# On the internal physical conditions in dust probes:

Transport, heating and evaporation of fragmented dust particles

—

Tarjei Antonsen
Master's thesis in Space Physics FYS-3931 – December 2013
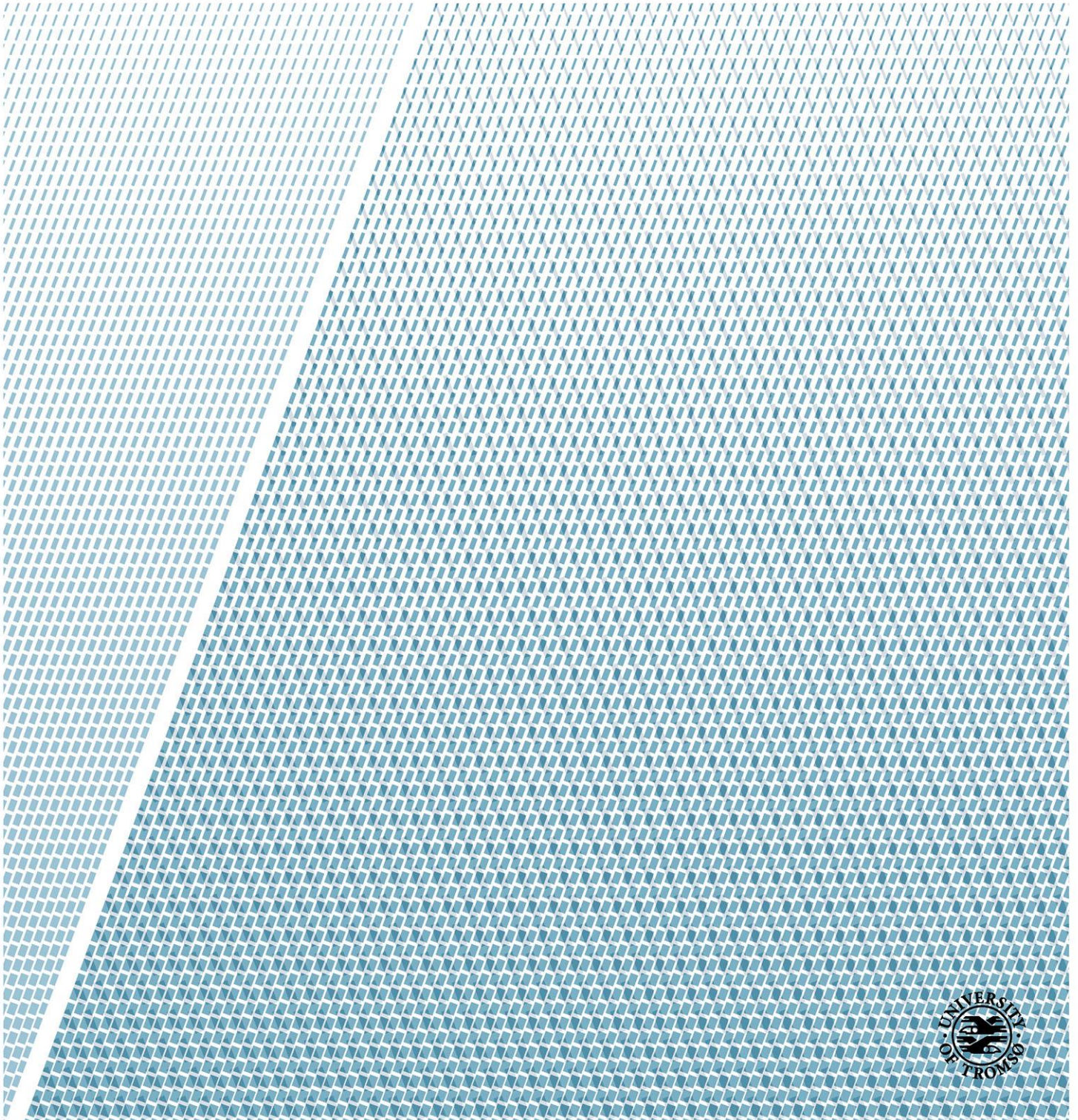
On the internal physical conditions in dust probes: Transport, heating and evaporation of fragmented dust particles.

Tarjei Antonsen

University of Tromsø
tarjei.antonsen@gmail.com
December 2013

2

Abstract

We study the conditions within, and dynamics of fragmented mesospheric dust particles inside, the Faraday-cup type dust probe MUDD using numerical simulations with a dedicated model. The transport of singly charged fragments from impacting NLC particles on the main grid in MUDD, have been calculated on the basis of supplementary models of the neutral gas conditions and electric field structure within the probe. The theoretical model includes the effects of drag from neutral molecules, electric forces, as well as heating of – and evaporation from – the fragments. The model equations have been improved to be valid for nanoscale particles with a broad range of intrinsic properties, in the molecular flow regime. We find that the size range for unambiguous detection of pure MSP fragments of mass density $\rho_s = 3000$ kgm^{-3}, is limited to fragments of radii between 1.5 nm and 2.1 nm with a 0.3 nm resolution; i.e. for the two existing detection modes of retarding potentials 10 V and 20 V. In the zero potential reference mode, fragments with radii smaller than 0.8 nm are stopped completely by neutrals. Fragments of pure ice content are found to evaporate rapidly, and will not contribute significantly to the measured currents at the bottom plate. Ice particles which contribute to the currents have to be larger than 3 nm, which renders the common assumption that ice particles smaller than 3 nm in radius must stick to probe surfaces [Tomsic, 2001; Havnes and Næsheim, 2007] redundant. From the study of alternative potential modes in MUDD, it is found that is is possible to improve the detectable size distribution of MUDD significantly by using lower retarding or accelerating potentials than the modes which already exist. Results from the E-field modeling suggest that the production of secondary charges have been somewhat underestimated due to very strong field anomalies near the edges of the probe. We also find plausibly large uncertainty factors from the investigations of initial fragment velocity, dynamic shape and heating of fragments during collisions with G2.

ii

Acknowledgments

Above all, I wish to express my sincerest gratitude to my supervisor Prof. Ove Havnes, for the continuous help he has given me throughout my work with this thesis. He has selflessly shared some of his vast knowledge with me through many interesting and inspiring discussions, and involved me in his research, which has motivated me to continue further into the magnificent world of dust physics.

It is also appropriate to thank Dr. Alexander Biebricher at NAROM, Andøya, with whom I had a fruitful discussion about the implementation of my theoretical model. Further thanks must be directed to Prof. Åshild Fredriksen who have helped me very much through the last one and a half years, especially with my involvement in the MAXIDUSTY-I project, where she has been a superb supervisor. In this regard, I must also thank project engineers Sveinung Olsen and Yngve Eilertsen for their help with technical aspects of my work.

On a personal note, I would like to thank all the master's students in "Norut-brakka" at the auroral observatory. Thank you for all the great conversations and bad cups of coffee.

Finally, a huge thanks to my beautiful girlfriend, Kaja, my friends, family and bandmates, for all the support you have given me through these last busy months, and for believing in me.

Tarjei Antonsen,
December 2013

Contents

Chapter 1

Introduction

The rocket-borne dust probe has historically been – and still remains – a most vital observation tool in the investigation of the mesosphere. Situated between around 55 and 100 km, the mesosphere can only be investigated in situ by rockets, as it is unapproachable for balloons and satellites. The spatial resolution of dust probes can be as low as ~ 0.2 m, and is therefore moreover superior to remote methods in investigating small-scale phenomena.

Mesospheric aerosols, from hereon referred to as *dust*, have been observed in the form of visible clouds in the polar regions since the late 1800s [Brekke, 2013]. Through the last few decades, unambiguous evidence has been obtained for these so called noctilucent clouds (NLC) and their related sub-visual spectrum phenomena polar mesospheric summer echoes (PMSE), which consist of charged nano-scale ice particles. It is referred to Rapp and Lübken [2004] and Rapp and Thomas [2006] for detailed reviews on the topic of icy dust particles.

Knowledge about ice dust and other mesospheric dust types have become important through the course of the last decades, since it was first theorized by Rosinski and Snow [1961] and later substantially quantified by Hunten et al. [1980], that residual particles of meteoric ablation could recondense into nanoscale dust; so called meteoric smoke particles (MSP). These dust particles, which are thought to act as nucleation sites for NLC and PMSE particles, have been suggested to be involved in a number of processes in the upper and middle atmosphere. They are suggested to affect the water and radiation budget of the Earth, and possibly indicate and even induce changes in the climate [Andreae and Rosenfeld, 2008; Thomas and Olivero, 2001]. Many of the processes which connects the mesosphere to the D-layer plasma above, and the stratosphere below, are thought to be controlled by mesospheric dust. The formation of clouds and subsequent destruction of ozone in the polar stratosphere [Voigt et al., 2005], and removal of metal layers in the middle atmosphere [She et al., 2006] is attributed to mesospheric

dust.

The MSP particles typically have radii smaller than 3 nm, and are thus extremely hard to observe directly. In fact, no unambiguous direct observation of such particles have yet been achieved (see e.g. Rapp et al. [2007] for a review). The aim of this work is to analyze the dynamics inside – and subsequently assess and improve the detecting capabilities of – dust probes of a Faraday cup-type design, represented here by the MUltiple Dust Detector probe (MUDD) developed at the University of Tromsø. This design is an extension of the design of Havnes et al. [1996] who was the first to decisively detect charged dust particles in the mesosphere. The MUDD probe aims to analyze the sizes of fragments from NLC particles which are shattered by mechanical impact inside the probe, and a large part of these fragments are thought to be pure MSPs. However, the environment of rocket probes is highly complex and includes supersonic flows, different flow regimes and lacks stationarity of many important background parameters. The correct interpretation of probe data and development of new methods is therefore dependent on elaborate theoretical considerations, which this thesis intends to provide, and we approach the stated problem by analyzing the dynamics of a variety of fragment types. It is found that the current MUDD probe can detect MSPs of radii between 1.5 nm and 2.1 nm with a resolution of 0.3 nm, however, to extend this spectrum down to 0.8 nm or even lower, with a higher resolution, is found to be advantageous and may be achieved without significant changes to the design.

An ultimate objective for this study, is that the results obtained and theoretical considerations given, can be utilized in the ongoing research in the field of mesospheric dust physics. Immediate contributions are aimed towards:

- Improving the analysis of fragment energies of an already launched MUDD probe (PHOCUS campaign, 2011; see e.g. [Havnes et al., 2014]) to find a best possible fragment size distribution.

- Optimizing the choice of potential modes in a triplet of MUDD probes to be launched on the payload MAXIDUSTY-1 in 2014.

- Investigating if the inner mechanical structure of the MUDD probes can be modified to improve their performance.

This work is structured in the following way: In chapter 2, a detailed introduction of mesospheric dust is given. It includes a discussion of nucleation mechanisms, heating mechanisms as well as a more detailed review of the possible influences of dust on middle atmosphere chemistry. An introduction of MSPs constructs a framework for our considerations of the fragment dynamics. Chapter 3 focuses on the observation of dust by rockets, and introduces the domain of our theoretical calculations; the MUDD

probe. The problem setup of fragmentation in MUDD is presented, and the connection between the obtained solutions and real MUDD data is given through the explanation of the detection procedure. We also give justifications of the choice important intrinsic parameters such as fragment charge and chemical composition in our model. The theoretical model, consisting of the three combined models for electric fields, neutral gas dynamics and dust fragment dynamics, is subsequently presented in chapter 4. We focus on the model equations for the dust dynamics which have been unified and implemented explicitly for this thesis. Improvements and adjustment factors for the model equations are also discussed.

Chapter 2

Dust in the middle atmosphere

Understanding the dynamics of middle atmosphere dust is very much constrained by the knowledge of its intrinsic properties. This chapter will accordingly introduce the typical dust particle encountered in-situ in the mesosphere, the atmospheric layer between around 55 and 100 km. Section 2.1 introduces the meteoric smoke particle (MSP) by discussing the current evidence on the topic, and the following section discusses the mesospheric dusty ice condensates, their coupling to MSPs, nucleation and heating mechanisms; topics which are central in the study of dust fragmentation. The chapter is concluded in section 2.3 which motivates the study of the content of middle atmospheric dust by discussing the mechanisms in which dust from the mesosphere may influence the neighboring atmospheric regions. On the background of a number of studies, we present a review concluding that dust particles may be central in the connection mechanisms with the stratosphere and the dusty D-region plasma.

2.1 Meteoric smoke particles

The global mass influx of meteoric material due to ablation of meteoroids is estimated to be of the order of 10 to 200 metric tons per day (see e.g. Love and Brownlee [1993]; Gabrielli et al. [2004]). About 70 percent of the meteoric material reaching the Earth ablates at altitudes between 70 and 110 km, and the majority of their ablation products comes from the evaporation of micrometeoroids of radii ranging from about 5 μm to 250 μm. For larger bodies, it has been found that relatively small fractions of mass are deposited above and within the middle atmosphere (see e.g. Love and Brownlee and Hunten et al. [1980]). It was early proposed, by Rosinski and Snow [1961], that the oxidization of ablation vapor could create species such as Iron oxide (FeO) and silicon oxides (SiO/SiO$_2$) which were likely to subsequently

recondense into nanometer-scale solid particles; so called meteoric smoke particles (MSPs). This work was later quantified to a significant extent by Hunten et al. [1980] who introduced a microphysical model considering not only the initial recondensation, but also subsequent growth of the particles by coagulation, and particle transport by eddy-diffusion.

Their calculations predicted concentrations of up to several thousand MSPs cm^{-3} with radii up to a few nanometers. Figure 2.1 shows the steady-state solutions from Hunten et al. for different initial radii, and illustrates that the particles grow through gravitational sedimentation to lower altitudes; a consequence of the coagulation and eddy-mechanisms in the model.

Following these pioneering studies, MSPs have been suggested to be of importance in several different atmospheric phenomena, the most relevant of which will be discussed in sections 2.2 and 2.3.
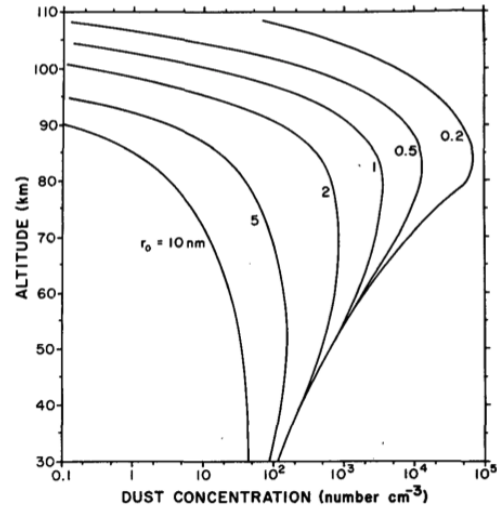
Figure 2.1: Predicted steady-state concentrations for dust particles of different initial radii. Adopted from Hunten et al. [1980]

2.2   Mesospheric dusty ice condensates

The existing studies of mesospheric dust have provided unambiguous evidence of ice particles in the polar summer mesopause region (see e.g. Lübken and Höffner [2004] and Rapp and Thomas [2006] for detailed reviews). Noctilucent clouds (NLC) and polar mesospheric summer echoes (PMSE), two phenomena strongly coupled with water ice dust-types, are temporarily high concentrations of icy particles near the high latitude mesopause region between altitudes of 85 km to 90 km [Thomas, 1991]. For rocket-borne dust probes, charged dusty ice particles originating from NLC and PMSE are the particle species likely to be encountered in the mesosphere. This study primarily addresses how dust probes, with special focus on the Faraday cup-type MUDD probe, can measure the size distribution of charged dust particles resulting from the fragmentation of NLC particles within the probes.

To serve the understanding of how the dust acts in the vicinity of a dust probe, the next sections include theory on different mechanisms that define the properties of dust particles, also called dust grains. These characteristica are pivotal for how destruction of dust grains in rocket probes complicates

the interpretation of observational results for certain scenarios, and for how dust grains fragment, which is further addressed in the next chapter.

2.2.1 Nucleation of dust grains

Predicting the behavior of dust in a turbulent dynamic environment will benefit from a priori information about the structure and size distribution of the grains. As the experimental evidence of mesospheric dust is limited, many dust characteristica can be approximated with nucleation and growth theories. As for the growth of ice particles, it can be considered as an automatic condensation mechanism. Thermodynamically, for a phase change to happen, e.g. the condensation from gas to an amorphous or solid form, the specific Gibbs free energy must be the same for the two phases. The critical vapor pressure between condensation and evaporation of a dust grain at a temperature T_d is then given by the Clausius-Clapeyron relation (on the form of Lichtenegger and Kömle [1991]):

$$P_{vap}(T_d) = P_{ref}\exp\left(\frac{m_D \cdot L_d}{k_B}\left[\frac{1}{T_{ref}} - \frac{1}{T_d}\right]\right) \tag{2.1}$$

where P_{ref} is the material specific pressure at some reference temperature T_{ref}, m_D is the mass of one dust-molecule, L_d is the latent heat of evaporation and k_B is the Boltzmann constant. The reference values for water ice are $P_{ref} = 10^5 Nm^{-2}$ at $T_{ref} = 373K$ with heat of vaporization $L^{Ice} = 2.78 \cdot 10^6 Jkg^{-1}$. Note that this formula is general and thus applicable to growth or evaporation of smoke particles also. The latent heat of smoke which will be utilized is $L^{smoke} = 6 \cdot 10^6 Jkg^{-1}$ [Hunten et al., 1980].

The vapor pressure term have been subject of studies for a relatively long time [Kelley, 1935; Lamy, 1974; Lichtenegger and Kömle, 1991], motivated by that uncertainties in the vapor pressure term will introduce errors in the thermodynamic calculations of dust particles. Podolak et al. [1988] introduced vapor pressure terms for smoke and ice which differs from the one of Lichtenegger and Kömle [1991] at low pressures and radii. Their improved expressions have moreover been employed in molecular dynamics simulations of dust in Horanyi et al. [1999]. This thesis will therefore represent vapor pressure by these modified terms:

$$P_{vap}(T_d) = \begin{cases} 3.89 \cdot 10^{10}\exp\left(-4845/T_d\right) & \text{for ice particles} \\ 1.51 \cdot 10^{12}\exp\left(-56655/T_d\right) & \text{for smoke particles} \end{cases} \tag{2.2}$$

For small radii, a correction factor should be included in equation (2.1) which accounts for evaporation from a spherical surface, which may be calculated as [Evans, 1994]:

$$P_{vap}(T_d, r_d) = P_{vap}^{(2.2)}(T_d) \cdot \exp\left(\frac{2\gamma m_D}{\rho_d k_B T_d r_d}\right) \tag{2.3}$$

where γ is the specific surface energy of the dust grain, m_D is the mass of *one* dust molecule and ρ_d is the grain density. According to a recent study by Gundlach et al. [2011], the surface energy of a micrometer-sized ice particle is $\gamma_{ice} = 0.190 Jm^{-2}$. For the smoke particles, we need to know about the intrinsic chemical composition of MSPs. As will be justified later, it shall be assumed that the particle origin is chondritic meteoroids, and it is therefore rational to employ a mean surface energy measurement of typical chondritic condensates to represent MSPs. It is found for SiO_2 in the literature that $\bar{\gamma}_{Smoke} \approx 0.200 Jm^{-2}$ [Kendall et al., 1987; Heim et al., 1999], i.e. rather similar to that one of ice.

For condensation to take place, however, there must exist a nucleation site for the condensing vapor; a seed. The mechanisms through which this seed may nucleate are many and highly complex, and we therefore discuss the two broad headings that describes the main mechanisms of initial nucleation of dust grains of ice and MSP.

Heterogeneous nucleation

As the name proposes, heterogeneous nucleation describes the situation in which the condensing species is chemically different from the condensation site. For NLC particles, MSPs were early considered as the most plausible condensation site for mesospheric water vapor. It has been confirmed in the laboratory by Saunders and Plane [2006] that the suggested recondensation of meteoric material can indeed happen when considering chondritic meteoroids, i.e. meteoroids containing approximately equal amounts of Iron, Magnesium and Silicon. Furthermore it has been argued that molecules with very large dipole moments, e.g. $MgSiO_3$ and $FeSiO_3$ from chondritic meteoroid ablation, are likely to bind to water molecules under mesospheric conditions [Plane, 2011]. However, whether the recondensed MSPs consists of separate species of metal silicates and pure silica or non-stoichiometric compounds of Mg-, Fe- and Si-oxides [Hervig et al., 2012] is still in lack of a definite answer. A justification of the choice of MSP content in the theoretical model is given in chapter 3.5.2.

Homogeneous nucleation

The polar summer mesopause is the coldest region in the earth's atmosphere with temperatures reaching as low as 110 K [Lübken et al., 2009] with fluctuations of ± 10 K due to gravitational waves breaking in the mesosphere [Rapp et al., 2002]. An example of a measurement of temperature in the summer mesosphere in the presence of ice particles with radii of a few nanometers is shown in fig. 2.2. Due to these low temperatures, water vapor *alone* can nucleate almost barrier free, as motivated by Ostwald's rule (cf. Ostwald [1897]; Murray and Jensen [2010]) which states that 'an unstable

system does not necessarily transform directly in to the most stable state, but to the state which is accompanied by the smallest loss of free energy'.

For water vapor this means that the water molecules does not need to "jump" from the gaseous state to the stable hexagonal ice (I_h), or even to a meta-stable cubic ice form (I_c), but may rather bind in a so called amorphous solid state, i.e. one without any crystalline structure.

Figure 2.2: Temperature profile in the presence of nanoscale dusty ice (red). The lines illustrates the frost points. Adopted from Lübken et al. [2009]

The homogeneous nucleation mechanism was until recently thought of as unlikely in the mesosphere, but two independent studies, namely Zasetsky et al. [2009] and Murray and Jensen [2010], have cast new light on the subject. They showed theoretically that not only is it possible for water vapor to condense to nanometer sized amorphous solid water grains, but in periods with a rapid decrease in temperature ($\sim 5K/h$) as induced by gravity waves, the homogeneous mechanism *may compete* with the heterogeneous one.

Due to the lack of indisputable evidence for the true content of NLC and PMSE particles, this study will not focus on one definite particle type but treat ice and smoke particles of chondritic materials independently as the mesospheric ice particles are likely to be hybrids of smoke and ice (as argued in [Plane, 2011]). However, as just presented, it is not certain whether the initial condensation core of the particles is amorphous solid water, or if the particles have a smoke core; which can be important for how the particles evaporate in dust probes because of the implications it may have for the structure of the larger NLC/PMSE particles. The theoretical calculations presented in this work are based on the traditional view that the ice is hexagonal in structure, and that the large dust particles are very likely to contain some MSPs.

2.2.2 Heating of dust grains

Dust probes which utilize a closed bucket design like the Faraday cup, also known as 'impact probes' (e.g. MUDD and DUSTY), has as a consequence a rise in number density and also a rise in background gas temperature, during flight. Because of the large temperature difference between a cold dust grain and the gas inside the dust probe, this study must address the possible evaporation of surface molecules from the grain. The heating effect is only accounted for after the dust grain has passed through the front shock
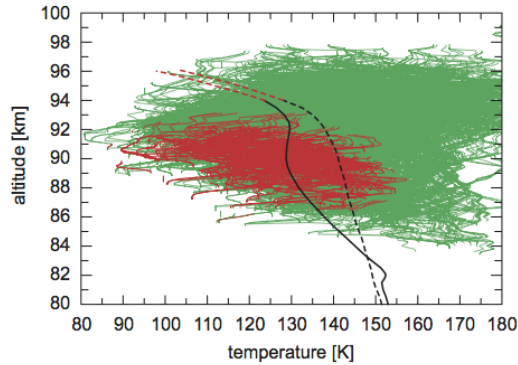
of the probe, which is to say that we assume the heating through the shock to be modest. However, as is discussed in chapter 6, the heating effect may be important in several stages of the detection procedure and more thorough investigation might be necessary.

When a dust grain is immersed in a gas of neutrals (with or without ions), atoms (or molecules) with velocities characteristic of the thermal energy of the gas will strike the surface of a dust grain. The initial kinetic energy of one atom is then:

$$\frac{1}{2}m_g v_g^2 = \frac{3}{2}k_B T_g \tag{2.4}$$

where m_g and v_g are the mass and velocity of an incoming neutral atom and T_g is the macroscopic neutral gas temperature.

On a microscopic level, a collision is not a hard sphere interaction due to the fact that a grain is very unlikely to have a perfect spherical and crystalline structure. In fact, a grain surface may contain a number of irregularities that constitute potential wells in which a neutral atom or ion may be trapped in [Evans, 1994]. When an incoming atom is trapped in such a potential well with depth U, it will vibrate at a frequency ν, and the probability for the atom to leave a potential well is proportional to a Boltzmann factor, $\exp(U/kT_d)$. The time an atom is likely to stay at the surface of a dust grain and vibrate is then:
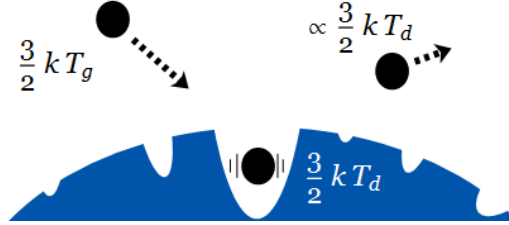
Figure 2.3: Energy exchange during an interaction between atom and dust grain surface potential.

$$\Delta t_{surf} = \nu \cdot \exp\left(\frac{U}{k_B T_d}\right) \tag{2.5}$$

The atom will subsequently leave with a speed characteristic of the dust grain temperature and not the gas [Evans, 1994], as illustrated in figure 2.3. Thus the atom has provided net amount of energy ΔE to the dust grain

$$\Delta E = \frac{1}{2}m_g\left(v_g'^2 - v_g^2\right) = \frac{3}{2}k_B\left(T_g - T_d\right) \tag{2.6}$$

where v_g' is the atom speed *after* the interaction. Note that this is only valid in a perfectly efficient energy transfer, which is unrealistic. In addition; a rigorous derivation of the energy balance should also take into account the thermal radiation from the grain and the Maxwellian nature of the neutral gas atoms.

2.3 Influence on middle atmosphere chemistry

Dust and aerosols are abundant through the entire atmosphere. In the middle and upper atmosphere, i.e. the stratosphere and mesosphere in the altitude region between around 20 km to 100 km, internal layers can interact with each other in processes which often involve dust particles. The fundamental motivation of many studies of the mesosphere is thus to better understand the complex chemistry within – and coupling between – the neighboring atmospheric regions.

The dust particles which the MUDD probe aims to investigate are mesospheric dust particles consisting presumably of ice with embedded MSPs, with the MSPs presented in the previous sections. These particles can constitute visible clouds in the polar summer mesosphere, NLC, which have been found to fit with a monodispersive distribution of radii around 50 nm, or a gaussian distribution with a mean radius of 34 nm [von Cossart et al., 1999; Megner et al., 2009] assuming spherical particles. NLC particles together with smaller ice particles of radii down to ~ 10 nm, constitute the similar phenomenon PMSE which are radar echoes that often partly overlap the NLC in space and time. A typical NLC with wave structures due to gravity waves propagating upwards can be seen in figure 2.4.

Figure 2.4: A Noctilucent cloud observed during twilight from Estonia. Photo: Martin Koitmäe via Wikimedia commons.

Both NLC particles and PMSE particles provide surface area where chemical reactions may take place, by lowering the energy barrier for the reactions [Evans, 1994]. This is also true for free MSPs, where these chemical reactions are likely to happen in potential wells on an MSP surface, as opposed to *without* a third body in the ambient space. The same principle

can be applied to dust growth; a combination is more likely to happen if a third body (e.g. an MSP) can carry of the energy resulting from a combination. She et al. [2006] observed a strong anti-correlation between NLC and mesospheric Sodium (Na-) layers, and found PMSE measurements to be consistent with a weaker anti-correlation. Their results were in good agreement with the results of Lübken and Höffner [2004] regarding the removal of Potassium (K) by icy dust particles, and together they provide strong evidence for the effect of dust as effective sinks on mesospheric (alkali) metal layers.

Another important mechanism which may take place on dust surfaces is the destruction of ozone. The mesospheric temperature has sunk $\mathcal{O}(1)$ K since 1979 with cooling rates up to ~ 0.4 Kyr^{-1} [Keckhut et al., 1995; Keckhut, 2001], and it is probably due to this lowering that the occurrence of NLC has doubled over the last decades [Gadsden, 1997]. Thus it is speculated that the destruction rate of ozone may be rising as a consequence of the higher occurrence of mesospheric dust.

In section 2.1 it was pointed out, as illustrated in figure 2.1, that MSPs nucleate at mesospheric altitudes and can coagulate as they move downwards. The figure shows theoretical concentrations of MSPs of radii up to 10 nm from some 10 to some 100 cm^{-3}. During the winter, when dust particles must be smaller in size than NLC and PMSE particles [Havnes and Kassa, 2009b], dust acquire downwards momentum within the polar vortices through the stratosphere [Hervig et al., 2009; Bardeen et al., 2008]. The MSPs may subsequently remove nitric acid vapor from the stratospheric aerosol layer, which may indirectly increase the rate of depletion of ozone in the stratosphere [Prather and Rodriguez, 1988; Voigt et al., 2005].

For free MSPs, models have predicted concentrations of around 1000 cm^{-3} at the summer mesopause and around 4000 cm^{-3} at the winter mesopause [Megner et al., 2008; Bardeen et al., 2008]. However, as few long-term observations of the mesospheric dust exist, there is great uncertainty in the real concentration. A mean number density of NLC particles of 83 cm^{-3} was observed at the polar northern mesopause by von Cossart et al. [1999]. Interestingly, it has been argued that the predicted summer concentrations cannot account for the observed high concentrations of icy dust in NLCs and PMSEs if nucleation is completely heterogeneous with MSPs as the condensation nuclei [Hervig et al., 2009]. This supports the theoretical findings of Murray and Jensen [2010] and Zasetsky et al. [2009] which conclude that homogeneous nucleation mechanisms may compete with the heterogeneous ones.

Chapter 3

Observation of dust particles

A natural point of continuation in the theoretical background of mesospheric dust is to discuss how the dust may be observed. The focus is directed towards sounding rocket dust probes, represented in this paper by the Faraday cup-type MUDD probe. A study of dust dynamics in a probe environment may often be dependent on a priori theoretical information about the observed quantities to correctly interpret observational data. To give extensive insight into such information, is very much the objective of this thesis. This chapter includes a motivation, a status-of-knowledge, of mesospheric dust observation by rockets and how theory and experiments completes – and corrects – each other to yield important background knowledge for a thesis like the present. In section 3.2 and 3.3, the focus is directed towards MUDD, and the spatial configuration and basic formulation of the problem of fragmentation between the main (bottom) grid G2 and detector plate BP is given. A presentation of the detection procedure is given in section 3.4, in which an explanation of how the theoretical model can be connected to the real MUDD is given. The last section addresses the fragment types which are likely to form in a collision with G2, and thereby defines the main particle species which are investigated in this paper.

3.1   In-situ observation by rocket probes

Evidence exists for small-scale interactions between dust and the background atmosphere, and it is speculated that mesospheric and stratospheric dust may also affect the climate on larger scales [Andreae and Rosenfeld, 2008]. Therefore, the intrinsic chemical properties of dust particles have received considerable attention in the last few decades, particularly in the troposphere and stratosphere where where long-time in-situ observations can be carried out by airplane and balloons; see e.g. Cziczo et al. [2001]; Bigg [2012] for recent reviews. The situation for the mesosphere is more complicated because of its inaccessibility to balloons. For both stationary ground based

radars and space-borne radars, the dust particles of interest, mainly NLC and PMSE particles, are generally situated too low to be observed directly. However, powerful instruments and techniques have been developed which allows for observation of cloud phenomena on length scales down to 100 m. Due to their effect on electron density spatial distribution, dust particles can be indirectly observed by radars as predicted by the model of Havnes et al. [1984]. The reader is referred to e.g. [Havnes, 2004; Havnes and Kassa, 2009a; Friedrich and Rapp, 2009] for excellent papers on the topic of PMSE/PMWE. Methods for dust observation by incoherent scatter radars (ISR) which take advantage of the narrowing of ISR spectra by MSPs have also been proposed [Rapp et al., 2007]. The observation of mesospheric icy dust by satellites have also gotten its renaissance through solar occultation [Hervig et al., 2009, 2012].

For in-situ observation at a very much smaller length scale than what remote methods provide, sounding rockets are necessary. Instrumented rockets can have a spatial resolution on the order of 10 cm ($\sim$ 4000 samples/sec at 1000 ms^{-1} yields a 25 cm resolution) which allows them to investigate the mesosphere with remarkable precision. One of the early discoveries by rockets was the extremely low temperature minima at $\sim$ 85 km [Theon et al., 1967] which has been found to be crucial for ice formation, and characteristica like temperature profile and turbulence distribution have later been measured [Inhester et al., 1994; Lübken et al., 2002]. After Pedersen et al. [1969] suggested that dust particles could affect the charge balance in the mesosphere rather strongly, much effort have been put into observing the dust particles directly with instruments like faraday cups, mass spectrometers and Gerdien-condensers. To collect and retrieve any kind of mesospheric dust back to the ground for a first hand study, remains however yet to be achieved [Rapp et al., 2007].

DUSTY, which is a Faraday cup probe developed at UiT and a precursor of MUDD, was the first experiment to unambiguously observe charged dust in the mesosphere [Havnes et al., 1996]. An important note about the cup designs of DUSTY and MUDD is that particles with radii < 2 nm, i.e. typical radii of MSPs, are likely to be swept away by the shock on the front of the probe [Horanyi et al., 1999; Hedin et al., 2007], although newer designs reduces this problem (see e.g. Robertson et al. [2009]). MUDD, however takes advantage of the tendency of MSPs to stick effectively to ice and vice-versa, and lets the high mobility NLC particles carry the MSP inside the probe, releasing the 'free passenger' MSPs as they fragment. Measurements by faraday cup probes have moreover been shown to be affected by secondary charging due to fragments rubbing of charges from impact surfaces [Havnes et al., 1996; Kassa et al., 2012]. This issue is touched upon in the later discussions.

3.2 The MUDD probe

Figure 3.1 shows the principle of the MUDD dust detector. MUDD is essentially a Faraday cup with three grids; G0, G1 and G2. The top grid, G0, is intended as earth at the payload potential, to shield the other instruments on the payload from the electric fields from the lower grids. However, G0 is unlikely to have zero potential as rocket payloads are readily negatively charged with a couple of volts in the mesosphere; see e.g. Bekkeng et al. [2013]. The second grid from the top, G1, is set at a constant voltage at + 6.2 V, which will stop the positively charged ambient ions from entering. Grid 2 (G2) consists of concentric metal rings with a height of 9.5 mm and an inclination of just above 20° to the perpendicular plane. This inclination is set such that the rings overlap slightly and there is no direct flux through G2; every particle must collide with a ring. G2 has a constant voltage of + 10 V. The bottom plate (BP) has a varying electric potential which cycles through the values +10 V, 0 V, -10 V and back to 0 V, and the cycle is subsequently repeated. The currents to G1, G2 and BP are sampled at 1920 Hz where each voltage of the BP-cycle are sampled 39 times, corresponding to about 14 m of flight. Between these sampling groups, there is a small gap, corresponding to about 5 samples ($\approx$ 2 m in height). These specifications yield a resolution of $\mathcal{O}(10)$ cm which can be considered far superior to the resolutions of ground based radars, lidars and satellite borne radars.
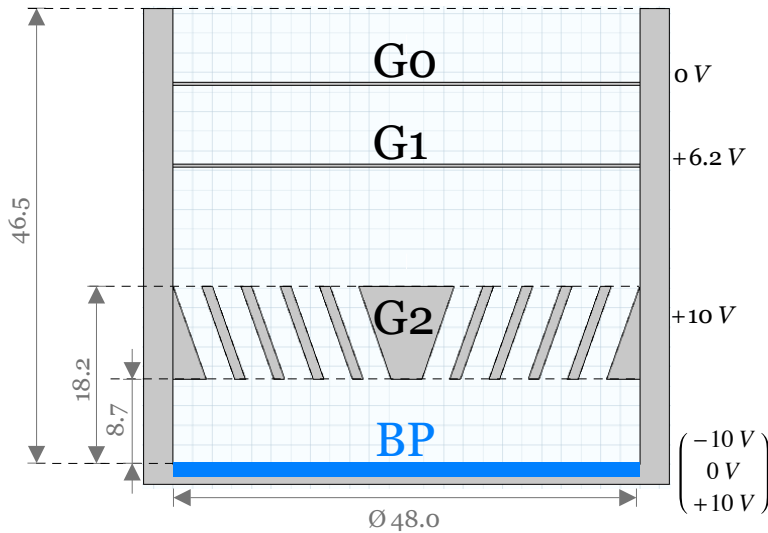

Figure 3.1: Vertical cross section of the MUDD probe. The length measures are given in mm.

3.3   Fragmentation of dust grains in MUDD

The "large" incoming icy dust particles with $r_d > 10$ nm, will hit G2 at an incidence angle of 70° (to the G2 normal), with a velocity close to the rocket velocity. During the first launch of the MUDD probe in the PHOCUS campaign in 2011, this was close to 700 ms^{-1}, and the MUDD probes planned to be launched on MAXIDUSTY I, are assumed to have very similar technical specifications.

Figure 3.2 sums up the key parameters and geometry which will be used in the simulations of dust fragment movement in MUDD. The incoming dust grains will fragment into smaller particles, from hereon primarily referred to as *fragments*, which will leave almost parallel to the impact surface G2; $\theta = 6°$ will be used in this study [Tomsic, 2001],. Tomsic [2001] found experimentally a strong size dependence in the velocity distribution of the fragments of pure ice grains of radii up to 7 nm with an impact angle of 70° to the G2 surface normal. On a gold-coated impact surface, the larger fragments with energies over 100 eV may conserve between 60 and 70 % of their initial velocity. For other materials, e.g. smooth graphite, more of the ini-

Figure 3.2: Configuration of the problem of dust fragment transport between G2 and BP.

tial energy is retained [Tomsic, 2001]. Now, since many of the fragments in MUDD have lower energies ($< 20eV$, Havnes, priv. comm.) we may draw from the results of Tomsic that the fragments keep at least 40% of their initial energy if we extrapolate – and even more in MUDD since the impact surface is stainless steel. Thus in this study, initial fragment velocities of $v_0 \sim 450 \pm 100ms^{-1}$ are used to account for the uncertainty in fragment kinetic energy.

The geometry and environment for fragmentation from an isolated impact plane of G2 must also take into account the neutral gas parameters and local electric fields. The gas parameters are assumed to be global for the entire system sketched in fig. 3.2 and are computed in the neutral gas simulations. For the electric fields, an assumption has been made; enhanced local electric fields because of sharp probe corners and edges are disregarded. It may actually become a point of interest to investigate the theoretical effects of enhanced fields at the probe edges, as they can become large enough to introduce numerical instabilities, which will be discussed below. There-

fore, a homogeneous E-field between G2 and BP is used while the fields are assumed to be zero inside G2. The E-field solution given in this thesis is therefore not applied directly onto the fragmentation problem, but it has applications in further research on and with MUDD. The field values are dependent on the potential difference between G2 and BP. Throughout the paper, these parameters will be used interchangeably; a certain bottom plate potential will give rise to a retarding electric field. The energies of incoming particles are estimated by comparing the currents at BP at the different retarding potentials against a reference potential. Since G2 is set on a constant voltage of 10V, when the potentials are equal, the retarding potential is zero; when $V_{BP} = 0$, the retarding potential of negative particles is 10 V, and; when $V_{BP} = -10$ the retarding potential is 20 V. We will in addition address the possible effects off smaller retarding potentials of respectively 1, 2 and 5V, on the detection sensitivity and measurement resolution of smoke particles.

3.4 The detection procedure

The solutions obtained with the theoretical model, which is introduced in chapter 4, may be presented in a number of ways due to the versatility and applicability of the model simulations. To address the relationship between the model simulations and the real MUDD probe is appropriate at this point. In the following, we give a justification of how we interpret the obtained solutions and compare them to real data.

The MUDD probe measures currents at its different grids as the potential on the bottom plate, BP, is varied. An approximation of the fragment size distribution may be deduced from the change in currents measured at the bottom grid, G2, and BP. The grids G0 and G1 detects the ambient electron currents, and primary and secondary currents from impacting dust, but are not significantly affected by the alternating potential over BP. Figure 3.3 shows a hypothetical measurement of the current at BP while the rocket is traveling through a layer of increasing charge density (e.g. an NLC). The highest current is measured when there is no potential between G2 and BP ($V_{BP} = 10V$); we call this potential mode the *reference mode*. As the BP potential is switched to $V_{BP} = 0V$, the fragments experience a 10 V retarding potential and a portion of the fragments are stopped, reducing the current; we name this potential mode the *first detection mode*. The potential is subsequently cycled to -10 V, yielding a 20 V retarding potential for negatively charged fragments; the *second detection mode*. After this, the potential is alternated back to the first detection mode, before the cycle is repeated. In summary: BP cycles through the potentials (+10 V, 0 V, -10 V, 0 V,...). By comparing the currents from the detection modes with the reference mode, it is possible to deduce the proportion of fragments which

are stopped and thus derive their energies (or sizes).
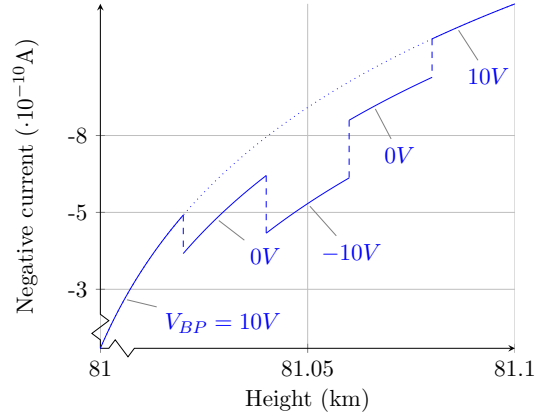
Figure 3.3: Sketch of how the negative BP current may rise through an NLC layer for the different potential modes of MUDD. The labels are arbitrary.

In this paper we will connect this picture of the MUDD currents to the obtained solutions in a couple ways. One method is to probe the energy a fragment has on impact. The fragment energy is a very convenient way to represent results, and may be transferred to MUDD because of its proportionality to the measured current. However, the fragments have a discrete and finite number of charges ($-1e$ here), and the fragment energy ceases to exist as a useful measurement when it represents situations where none of the fragments are stopped between G2 and BP; it will then give ambiguous information. Nevertheless, it is possible to probe the most energetic impacts as a representative for the amount of current a certain fragment species will produce.

Another approach which will help to overcome ambiguities, is to count the percentage of hits at BP. It will be directly proportional to the measured current, assuming that every charged fragment will transfer its charge to BP. This method yields a powerful tool for analyzing data due to its direct connection with the MUDD measurements. Together with the first method, it can also give information which may be utilized in further development of MUDD.

3.5   The MUDD particle

We have up to this point established why the NLC particles, i.e. the "large" mesospheric dust particles of radii up to 50 nm at a height of between 80-90 km containing MSPs, are interesting for the middle atmosphere chemistry. The MUDD probe is as explained designed to measure the size distribution of

the fragments which are created in the collisions between NLC particles and the grid G2. To interpret the MUDD data correctly, it is necessary to know how different fragment types with different radii behave between G2 and BP. This introduces an intricate problem with limiting factors introduced in both the current knowledge about the content and structure of MSP and NLC particles and their molecular dynamic behavior.


>20 nm   <2-3 nm
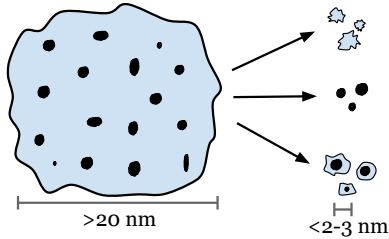
Figure 3.4: Three main types of fragments possibly found in dust probes. From top to bottom: ice, MSP and MSP with an ice layer.

An icy dust particle may fragment in different ways, and the degree of fragmentation is determined by intrinsic factors such as grain size, structure and composition as well as experimental factors such as collision velocity, impact angle and impact surface temperature [Tomsic, 2001; Tomsic et al., 2001]. The material strength and density of the grain is also important. The results of Tomsic [2001] are valid for pure ice particles, but we assume that NLC particles are similar in structure, and that the results are applicable to our situation. NLC particles may contain up to some thousand MSPs (up to 3-5% in volume) [Hervig et al., 2012; Havnes et al., 2014], and possible fragments might consist of pure ice, pure MSP or MSPs with an ice coating, as summed up in fig. 3.4. However, results from Tomsic [2001] show that ice particles of radii smaller than ~ 3 nm tend to stick to the impact surface when impact angles are similar to the inclination angle of G2 in MUDD. Thus it shall be assumed that none of the pure ice particles which have an initial radius < 3 nm contribute to the measured BP-current. Furthermore, Havnes and Næsheim [2007] and Kassa et al. [2012] find that the smallest fragments are unlikely to consist of pure ice, and the majority of the fragment size distribution is assumed to be occupied by pure MSPs. Regardless, the simulations presented in this work will include to some extent pure ice particles and MSPs with an ice coating to quantify a possible effect on the fragment energy history.

Tomsic [2001] describes an effect similar to the Leidenfrost effect for ice particles impacting at an angle. This effect describes the situation when the temperature difference between the ice particle and the impact surface is so large that the gas pressure from evaporating surface molecules can become large enough to form a 'cushion' of vapor underneath the particle. This cushion may ensure that the outermost molecules evaporate from the surface at the impacting area. If we assume that the MSPs in the impacting layer are also released, we may justify that a significant number of MSPs are among the fragments. Figure 3.5 shows the number of MSPs which are released during a collision if 1/4 of the total surface area of an NLC particle touches the G2 surface, and the outermost layer of MSPs are released. It

must be noted that this assumption is fairly pessimistic, and that more
MSPs should be released as NLC particles probably fragment more severely
at the energies and impact angles encountered in MUDD.
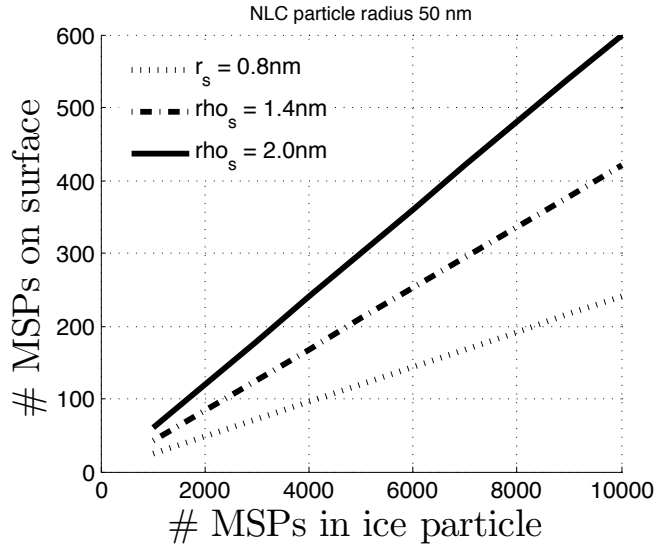
Figure 3.5: Number of released MSPs from an evaporation of the
outermost layer of impact of an NLC particle, shown for different MSP
radii. The MSP are assumed to be evenly dispersed.

3.5.1   Charge on fragments

An estimate of the charge a fragment obtains in a collision is necessary. Auer
and Sitte [1968] introduced an empirical relationship for charging of metal
and carbon particles impacting on tungsten surfaces, and found the charge
to be linearly dependent on the particle mass:

$$Q = K m_d v^\beta \tag{3.1}$$

where K is a constant and β ranges from 2 to 3.2. For micrometeoroid ana-
logues of similar sizes as the MSP fragments in MUDD, Adams and Smith
[1971] found that a particle may obtain a charge of $-1e$ with a probability
lower than 1%. This is however not particularly low. As NLC particles are
predominantly negatively charged, we adopt this result and assume each
fragment to have a charge number $Z_d = -1$ in the simulations.

Experimental results for pure ice particles give that the charging prob-
ability of a fragment is approximately 1 in 1000 [Tomsic, 2001]. However,
from rocket experiments it has been concluded that the charging probabil-
ity of NLC fragments may be between one to three orders of magnitude

higher Havnes et al. [1996]; Havnes and Næsheim [2007]; Kassa et al. [2012]. The NLC particles are abundant, with number densities, N_d, up to several thousand per cubic centimeter [Havnes et al., 1996] and (negative) charge densities, $N_d Z_d$, are found to be of the same order of magnitude [Robertson et al., 2009; Havnes et al., 1996].

3.5.2 Chemical composition of fragments

To solve for particle evaporation and heating, the fragment density and molecular weight must be known, among other parameters. For the water ice particles, a mass density of $\rho_i = 980$ kgm^{-3} will used. For the MSP particles, we must rely on a commensurate of studies to replace the still missing direct measurement of MSP content. A number of papers have been published on the subject, and possible candidates are given in table 3.1. It must be noted that most of the densities are given for the most stable solid state, although recondensed smoke particles may often have an amorphous structure (see e.g. Plane [2011]; Saunders and Plane [2006]; Zasetsky et al. [2009]), and therefore a lower density than the one listed. Authors mostly agree upon that the most likely candidates are direct condensation products from chondritic meteoroids, and in this study we will use a chondritic-type MSP, with density $\rho_s = 3000$ kgm^{-3} and a molecular weight of $m_D = 140$ a.m.u.

Table 3.1: Mass densities of MSP analogues. Chemical data is from the Euromin database and Webminerals. 'S' denotes a solid state while 'A' denotes an amorphous state.

Name	Chemical formula	Mass density $[\text{gcm}^{-3}]$	Author(s)
Wüstite	FeO	5.880	Hervig et al. [2012]
Magnesiowüstite	$\text{Mg}_x\text{Fe}_{1-x}O$, $x = 0.1 - 0.6$	< 4.0	"
Carbon	C	2.0 (S) 1.8 (A)	"
Göethite	FeO(OH)	4.18	Saunders and Plane [2006]
Silicon dioxide	SiO_2	2.65 (S) 2.20 (A)	"
Fayalite	Fe_2SiO_4	4.39	"
Olivines	$\text{Mg}_{2-x}\text{Fe}_{x-2}\text{SiO}_4$	3.0-3.4	Plane [2011]; Klekociuk et al. [2005]
Hematite	Fe_2O_3	> 5.0	Bohren and Olivero [1984]

Chapter 4

The theoretical model

In this chapter, a diffusion free closure of the transport equations for charged dust particles in an air filled probe will be introduced. The neutral air movement can be found by solving the Navier-Stokes equation with Chapman-Enskog expansion in the continuum and transitional flow regimes [Beskok and Karniadakis, 1994]. However, this approach is not valid in the free molecular flow regime for reasons discussed in section 4.2. To overcome this problem, we must therefore use the numerical procedure Direct Simulation Monte Carlo (DSMC) [Bird, 1994], which is introduced and justified in the same section. The equations used in the electric field modeling are introduced in section 4.1, for a rotationally symmetric system. The main model in this thesis is the one of the charged dust fragments. In sections 4.3 and 4.4, the self-consistent equations of the combined motion and evaporation of fragments are introduced. We have also included discussions where the choices of drag coefficient and dynamic shape factor are justified. In section 4.5 we summarize the input parameters used in our models.

4.1   Electric field inside the probe

Calculation of the electric fields inside the MUDD probe is a simple problem in electrodynamics if we make use of the axial symmetry of the design. The electric field vector can be written as the gradient of the scalar electric potential:

$$\vec{E} = -\nabla V. \tag{4.1}$$

Through the Gauss law on differential form, $\nabla \cdot \vec{E} = \rho/\epsilon_0$; where ρ is the space charge density and ϵ_0 is the vacuum permittivity, we can subsequently express the fundamental equations for $\vec{E}$ in terms of the electric potential, V, where the result is the Poisson's equation:

$$\nabla^2 V = \frac{\rho}{\epsilon_0}. \tag{4.2}$$

However, there are two important constraints of the MUDD probe (and other Faraday cups) during operation at mesospheric altitudes, which can be utilized in further manipulating the equation; (I) We assume that there are no space charges in the background gas, and (II) The spatial configuration of the probe allows for a rotationally symmetric solution. The problem of finding the electric fields then reduces to solving the Laplace equation in cylindrical coordinates, which can be stated as:

$$\nabla^2 V = \frac{1}{r}\frac{\partial}{\partial r}\left(r\frac{\partial V}{\partial r}\right) + \frac{\partial^2 V}{\partial z^2} = 0. \tag{4.3}$$

where $V(r,z)$ gives the azimuthally symmetric solution for every $\theta \in [0, 2\pi]$.

Due to the complex structure of MUDD, the partial differential equation (4.3) is handled numerically with finite element analysis with Dirichlet boundary conditions, i.e. for every boundary of every subdomain, V is assigned a value;

$$V(\vec{r}) = U(\vec{r}) \quad \forall \vec{r} \in \partial\Omega_i \tag{4.4}$$

where $\vec{r} = (r, z)$, $U(\vec{r})$ is an electric potential value in $\vec{r}$ and Ω_i is the i'th subdomain of MUDD. The two-dimensional axisymmetric geometry of MUDD is shown in fig. 4.1.
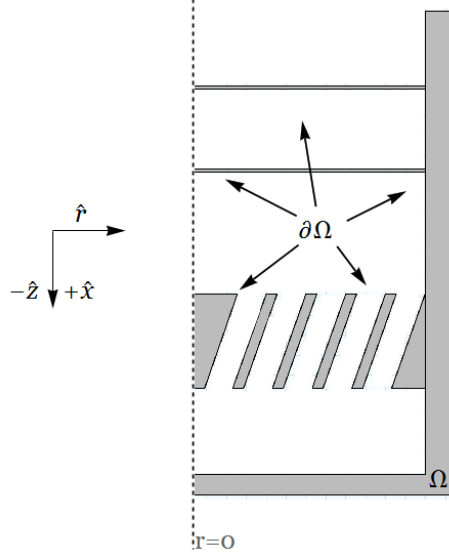

Figure 4.1: Geometry of the rotational symmetric formulation of the E-field problem in MUDD. All the boundaries are assigned potentials corresponding to the values shown in fig. 3.1 above (according to the Dirichlet conditions). In dust simulations, the geometry is tilted $-\pi/2$ so the flow direction becomes $+\hat{x}$.

4.2 Motion of neutrals

Describing and analyzing the neutral gas flow around and inside a rocket-borne dust probe is complicated in complex geometries. Before the core of the problem of neutral air motion is discussed, it may be advantageous to define a very fundamental equation for non-equilibrium systems; the Boltzmann equation. Appendix A therefore includes a general formulation of the equation.

A rocket in flight and its probes will experience different flow regimes which are characterized by the degree to which the neutral background gas is rarefied. This measure can be quantified by the Knudsen number which is defined as:

$$Kn = \frac{\lambda_{mfp}}{L} \tag{4.5}$$

where L is a characteristic dimension of a system, e.g. the dust grain radius or some dimension of the rocket probe. The parameter λ_{mfp} is the atmospheric mean free path which quantifies the mean undisturbed flight length of an atom or molecule of the gas. It can be expressed as:

$$\lambda_{mfp} = \frac{1}{\sqrt{2}\sigma_g n_g} \tag{4.6}$$

where $\sigma_g \approx 4.3 \cdot 10^{-19} m^2$ is the mean collisional cross-section of air molecules and n_g is the neutral (air) density. Traditionally it has been defined that a gas is in *continuum flow* when $Kn \leq 0.1$ and in a so called *free molecular flow* when $Kn >> 10$ [Hedin et al., 2007]. In a continuum flow gas, the gas movement can be calculated by the Navier-Stokes equations with a Chapman-Enskog correction for perturbations in the velocity distribution. A system with a high Knudsen number, however, will not have a well-defined collision derivative (see eq. (A.2)) for particles which are more likely to hit the system boundaries in stead of other particles, and Navier-Stokes cannot be used.

We are thus faced with some relevant problems in simulations of a rocket dust probe environment. As rocket bodies are highly aerodynamic structures and open payloads often have varying aerodynamic qualities, shock waves on the front of a payload may cause relatively large variations in the local Knudsen number. An illustration of the validity of fluid equations can be seen in fig. 4.2.

It should be pointed out that the conservation equations of fluid mechanics are valid for all flow regimes, but it has been argued that for Knudsen numbers in the transition regime ($Kn \gtrsim 0.1$), the continuum equations are hardly useable [Bird, 1994].

For dust probes utilized in the mesosphere, like MUDD, the background density (at 82 km and up) is low enough to lie well inside the transition
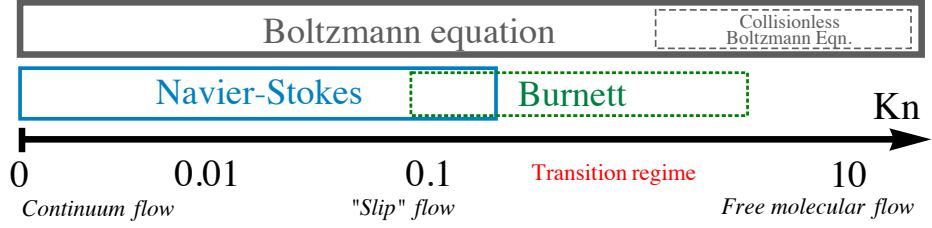
Figure 4.2: Valid equations in the different flow regimes characterized by the Knudsen number. Inspired by Beskok and Karniadakis [1994].

regime. The solution to this problem is a method called Direct Simulation Monte Carlo (DSMC) which uses probabilistic simulation to solve the Boltzmann equation. The code – DS2V – used in this study is written by G. Bird who also proposed the DSMC method. DS2V is used to calculate two-dimensional rotationally symmetric gas flows. It handles flows from the free molecular regime to the transition regime through simulating single particles and including particle-particle interactions and particle-boundary interactions. A quasi-steady state solution is obtained without the risk of numerical instabilities. Furthermore, the gas parameters are found and used in the dust motion simulations.

4.3   Motion of charged dust

The drag force experienced by a dust grain will depend on if the flow is subsonic or supersonic. For an ideal gas, the speed of sound is approximately (because of an approximation, $B = \gamma P_g$, of the bulk modulus in the Newton-Laplace equation) given by:

$$c_s = \left(\frac{\gamma n_g k_B T_g}{\rho_g}\right)^{\frac{1}{2}} = \left(\gamma \frac{k_B T_g}{m_g}\right)^{\frac{1}{2}} \tag{4.7}$$

where $\gamma = c_P/c_V$ is the ratio of specific heats at respectively constant pressure and constant volume, $n_g k_B T_g$ is the gas pressure and ρ_g is the gas density. Around a rocket probe, we assume the standard value of $\gamma \approx 1.4$ to be valid, as the pressure and density varies. During flight, the speed of sound in air between G2 and BP in MUDD is estimated to be $c_s = 376 ms^{-1}$ for parameters obtained in the neutral gas simulations. This is slightly higher than at sea level.

Furthermore, for the subsonic case, the drag-force is given by Stokes' law [Evans, 1994; Stokes, 1851]

$$\vec{F}_{drag} = 6\pi \eta r_d \vec{v}_{rel} \tag{4.8}$$

where it has been assumed that the dust particle is spherical with a radius r_d and velocity $\vec{v}_{rel} = \vec{v}_d - \vec{v}_g$ relative to the gas. The parameter η is the viscosity, which in terms of gas properties is:

$$\eta = \frac{1}{2} r_d n_g m_g \left(\frac{k_B T_g}{\pi m_g} \right)^{\frac{1}{2}} \tag{4.9}$$

where m_g is the molecular mass of the gas.

For supersonic movement, the drag force in a free molecular flow approximation is proportional to v_{rel}^2, and can be calculated as [Gombosi et al., 1986, eq. 63]

$$\vec{F}_{drag} = r_d^2 \pi \frac{C_D}{2} n_g m_g |\vec{v}_d - \vec{v}_g| (\vec{v}_d - \vec{v}_g) \tag{4.10}$$

where C_D is the drag-coefficient; usually set to unity, $\vec{v}_d$ is the dust velocity and $\vec{v}_g$ is the gas (mean) velocity. A justification of the choice of drag coefficient is given in section 4.3.2 below.

The equation of motion for a charged dust grain must include the electric force, and the full equation becomes

$$\frac{4\pi}{3} \rho_d r_d^3 \frac{d\vec{v}_d}{dt} = q_d \vec{E} + 3\pi r_d^2 n_g m_g \left(\frac{k_B T_g}{\pi m_g} \right)^{\frac{1}{2}} (\vec{v}_d - \vec{v}_g) \qquad \text{If } v_d < c_s \quad (4.11)$$

$$\frac{4\pi}{3} \rho_d r_d^3 \frac{d\vec{v}_d}{dt} = q_d \vec{E} + r_d^2 \pi \frac{C_D}{2} n_g m_g |\vec{v}_d - \vec{v}_g| (\vec{v}_d - \vec{v}_g). \qquad \text{If } v_d > c_s \quad (4.12)$$

4.3.1 Improvement of term for drag force

To simplify the implementation of the non-linear drag term above, it is advantageous to combine the equations into one which is valid for all velocities. We will therefore derive an improved neutral drag term based on the work of Baines et al. [1965] and Smirnov et al. [2007] which use a specular reflection of the neutral molecules from the dust surface. In the latter work, such a hybrid term has been used on the transport of carbon dust particles.

We make two assumptions: (I) The dust particle mass is much larger than that of a gas molecule, i.e. $m_D >> m_g$, where m_D and m_g are the masses of single dust and neutral molecules, respectively. (II) The neutral gas molecules have velocities distributed after the Maxwell-Boltzmann distribution, thus in one dimension we obtain:

$$f(v_g) = \left(\frac{m_g}{2\pi k_B T_g} \right)^{\frac{1}{2}} \exp\left(-\frac{m_g v_g^2}{2 k_B T_g} \right) \tag{4.13}$$

where f is the probability density described in appendix A.

We consider a small flat surface element of a dust particle which moves through a gas with velocity $\vec{v}_d$. Let the geometry be defined spherically, such
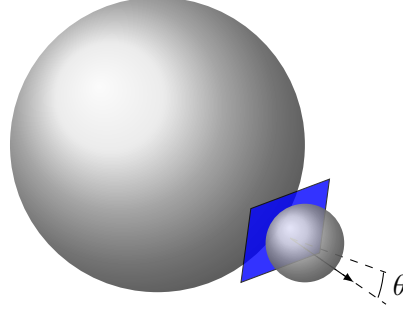
Figure 4.3: Schematic of geometry in collision between large dust particle and gas molecule. The relative sizes are not in scale.

that the polar axis is defined as the normal of the surface element. If the dust moves at an angle θ to this normal, as shown in figure 4.3, the transfer of momentum to the dust grain in the polar direction becomes:

$$\Delta p = 2m_g(v_g + v_d \cos\theta) \tag{4.14}$$

where we have used the assumption that $m_D \gg m_g$.

We take into account the maxwellian nature of the neutral gas molecules, by using eg. (4.13). The probability of a gas molecule having a speed between v_g and $v_g + \mathrm{d}v_g$ in one (the polar) direction is then:

$$f(v_g \rightarrow v_g + \mathrm{d}v_g) = \frac{1}{(\pi)^{\frac{1}{2}} v_{th,g}} \exp\left(-\frac{1}{2}\frac{v_g^2}{v_{th,g}^2}\right) \mathrm{d}v_g \tag{4.15}$$

where $v_{th,g} = (2k_B T_g/m_g)^{\frac{1}{2}}$ is the thermal velocity of the neutrals.

A small surface area of the surface of the dust grain is in spherical coordinates given as $\mathrm{d}A = r_d^2 \sin\theta\mathrm{d}\theta\mathrm{d}\phi$, where r_d is the dust grain radius, and ϕ is the azimuthal coordinate. The collision frequency of neutral molecules on the surface element can be obtained as:

$$\nu_{g,d} = n_g(v_g + v_d \cos\theta)\frac{1}{(\pi)^{\frac{1}{2}} v_{th,g}} \exp\left(-\frac{1}{2}\frac{v_g^2}{v_{th,g}^2}\right) \mathrm{d}v_g \mathrm{d}A \tag{4.16}$$

where n_g is the neutral gas density. The momentum transfer per unit time along the polar axis is subsequently yielded by multiplying with the term from eq. (4.14):

$$\frac{\Delta p}{\Delta t} = 2m_g n_g(v_g + v_d \cos\theta)^2 \frac{1}{(\pi)^{\frac{1}{2}} v_{th,g}} \exp\left(-\frac{1}{2}\frac{v_g^2}{v_{th,g}^2}\right) \mathrm{d}v_g \mathrm{d}A \tag{4.17}$$

The component of this force perpendicular to the grain velocity direction will be cancelled through integration over the entire grain surface, thus the drag can be stated as:

$$2m_g n_g r_d^2 (v_g + v_d \cos \theta)^2 \frac{1}{(\pi)^{\frac{1}{2}} v_{th,g}} \exp \left(-\frac{1}{2} \frac{v_g^2}{v_{th,g}^2} \right) \mathrm{d}v_g \sin \theta \cos \theta \mathrm{d}\theta \mathrm{d}\phi \quad (4.18)$$

We obtain the total drag by integrating over all neutral velocities. If $v_g > v_d$, collisions will happen for all collision angles θ, however if $v_g \leq v_d$, collisions will only happen if $\cos \theta > -v_g/v_d$. By using this, we may combine the supersonic and subsonic terms, and we state the total drag as:

$$2m_g n_g r_d^2 \frac{1}{(\pi)^{\frac{1}{2}} v_{th,g}} (I_1 + I_2) \quad (4.19)$$

where the integrals I_1 and I_2 are valid for the different velocity regimes:

$$I_1 = \int_0^{2\pi} \int_{v_d}^{\infty} \int_0^{\pi} \mathrm{d}\phi \mathrm{d}v_g \mathrm{d}\theta (v_g + v_d \cos \theta)^2 \exp \left(-\frac{1}{2} \frac{v_g^2}{v_{th,g}^2} \right) \sin \theta \cos \theta$$

$$I_2 = \int_0^{2\pi} \int_{-v_d}^{+v_d} \int_0^{\cos^{-1}(-\frac{v_g}{v_d})} \mathrm{d}\phi \mathrm{d}v_g \mathrm{d}\theta (v_g + v_d \cos \theta)^2 \exp \left(-\frac{1}{2} \frac{v_g^2}{v_{th,g}^2} \right) \sin \theta \cos \theta$$

These integrals can be calculated in terms of the relative flow of the background neutrals to the dust grain. The final result for the drag term, after inserting for the integrals, then becomes:

$$\vec{F}_{drag} = \pi r_d^2 m_g n_g v_{th,g} (\vec{v}_g - \vec{v}_d) \frac{1}{u} \left\{ \frac{1}{\sqrt{\pi}} \left(u + \frac{1}{2u} \right) \exp(-u^2) \right.$$

$$\left. + \left(1 + u^2 - \frac{1}{4u^2} \right) \mathrm{erf}(u) \right\} \quad (4.20)$$

where $u = |\vec{v}_d - \vec{v}_g|/v_{th,g}$ is the normalized relative atom flow speed.

4.3.2 Estimation of drag coefficient

The drag coefficient, i.e. the C_D-term in eq. (4.10), is often used without particular justification in papers concerning simulation of dust motion, and the hard sphere approximation of $C_D = 0.5$ have been used without further discussion. Drag on a nanometer-scale particle is an abstract concept, especially in the free molecular flow regime. The drag coefficients for other flow regimes than viscous flows, are in fact empirical extensions to the works of Stokes [1851] regarding viscous flows.

The drag coefficient can be estimated through flow parameters calculated from the neutral gas simulations inside MUDD. A key parameter in quantifying flow regimes is the Reynolds number, which is defined as the ratio between the inertial and viscous forces. It advantageous to define this number in terms of the Knudsen number, which we defined above, however this is not the most recognized form. In appendix B we therefore derive the relationship between the Reynolds number, Knudsen number and Mach number which is more intuitive than normal formulations, at least for our purposes. The result, as given in eq. (B.7), becomes:

$$Re = \frac{Ma}{Kn} \left(\frac{\gamma\pi}{2}\right)^{\frac{1}{2}} \tag{4.21}$$

where Ma is the Mach-number, Kn is the Knudsen number and γ is the ratio of specific heats. This number is however not well defined for very small (sub-micro scale) particles, as they can slip between collisions when the Knudsen number is high. If the characteristic dimension of the system is the particle diameter, a correction factor, the *Cunningham slip correction*, C_c is given as:

$$C_c = 1 + Kn \left[\alpha + \beta\exp\left(-\frac{\delta}{Kn}\right)\right] \tag{4.22}$$

where the coefficients α, β and δ are found experimentally. Hutchins et al. [1995] measured the values $\alpha = 1.2310$, $\beta = 0.4695$ and $\delta = 1.1783$ for spherical particles. We note that the linear dependence on the Knudsen number may introduce a large slip correction factor for nano-scale particles in free molecular flow.

Stokes [1851] introduced what is now as known Stokes' law (see eq. (4.8)) for viscous flow, and the drag coefficient may thereof be defined as:

$$C_D = \frac{24}{Re} \tag{4.23}$$

which is valid for small Re. Numerous extensions of this based on experimental data have been introduced to cover certain ranges of Re. Langmuir et al. [1946] give the expression

$$C_D = \frac{24}{Re} \left(1 + 0.197Re^{0.63} + 0.0026Re^{1.38}\right), \qquad Re \le 100; \tag{4.24}$$

Schiller and Naumann [1933] showed:

$$C_D = \frac{24}{Re} \left(1 + 0.15Re^{0.687}\right), \qquad Re \le 700; \tag{4.25}$$

and a for higher Re, Ihme et al. [1972] have shown:

$$C_D = \frac{24}{Re} + \frac{5.48}{Re^{0.573}}, \qquad Re \le 30000. \tag{4.26}$$

The results can be combined to make a complete picture of how the drag coefficient behaves as a function of the Reynolds number. Figure 4.4 shows C_D for the introduced ranges of Re, with a further extension for even higher numbers. The rule of thumb is that $C_D \approx 0.44$ for large Re, which can be observed in the range $[10^3, 10^5]$.
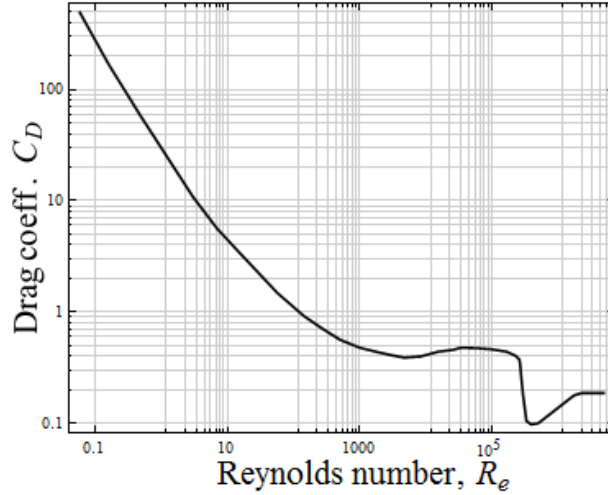

Figure 4.4: Drag coefficient versus particle reynolds number for smooth spherical particles. Interpolated data for C_D is from Wolfram [2013].

For dust particles in MUDD, we extract the gas properties from the neutral gas simulations to calculate Re. For a quasi-steady state solution of neutral flow in MUDD, as presented in the results, a first estimate places Re in the range 15-45, which yields an estimate of C_D right above unity, cf. figure 4.4. The large uncertainty in the range comes from the uncertainty and anisotropy of local gas parameters in MUDD.

4.3.3 Dynamic shape factor

A rigorous calculation of nano-scale dust dynamics must correct for the enhanced drag force which is introduced for non-spherical particles. Fuchs [1965] was the first to introduce a correction factor to the drag term as the ratio of the resistance force, i.e. neutral air drag, on a non spherical particle to the force on its volume equivalent sphere:

$$\chi = \frac{F_D^p}{F_D^{ve}} \qquad (4.27)$$

Both particles are assumed to move as the same relative velocity to the ambient gas. For micro-scale dust particles in viscous flows χ can be determined fairly accurate since the techniques for production and measurement

of such particles are well developed; see e.g. [Wu, Zhangfa and Colbeck, I., 1996]. The current studies of dynamic shape factors for meteoric smoke analogues of sub-micron radii are limited [Saunders et al., 2010; DeCarlo et al., 2004], although the results from different studies can be extrapolated to the nano-regime and yield a good approximation.

We introduce the *volume equivalent diameter*, d_{ve}, as the diameter of a volume equivalent sphere of a non-spherical dust grain. Another characteristic measure for the shape factor is the *electrical mobility diameter*, d_m, which is the diameter of a particle which migrates with the same velocity in a constant electric field as the non-spherical particle. This is important because it is the diameter which is measured by differential mobility analyzers (DMA) and particle sizers (SMPS) often utilized in studies of nano-scale particles (see e.g. Kulmala et al. [2004]). A non-spherical particle will experience a larger drag force, but the same electrical force compared to its volume equivalent sphere [DeCarlo et al., 2004], thus for non-spherical particles $d_m > d_{ve}$. The summary of different dynamic shape factors based on the detailed work of DeCarlo et al. [2004] is given in table 4.1.

This thesis will mainly treat the dust particles as spherical, because nearly spherical agglomerates, solid or amorphous, with or without voids, have $\chi \approx 1$ [DeCarlo et al., 2004; Saunders et al., 2010]. Also, in a collision process, is is plausible that agglomerates and oblate structures can become more spherical because large torques on elongated parts of the grain may possibly break them off. However, the enhanced drag effect might play a role in MUDD, and will therefore be addressed. It must be noted that certain agglomerates can have shape factors a few times larger than the ones listed in table 4.1 even for the same elements present in chondritic meteors [Colbeck, 1998], and the shape factor may therefore introduce a significant uncertainty.

4.4   Energy balance for evaporating particles

Our model includes the coupled terms for temperature and radius rate of change to map the possible effects of evaporation of fragments between G2 and BP in MUDD (see figure 3.1). For particles of smaller radii, on the order of 1-3 Ångstrøm, which are likely to stop completely due to neutral drag, evaporation may have an considerable effect. Knowledge about evaporation will furthermore bring useful corrections to the first approximation size distributions of the incoming fragments at BP which may be obtained with the simple equations of dust motion alone.

The primary energy balance equation for one dust particle, on a slightly

Table 4.1: Dynamic shape factors and diameter relations for different shapes, inspired by DeCarlo et al. [2004]. Note that the factor for agglomerates given here applies for the meteoric smoke analogues which are investigated in this thesis

Particle type		Diameter relations	Dynamic shape factor, χ
	Sphere	$d_m = d_{ve}$	$\chi = 1$
	Sphere w/voids	$d_m = d_{ve}$	$\chi = 1$
	Agglomerates	$d_m > d_{ve}$	$\chi = 1.5 - 1.6$ [1]
	Dublet	$d_m > d_{ve}$	$\chi = 1.12$ [2]
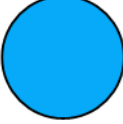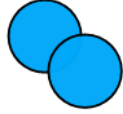
[1] Values from Saunders et al. [2010] used for nano-scale chondritic products (Fe_2O_3, SiO_2 and MgO).

[2] From Fuchs [1965]

augmented form from the one of Horanyi et al. [1999], is:

$$\underbrace{\pi r_d^2 n_g v_{th,g} \cdot k_B T_g}_{P_N} = \frac{4\pi}{3} \rho_d r_d^3 c_p \frac{dT_d}{dt} + L_d \frac{dm_d}{dt} \qquad (4.28)$$

where the term P_N on the l.h.s. can be interpreted as the heating power due to collisions with neutrals; the first term on the r.h.s. is the heat due to increasing temperature and the last term on the r.h.s. is the heat due to vaporization of the dust grain. The absorption of solar and terrestrial rays are ignored. The parameter n_g is the neutral density, $v_{th,g}$ is the thermal velocity of neutrals, T_g is the neutral gas temperature, c_p is the specific heat and L_d is the latent heat of vaporization of a grain. The specific heats used in this study are $c_p^{ice} = 7.49T_d + 90 J kg^{-1} K^{-1}$ [Klinger, 1981] and $c_p^{smoke} = 10^3 J kg^{-1} K^{-1}$ [Hunten et al., 1980]. The latent heats of vaporization used, are the same as those given for eq. (2.1).

As for the drag term, it is possible to modify the the term for heating power due to collisions with neutrals to fit better with dust simulations and

a wider range of velocities. We modify the term P_N from eq. (4.28) with a factor developed for transport of carbon dust by Smirnov et al. [2007], which can be derived in a similar way as the drag term from section 4.3.1, but only with diffusive ejection of the surface molecules. The improved term is named $\hat{P}_N$, and we have:

$$\hat{P}_N = P_N \cdot \frac{1}{4} \left\{ \frac{2}{\sqrt{\pi}} \left[5 + 2u^2 \right] \exp(-u^2) \right.$$

$$\left. + \frac{1}{\sqrt{u^2}} \left[3 + 12u^2 + 4u^4 \right] \operatorname{erf}(u) \right\} \tag{4.29}$$

where the dimensionless parameter $u = ||\vec{v_d} - \vec{v_g}|||/v_{th,g}$ is the ratio between the relative dust speed and thermal speed of the neutrals, and **erf** is the error function. As may have been noted, we do not take into account the thermal radiation from dust particles, as we operate on very short timescales. However, there is then a possibility that the dust heating can be slightly overestimated.

The next two sub-sections justify the uncoupling of the time evolution of dust temperature from the evolution of radius through the energy balance equation and kinetic theory.

4.4.1 Rate of change of dust radius

The mass of a dust grain can be expressed in terms of radius and mass density as $m_d = 4\pi\rho_d r_d^3/3$. Thus we may state

$$\frac{\mathrm{d}m_d}{\mathrm{d}t} = \frac{\mathrm{d}}{\mathrm{d}t} \left(\frac{4\pi\rho_d r_d^3}{3} \right) = 4\pi r_d^2 \rho_d \frac{\mathrm{d}r_d}{\mathrm{d}t}$$

$$\Rightarrow \frac{\mathrm{d}r_d}{\mathrm{d}t} = \frac{1}{4\pi r_d^2 \rho_d} \frac{\mathrm{d}m_d}{\mathrm{d}t}. \tag{4.30}$$

The time derivative of dust mass may be stated generally for any dust species d as proportional to the product of mass flux and the evaporating area A. We have that:

$$\frac{\mathrm{d}m_D}{\mathrm{d}t} = m_d A \Gamma_d \tag{4.31}$$

where m_D is the mass of one grain of a species d (generally ice or smoke), $A = 4\pi r_d^2$ is the evaporating area (assumed to be the total surface area of the grain) and Γ_d is the particle flux at which atoms leave the surface at a given vapor pressure $P(T_d, r_d)$ from eq. (2.3).

The particle flux Γ_d is found by assuming that a surface molecule leave a grain diffusively, and that there is a local thermodynamic equilibrium

(LTE) in the region between G2 and BP. This is however a bold claim which is often not true for gas the molecular or transitional flow regime, and thus deviations from LTE may occur in turbulent regions. In LTE the gas velocities are distributed as a Maxwell-Boltzmann distribution, which has the one-dimensional formulation in velocity space:

$$f(v_\xi) = \left(\frac{m_D}{2\pi k_B T_d} \right)^{\frac{1}{2}} \exp \left(-\frac{m_D v_\xi^2}{2 k_B T_d} \right) \tag{4.32}$$

where m_D is the mass of *one* atom or molecule of species d, v_ξ is the velocity of an escaping surface molecule in an arbitrary dimension ξ. Note that the characteristic temperature of the atoms is the dust temperature T_d. We have assumed that the neutral background velocity field is zero in all directions, so that the flux within a time interval Δt of escaping molecules can be calculated as the first order moment of the distribution; in other words:

$$\Gamma_d = \frac{\#\text{molcs. leaving}}{A \cdot \Delta t} = \frac{n_d A \Delta t \int_0^\infty \mathrm{d}\xi \cdot v_\xi f(v_\xi)}{A \Delta t} \tag{4.33}$$

where n_d is the number density of the evaporating species. A quick substitution of variables using $m_D v_\xi^2 / 2 k_B T_d$ as kernel gives the flux:

$$\Gamma_d = n_d \int_0^\infty \mathrm{d}v_\xi v_\xi f(v_\xi) = n_d \left(\frac{m_D}{2\pi k_B T_d} \right) \int_0^\infty v_\xi \exp \left(-\frac{m_D v_\xi^2}{2 k_B T_d} \right).$$

This integral can be solved using $\int_0^\infty y e^{-\beta y^2} dy = 1/2\beta$, which yields

$$\Gamma_d = n_d \left(\frac{k_B T_d}{2\pi m_D} \right)^{\frac{1}{2}} = n_d k_B T_d \left(\frac{1}{2\pi m_D k_B T_d} \right)^{\frac{1}{2}}.$$

The first part is nothing more than the vapor pressure defined in eq. (2.3), such that

$$\Gamma_d = P_{vap}(T_d, r_d) \left(\frac{1}{2\pi m_D k_B T_d} \right)^{\frac{1}{2}}. \tag{4.34}$$

The final expression for the the derivative of dust radius is obtained by substituting eq. (4.34) into eq. (4.31) and subsequently into eq. (4.30), which yields:

$$\frac{\mathrm{d}r_d}{\mathrm{d}t} = -\frac{P_{vap}(T_d, r_d)}{\rho_d} \left(\frac{m_D}{2\pi k_B T_D} \right)^{\frac{1}{2}} \tag{4.35}$$

4.4.2 Rate of change of dust temperature

The starting point for the derivation of the expression for temperature evolution is to insert the modified energy balance equation obtained from eq. (4.29) into the primary equation, eq. (4.28). Rearranging yields:

$$\frac{\mathrm{d}T_d}{\mathrm{d}t} = \left(\hat{P} - L_d \frac{\mathrm{d}m_d}{\mathrm{d}t} \right) \bigg/ \frac{4\pi}{3} \rho_d r_d^3 c_p \qquad (4.36)$$

where the quantities T_d, m_d, r_d, L_d and ρ_d still denote the temperature, mass, radius, latent heat of vaporization and mass density for a dust species d respectively. $\hat{P}$ is the modified heating power, i.e. the time derivative of the contributed collision energy, due to collisions with neutrals from eq. (4.29).

The mass derivative on the r.h.s. may be expressed in characteristic parameters of the dust by first rewriting the derivative of mass in terms of the derivative of radius given in eq. (4.30) and secondly inserting the expression for the derivative of radius from eq. (4.35). The final expression for time evolution of dust temperature T_d then becomes:

$$\frac{\mathrm{d}T_d}{\mathrm{d}t} = \left(\hat{P} - L_d \cdot 4\pi r_D^2 \left(\frac{m_D}{2\pi k_B T_d} \right)^{\frac{1}{2}} \cdot P_{vap}(T_d, r_d) \right) \bigg/ \frac{4\pi}{3} \rho_d r_d^3 c_p \quad (4.37)$$

4.5 Details of the numerical computations

The physical framework of our problem is the summer mesospheric conditions under which NLC particles typically form. The most important characteristic parameters which defines such an environment, and thus are used in the numerical simulations, are listed in the following.

Parameters in E-field model

The E-field system is solved, as mentioned, with a finite element method (FEM) with an adaptive mesh and Dirichlet boundary conditions. The physical parameters, e.g. the permittivity, of the system are defined for air at standard temperature and pressure as given by the FEM software.

Parameters in DSMC model (neutral gas)

Parameter	Value	Note
Altitude, h	82 km	
Ambient gas density, n_g	$4.12 \cdot 10^{20} \text{m}^{-3}$	Rapp et al. [2001]
Ambient temperature, T	150 K	Rapp et al. [2002]
Rocket velocity, v_R	750 ms^{-1}	
Bucket temperature T_B	350 K	
Mean mass of neutrals, m_g	29 a.m.u	79/21 N_2/O_2 mix

Parameters in dust dynamics model

Parameter	Value	Note
MSP mass density, ρ_s	3000 kgm^{-3}	Discused in 3.5.2
Ice mass density, ρ_i	980 kgm^{-3}	
Mean dust weight, m_D	140 a.m.u	For MSPs
Dynamic shape, χ	$1 - 1.5$	See table 4.1
Drag coefficient, C_D	1	
Initial fragment velocity, v_0	450 ms^{-1}	Tomsic [2001]
Latent heat of vaporization of ice , L^{ice}	$2.78 \cdot 10^6 Jkg^{-1}$	Lichtenegger and Kömle [1991]
Latent heat of vaporization of MSP , L^{smoke}	$6 \cdot 10^6 Jkg^{-1}$	
Specific heat of ice, c_p^i	$90 + 7.5T_d Jkg^{-1K^{-1}}$	Klinger [1981]
Specific heat of smoke, c_p^s	$1000 Jkg^{-1K^{-1}}$	Hunten et al. [1980]
Mean surface energy of smoke, $\bar{\gamma}_{smoke}$	0.200 Jm^{-2}	Gundlach et al. [2011]
Surface energy of ice, γ_{ice}	0.190 Jm^{-2}	Heim et al. [1999]

Chapter 5

Results

In this chapter, the results from simulations done on the basis of the theoretical model are presented. The electric field solutions are presented for the potential modes which exist in the present design of MUDD, i.e. for a varying bottom plate potential of 0 and $\pm 10V$ corresponding to retarding potentials of 10, 0 and 20V for negatively charged particles. The primary objective of the E-field simulations is to map the edge effects and how field lines connect to the probe walls, which is a modestly explored effect that might induce unwanted movement in MUDD. For the fragment dynamics simulations, which are especially emphasized in this thesis, an idealized field based on the E-fieldsimulations will be used (as presented in sec. 3.3), as certain edge effects may introduce numerical instabilities. The solutions from the Monte Carlo procedure on the ambient gas, provided by the methods introduced in [Bird, 1994], are presented for neutral gas parameters corresponding to conditions in the summer mesosphere at an altitude of 82 km. The derived neutral gas density in MUDD will subsequently be used throughout the dust simulations. The solutions for dynamics of dust fragments will be presented for a number of different parameters; mainly for a varying bottom plate potentials and different particle types. Dust movement in the present potential modes of MUDD is presented, with aim to assess its detecting capabilities. Furthermore, we present the solutions for alternative potential modes, i.e. lower bottom plate potentials, to investigate whether the sensitivity of the present MUDD probe can be significantly improved. Different particle shapes and hybrid compositions of MSPs and ice are also investigated.

5.1   Electric field solutions

The E-fields were calculated by solving the Lagrange equation in a rotationally symmetric system with a finite element procedure provided by COMSOL. Boundary potentials were assigned as a Dirichlet condition, i.e. volt-

ages were assigned to linear edge segments. The system was solved for a global temperature of 293 K, and the relative permittivity was set to unity; $\epsilon_r = 1$. It must be noted that this temperature is probably different from the real temperature in MUDD. However, the real conditions will never constitute a thermal equilibrium and the solution is nevertheless not strongly dependent on the temperature.

Figure 5.1 shows the primary detection mode of MUDD, where the bottom plate voltage is $V_{BP} = 0V$ which constitutes a retarding potential of 10 V for negatively charged particles. It is found that the average field value between G2 and BP is approximately $1100 \mathrm{Vm}^{-1}$ if we waive the enhanced fields on the sharp edges. This value is approximately 50 Vm^{-1} lower than the infinite conducting plane solution. The value inside G2 (between the concentric rings) varies from approximately 0 Vm^{-1} at the concentric ring closest to the center to some 10 Vm^{-1} at the outermost ring. This solution is not worryingly divergent from the zero-field solution from the inside of an infinite conducting plane. However, as will be discussed below, certain edge fields may be comparable in size to the fields between G2 and BP and introduce unwanted effects in fragmentation on the outer ring.
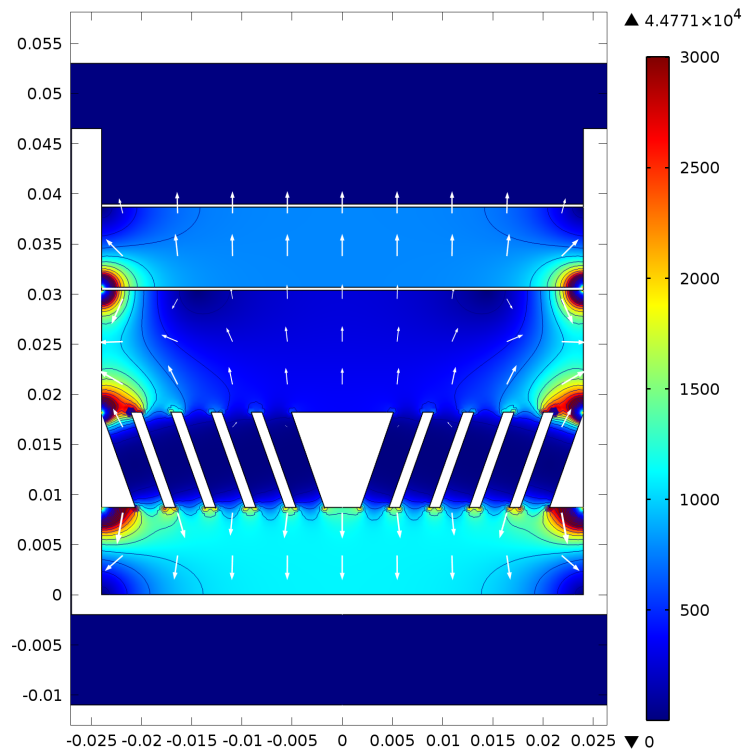

Figure 5.1: Electric fields in MUDD for a bottom plate potential of $V_{BP} = 0V$. We must note that the colorbar has a cut-off at 3000 Vm^{-1} and that arrows are logarithmically scaled.

Strong electric fields on different edges and corners are abundant, and every concentric ring of G2 can be observed to have strong fields at the top and bottom. These fields, which are only a few 100 Vm^{-1} larger than the retarding fields between G2 and BP, are in general not strong enough to have a large effect on particles with the energies that NLC particles and their fragments will have. Nevertheless, the enhanced field on the edges of G2 and below and above G2 at $r \approx \pm 0.24$ m are observed to be significantly larger than the retarding fields by factors of over 40 (!). The radial field strength, as shown in fig. 5.2, dominates, causing a substantial coupling of field lines to the probe walls. Regardless, it must be noted that NLC particles are relatively energetic and negatively charged, so the effect the large E-fields have on them will be small; because of the outward direction of the fields. The fragments on the other hand, have much lower energies, and there are areas on the top and bottom of G2 with strong radial fields in the $-\hat{r}$-direction which may possibly act as strong sinks for negatively charged fragments with low energy. If this effect reduces the effective area of G2 significantly, the secondary charging effect, as described in e.g. [Havnes and Næsheim, 2007; Kassa et al., 2012], can be significantly underestimated.
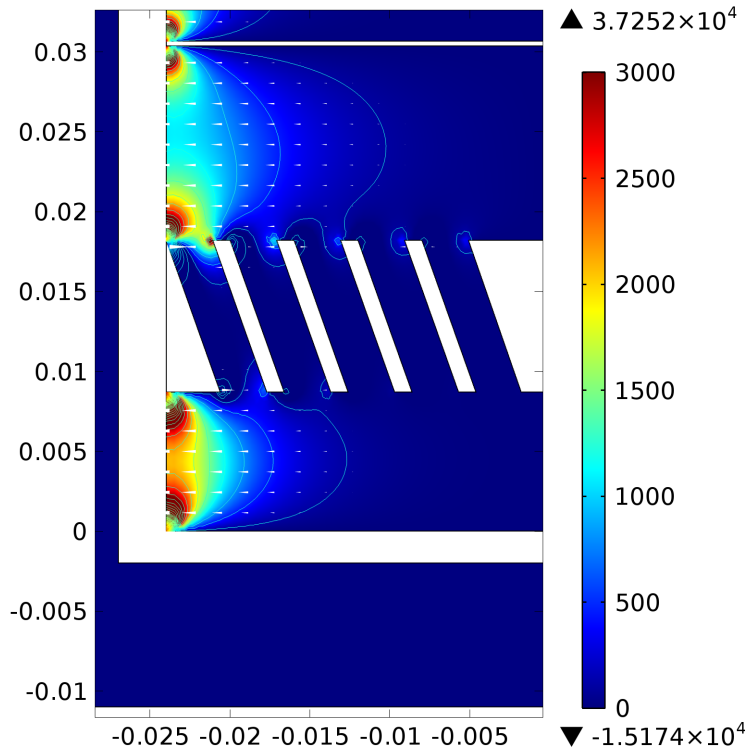

Figure 5.2: Electric fields in the radial direction for $V_{BP} = 0V$. Arrow length is Log-scaled.

Figure 5.3a shows a close-up of edge fields at the top of the outermost concentric ring of G2. The top of the inclined impact surface is seen to have a strong field which will attract negative fragments if the energy is small enough. In figure 5.3b an anomaly caused by the connection of field lines to the wall from the G1-grid can be seen. We observe two areas where the field strength is reduced to almost zero. The possible effect from this anomaly will presumably be small on the energetic NLC particles.

(a) Enhanced fields at the top   (b) Anomaly in G1–G2 field.
   outer boundary of G2.
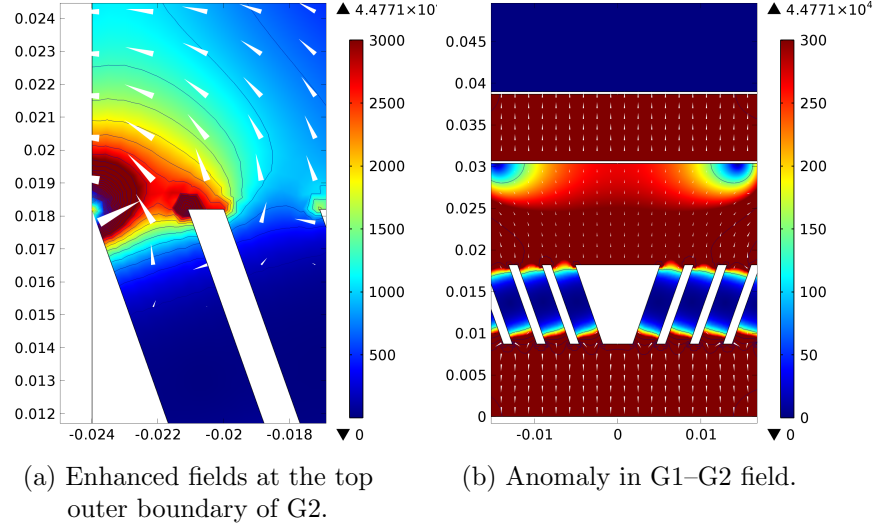
Figure 5.3: Close-up of anomalous field effects because of enhanced edge fields and field lines connecting to the walls.

In figures 5.4 and 5.5 the E-field solutions obtained for the other two potential modes in MUDD are shown. Figure 5.4 gives the solution for a bottom plate potential of $V_{BP} = -10$V, corresponding to a retarding potential of 20 V for negative fragments. This mode acts as a detection mode for the most energetic fragments. The electric fields inside and above G2 are virtually identical to the solution of $V_{BP} = 0V$, as expected. The mean field value between G2 and BP is approximately 2200 Vm^{-1}, again almost five percent lower than the infinite conducting plane solution. The edge effects are amplified in comparison with the first detection mode, and field strengths directly underneath the G2 rings are found to have values over 3400 Vm^{-1}, which is over 50% larger than the mean retarding fields between G2 and BP. A close-up comparison of edge effects between the two so-called detection modes is shown in figure 5.6.

Figure 5.5 shows the obtained solution for the third potential mode, or reference mode, where the field between G2 and BP is intended to be zero so that the total fragment current can be measured. The field between G2 and BP is observed to vary rather strongly with r in this mode. In the area below the innermost concentric ring, the average field value is approx-

imately 5 Vm^{-1}, while towards the outermost ring the field value reaches over 1500 Vm^{-1}. However, the E-field is mainly radial in the $\hat{r}$-direction so negative fragments will be deflected from the walls. Still, we observe that the strongest vertical fields beneath G2 may be strong enough to introduce a significant deceleration of negative fragments at the two outermost rings.
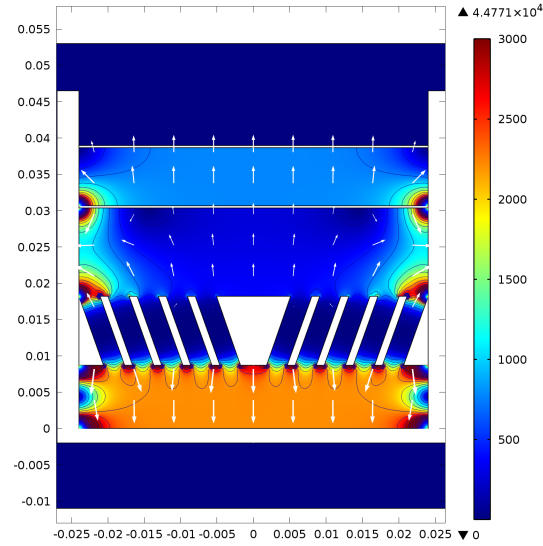
Figure 5.4: Electric fields in MUDD for a bottom plate potential of $V_{BP} = -10V$. The arrows are logarithmically scaled.
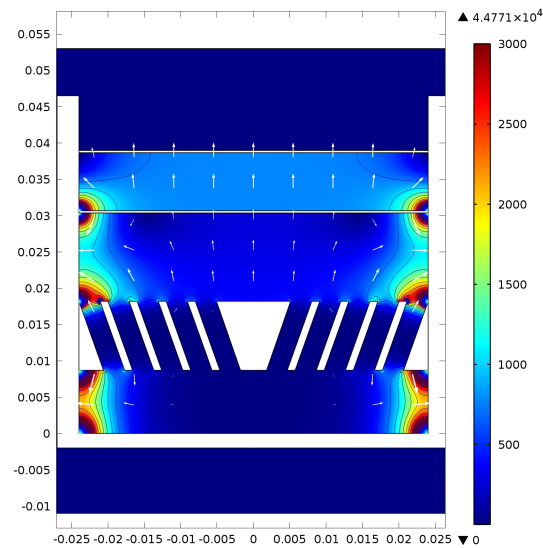
Figure 5.5: Electric fields in MUDD for a bottom plate potential of $V_{BP} = 10V$. The arrows are logarithmically scaled.

Figure 5.6 shows a comparison of the E-field edge effects for the two detecting (retarding) potential modes, $V_{BP} = 0V$ and $V_{BP} = -10V$. The difference lies mainly in that edge effects are much stronger in the latter mode in the area between G2 and BP. Electric fields with norms over 44000 Vm^{-1} exist for both modes, but will mainly act to repel negative particles from the probe walls and towards the probe center. The field direction around certain edges may however *attract* negative fragments, especially if the fragmentation of NLC particles takes place on the lowest or highest part of the outer concentric ring in G2, where the fields are large.

(a) $V_{BP} = 0V$ (b) $V_{BP} = -10V$
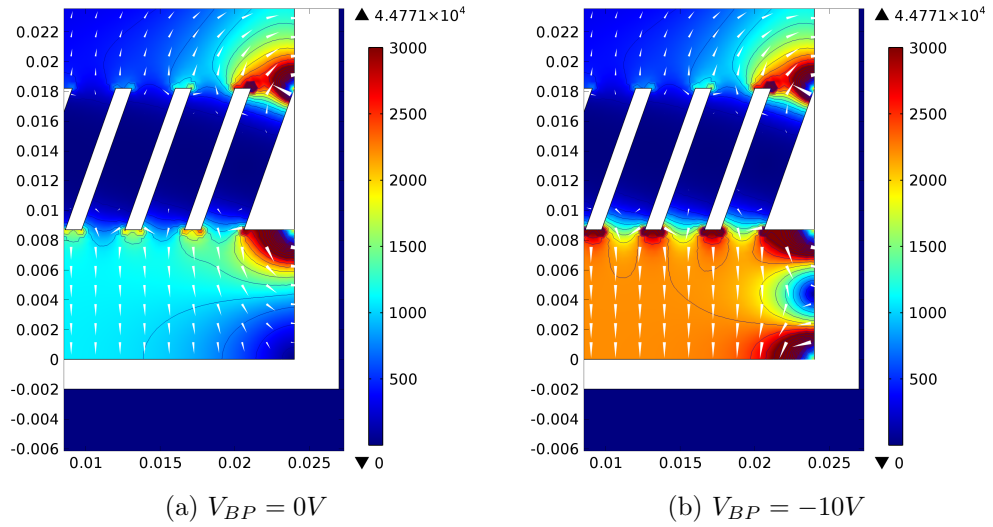
Figure 5.6: Comparison of edge E-fields for different potentials. The arrows are logarithmically scaled

5.2 Solutions for neutral gas movement

The neutral gas solutions are given for the set of parameters listed in section 4.5 which aim to replicate summer mesospheric conditions at an altitude of 82 km. The rocket velocity and MUDD bucket temperature are estimated based on earlier rocket flights. The DSMC was implemented to find steady flows at large times, i.e. averaging the flow over time which gradually reduces the statistical scatter as the sample increases [Bird, 1994].

In the figures 5.7 and 5.8 we present the obtained solutions for the number density and mass density, which can be derived consistently from one another. We observe a distinct shock front in which the number density is larger than the ambient number density by a factor of $3.75 - 5$. Such a shock front, where the gas is given a strong radial velocity, has previously been shown to transport free MSPs on the outside of probes so that only more inert particles (e.g. NLC particles) enter the bucket [Hedin et al., 2007]. The number density value throughout the MUDD bucket is fairly consistent with a mean value of $n_g = 2.5 \cdot 10^{21}$ m^{-3} in the areas inside G2 and between G2 and BP.
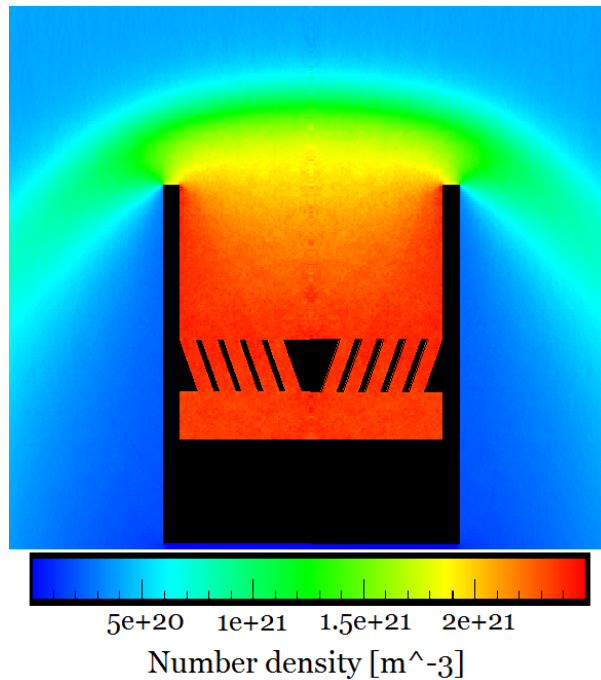
Figure 5.7: Number density of neutrals inside and around MUDD at 82 km.

The solution for the neutral gas temperature is shown in fig. 5.9. The strong compression in the shock gives rise to an increase in temperature in the bucket opening and the region around the probe. A noteworthy feature
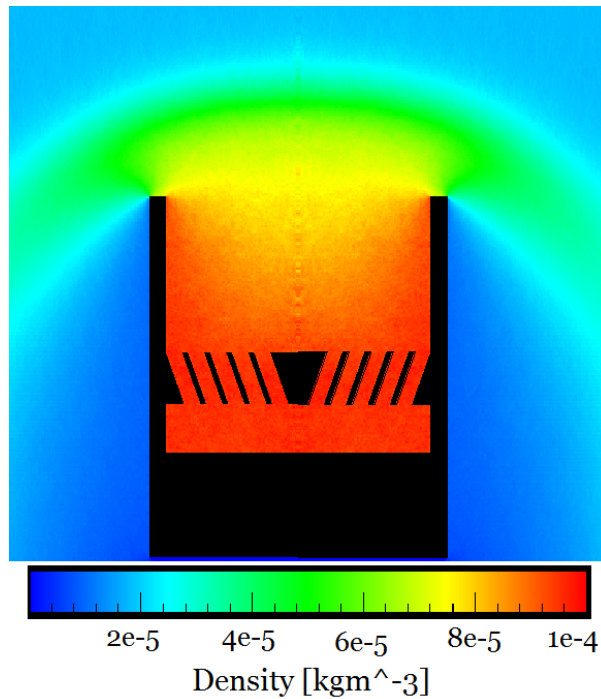
Figure 5.8: Density of neutrals inside and around MUDD at 82 km.

is the temperature in the bottom of the bucket. The air molecules are here
observed to have temperatures characteristic of the MUDD surface (set at
350 K), and they are observed to acquire this temperature quite rapidly,
i.e. well within the short integration time of the DSMC. This finding sup-
ports the use of a thermodynamic quasi-equilibrium in the dust movement
simulations with the background temperature set at the MUDD bucket tem-
perature (T_B in the text). An equilibrium will never be the case in practice,
and the temperature may not even be well defined if the local turbulence is
large enough [Horanyi et al., 1999], but it simplifies the numerical compu-
tations and is nevertheless a good approximation to the real situation.

The scalar pressure calculated from the gas parameters is shown in
fig. 5.10. The pressure is noted to be distributed homogeneously throughout
the probe volume. The mean value of approximately 11 Nm^{-2} is approxi-
mately 13 times as large as the ambient pressure. This value checks out to
be approximately equal to the ram pressure given by $P_{ram} \sim n_g m_g v_{rocket}^2$,
which is expected for probes without coning.

In figure 5.11, the background velocity field in terms of the radial and
vertical components are presented respectively. The vertical component is
only particularly expressed at the top of the probe, and varies between
values from around -7 ms^{-1} to +7 ms^{-1} inside the bucket. The radial
component have similar values inside the bucket, and the resultant velocity
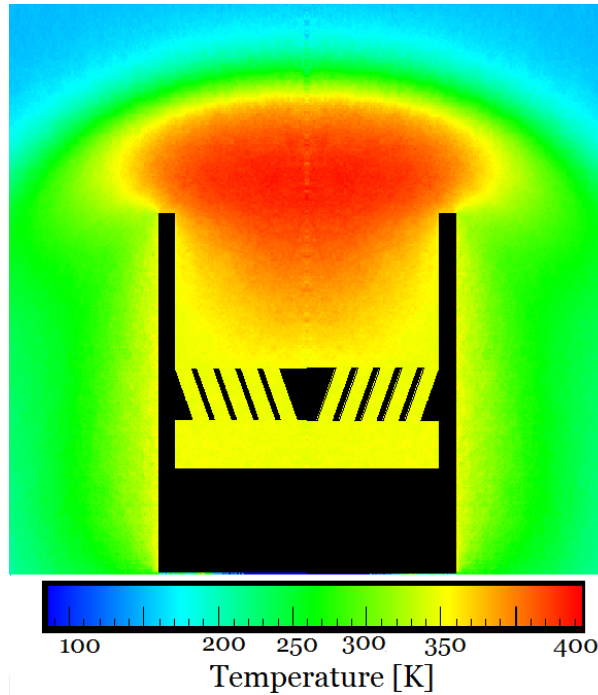
Figure 5.9: Neutral gas temperature inside and around MUDD at 82 km.
The ambient temperature is 150 K.

field between G2 and BP is turbulent with small velocities. It should be
noted that, when probing the values between G2 and BP, the measured
stream does not seem to acquire a significant radial component (on the
order of unity) due to the inclination of the G2 concentric rings, as would
be expected for larger particles. The question of what velocity field to use
further in the dust simulation is not trivial. A velocity grid from the neutral
gas simulations with a finite number of samples will naturally become quite
turbulent, almost stochastic because of the allowed resolution of the DSMC
procedure. Thus, since the velocities seem to average to zero (arguably with
a very small vertical component downwards ~ 1 ms^{-1}), we argue that the
velocity field is $\vec{0}$ in the fragmentation area between G2 and BP.

The table below summarizes the key gas parameters for the neutral gas
simulations which will be adopted to the dust dynamics simulations.

Table 5.1: Key gas parameters utilized in the charged dust fragment
simulations

Air number density, n_g	$2.5 \cdot 10^{21}$m^{-3}
Temperature in MUDD, T_B	350 K
Velocity of neutrals, $\vec{v_g}$	$\vec{0}$
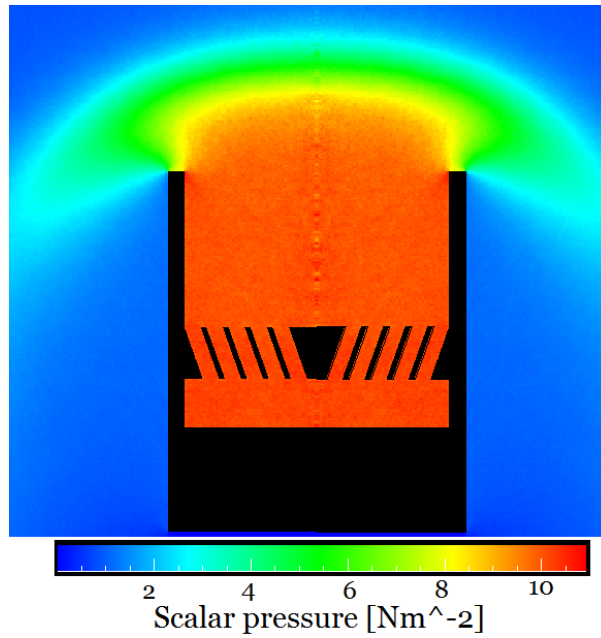
Figure 5.10: Scalar pressure in MUDD at 82 km deduced from the number density and temperature solutions.

(a) Vertical velocity field.

(b) Radial velocity field.
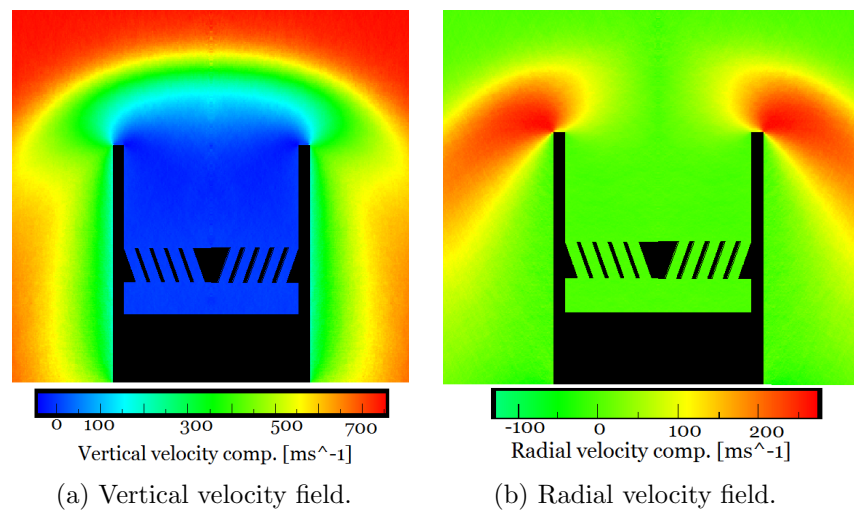
Figure 5.11: Velocity fields of neutrals inside the probe.

5.3   Solutions for singly charged dust fragments

From the extensive study of dust fragment dynamics between G2 and BP, we will in this section present the solutions obtained for the transport, heating and evaporation of different types of dust fragments in different retarding potentials. As justified in chapter 3.5, the results applies primarily for spherical MSPs of different sizes. However, results obtained from the extensions of the model for other fragment shapes and content (e.g ice layers of different sizes, and different MSP properties) will also be presented. The model parameters are summarized in the tables in chapter 4.5 and in table 5.1. The results are structured in such a way that solutions for a particular retarding potential are presented collectively. Simulations have been run for a uncertainty in velocity of $\pm 100 \text{ms}^{-1}$ for all particle types, as the one of the main sources of error lies in the estimated initial fragment velocity which is centered at 450 ms^{-1}. The retarding potential modes, i.e. the detecting modes, are presented first, succeeded by modes with lower bottom plate potentials. The reference mode, i.e. the case of no retarding potential, is presented subsequently and is followed by the solutions for non-spherical fragments. The nomenclature of the presentation is centered around energy in units of electron volts (eV) and hit percentage of charged fragments. These parameters can yield much information both alone or relative to the reference mode. This allows us to translate between the simulations and measurements of MUDD in the most practical way, and can be used to deduce the produced currents in MUDD. The obtained results from this study are summarized in tables at the end of their respective subchapter.

5.3.1   Dust fragments in a 10 V retarding potential

Meteoric smoke particles (MSP)

The fragmentation from G2 was discretized into 50 subintervals of one concentric ring ($[-0.182 \leq x \leq -0.0087]$ and $[0.013 \leq y \leq 0.1638]$) where the fragments were ejected from the surface of the ring at an angle of $6°$, with varying initial velocities.

Figure 5.12 shows the the traced path of 50 simulated fragments of pure MSP content with initial radius 1.6 nm, representing a typical simulation of singly charged dust. The 1100 Vm^{-1} retarding field is sufficient to brake and even reflect some of the fragments, and for this particular simulation, 54% of the fragments hit the bottom plate with energies ranging up to to 7.6 eV. This is to say that fragments from the bottom 54% of the G2 surface will hit BP. The reflected fragments will hit G2 from underneath and presumably loose their charge.

Figure 5.13 shows in the left panel the obtained temperature solution, and in the right panel the radius solution for the same 1.6 nm MSP-fragments. The MSP fragments are observed to accumulate heat throughout the inte-

gration time and the amount of accumulated heat varies little over the range
of initial positions from the G2 surface. The radius of the fragment is ob-
served to decrease with an insignificant amount; the observed dip in radius
towards the end of the integration time is only a few times the machine
precision.
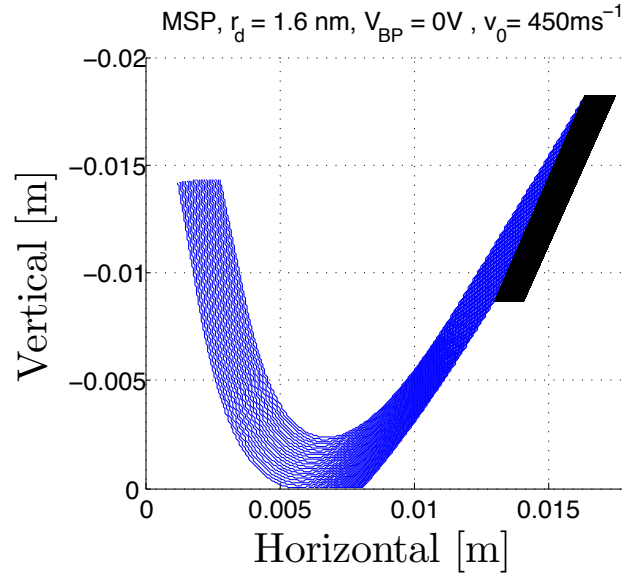
Figure 5.12: Traced flight path of spherical MSP fragments with initial
radius $r_0 = 1.6$ nm and initial velocity $v_0 = 450 \mathrm{ms}^{-1}$.
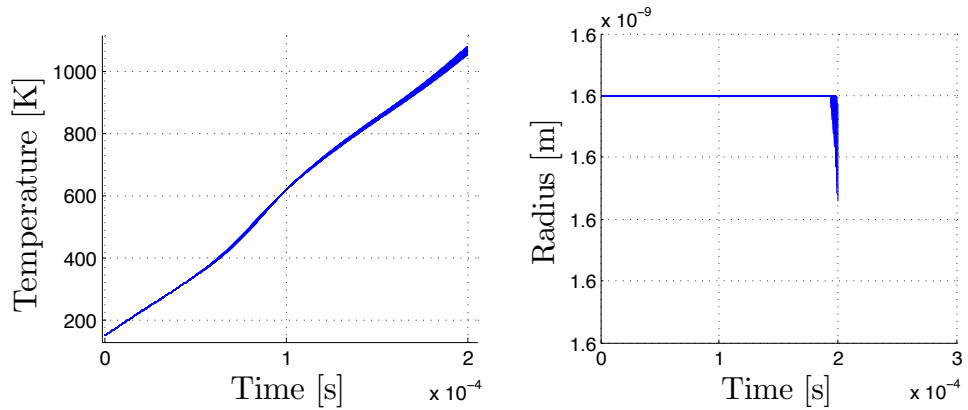
Figure 5.13: Temperature (left) and radius (right) as a function of time for
spherical MSP fragments with initial $r_0 = 1.6$. We note that this shows the
entire integration time of $2 \cdot 10^{-4}$ s, and the fragments hitting BP therefore
would have a much lower maximum temperature than the 1000 K as
shown here.

Figure 5.14 shows how the impact energy (particle energy at BP) varies with the initial position of the fragment. For the 1.6 nm MSP fragment, the radius does not change significantly and the energies will thus have an approximate linear relationship to the initial position. The $x-$position axis is read as length units above BP, so that the most energetic impacts are the ones coming from the lowest part of G2. Energy signatures like the present can be related to real MUDD data to some extent, and simplifies the comparison of simulation results and real life data. However, as is apparent in fig. 5.14, particles of the same radii yield a wide range of impact energies because of the strong dependence of initial position. A convenient way to overcome this ambiguity when comparing simulations, is to probe only the most energetic impact or the median energy impact to represent a particle of a given radius. In this manner, the 1.6 nm MSP fragment will be represented by an energy measure of 7.6 eV (most energetic) or 4.3 eV (median energy).
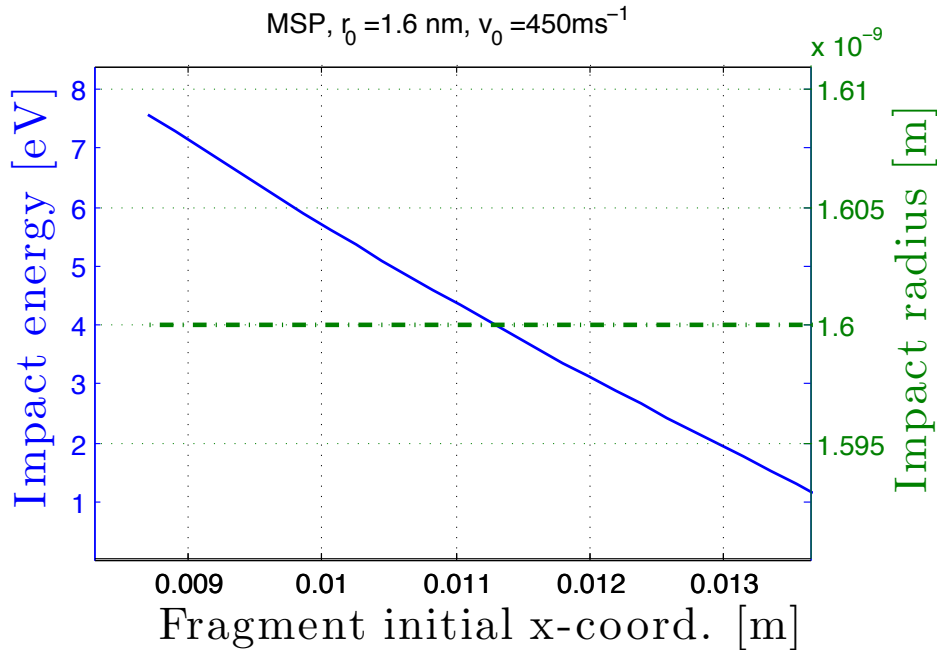
Figure 5.14: Impact radii and corresponding impact energy of 1.6 nm pure MSP fragments as a function of the initial height (above BP) at the G2 surface. The initial velocity is $v_0 = 450 \text{ms}^{-1}$.

In figure 5.15 we present the obtained solutions for impact energies of pure MSP fragments for a range of initial radii. The left panel shows the energies of the most energetic impacts for $v_0 = 450 \pm 100 \text{ms}^{-1}$. A broadening of the error band as a function of radius is observed. In the right panel, the same data is represented relative to the initial energy at G2. It is observed

that particles with an initial velocity of 550ms^{-1} keep respectively more of their initial energy than the 350 ms^{-1}-fragments loses, relative to the 450ms^{-1}-fragments. A non-linear relationship between relative energy and particle radius is observed, and larger particles with higher velocities may keep over half of their initial energy. It is also observed that a fragment with initial velocity 350 ms^{-1} must be 0.4 nm larger in radius than a fragment with initial velocity 450 ms^{-1} to obtain preserve the same relative energy, while the difference is only about 0.2 nm for the 550 ms^{-1}-fragments.
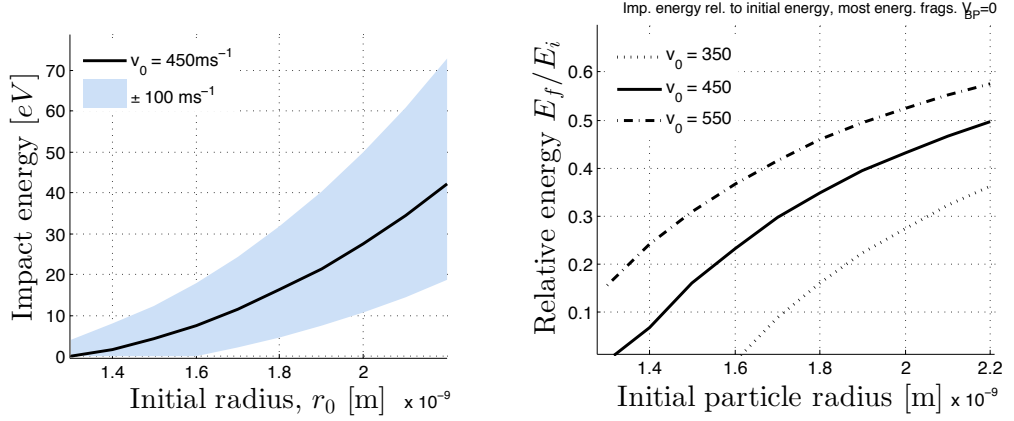
Figure 5.15: Numeric value of most energetic impacts (left panel) and the same values relative to initial energy (right panel) as a function of radius for pure MSP fragments. The ribbon (left) and dashed lines (right) represents the same values for an uncertainty in initial velocity of 100 ms^{-1}.

Different authors use different mass densities for MSPs [Rapp et al., 2007]; typically 2000 kgm^{-1} which is 1000 kgm^{-3} less than the mass density used in this thesis. We argued in chapter 3.5.2 why it is plausible that the density measure chosen here may be more realistic for MSPs. In figure 5.16 we give a comparison of hit percentages for different mass densities, where the specific weight used in this study is compared to fragments of lower densities. The relationship is observed to be approximately constant as a function of radius, and the 3000 kgm^{-1} fragment is seen to have a 40% higher hit percentage than the 2500 kgm^{-1} fragments, and another 40% higher hit count than fragments of density 2000 kgm^{-1}.

Table 5.2 summarizes the solutions obtained for pure MSP fragments in a 10V retarding field. This is one of the potential modes which currently exists in MUDD. As will be discussed later, when these solutions are compared to the solutions of the reference mode with no retarding fields, they may be directly transferred to MUDD. A detection limit of charged fragments may nevertheless be extracted directly out from the data. If we require that at least 30% of fragments must hit BP to be unambiguously detected,
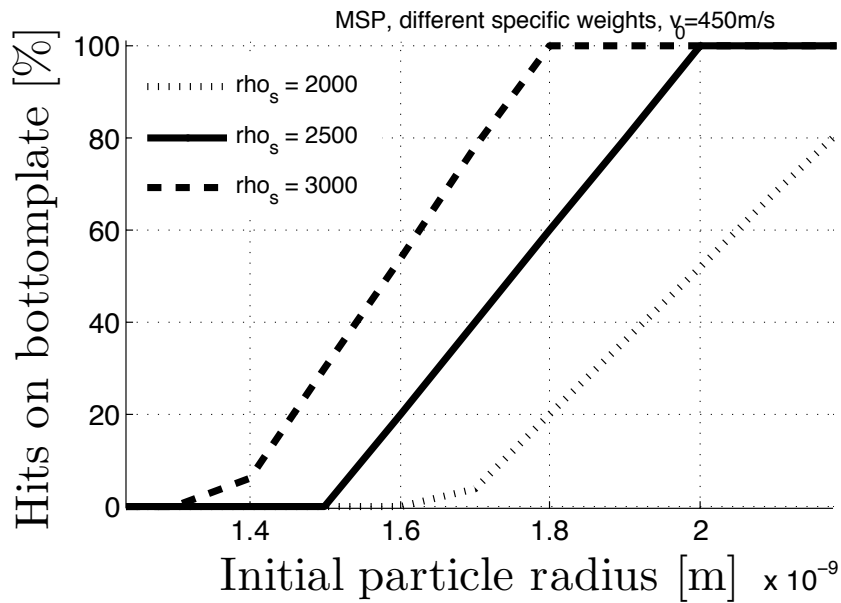
Figure 5.16: Hit percentages for pure MSP fragment of different specific weights in a 10 V retarding potential and with an initial velocity of 450 ms^{-1}.

the results yield that the particles have a minimum radius of 1.5 nm with bounds of 1.3 nm and 1.8 nm when the uncertainty in initial velocity is taken into account. The maximum detectable radius is correspondingly 1.8 nm bounded below by 1.6 nm and above by 2.2 nm due to the uncertainty in velocity. For larger radii, fragments will give yield equal currents, while fragments of radii smaller than the minimum limits, will yield currents equal to that of the reference mode.

Table 5.2: Impact radii and energies for pure MSPs at different initial velocities. The potential over BP is $V_{BP} = 0$V, i.e. a retarding potential of 10V for negatively charged particles. E_f denotes the energy range at impact. The intrinsic dust parameters are described in chapter 4.5.

$r_0[nm]$	$v_0 = 350m/s$		$v_0 = 450m/s$		$v_0 = 550m/s$	
	$E_f[eV]$	Hits [%]	$E_f[eV]$	Hits [%]	$E_f[eV]$	Hits [%]
1.2	—	0.0	—	0.0	—	0.0
1.3	—	0.0	—	0.0	$0.0 - 4.1$	28.0
1.4	—	0.0	$0.0 - 1.5$	6.0	$0.0 - 7.9$	58.0
1.5	—	0.0	$0.0 - 4.3$	30.0	$0.0 - 12.4$	86.0
1.6	—	0.0	$0.0 - 7.6$	54.0	$2.6 - 17.9$	100.0
1.7	$0.0 - 2.1$	12.0	$0.0 - 11.6$	78.0	$6.2 - 24.3$	100.0
1.8	$0.0 - 4.5$	32.0	$1.3 - 16.2$	100.0	$10.5 - 31.8$	100.0
1.9	$0.0 - 7.4$	50.0	$4.2 - 21.5$	100.0	$15.7 - 40.3$	100.0
2.0	$0.0 - 10.6$	70.0	$7.5 - 27.5$	100.0	$21.8 - 49.9$	100.0
2.1	$0.0 - 14.4$	90.0	$11.6 - 34.4$	100.0	$28.9 - 60.8$	100.0
2.2	$2.0 - 18.6$	100.0	$16.3 - 42.1$	100.0	$37.0 - 72.9$	100.0

MSP with a thin ice coating

For the 10V retarding potential, we shall also present results for MSP fragments with a thin layer of ice. As argued earlier, it is assumed that ice particles with a radius smaller than 3 nm tend to stick and eventually evaporate on the G2 surface. However, we want to investigate the possibility that MSPs may be coated with thin ice layers as they rebound from an NLC particle, and an elaboration of the potential influence such ice layers have on the measured fragment energies is helpful for analysis.

In figure 5.17 we present a comparison between pure MSP fragments of 1.7 nm radius with MSP fragments with an additional ice layer of 1 and 3 Ångstrøm (0.1 and 0.3 nm) respectively. The upper row shows the solutions for movement (left), temperature (middle) and radius (right) of the pure MSP fragments. These solutions are similar to the solution from figures 5.12 and 5.13 for 1.6 nm fragments of pure MSP content; although with a lower hit count. From table 5.2 we note that the hit percentage is 78%, and that the most energetic hit have an energy of 11.6 eV. The temperature solution shown in the middle panel shows a similar accumulation of heat as previously observed. We stress that it shows the temperature for the entire integration time, and that most fragments will have lower temperatures than 1050K as shown in the figure. Impacting particles are probed to have temperatures between 250 K and 500 K.

The middle row contains the solutions for an 1.7 nm MSP core with an ice layer of 1Å. The movement solution is similar to the pure MSP solution, but we observe a slightly higher braking of particles, resulting in a hit percentage of 76%, i.e. 2% lower than the pure MSP solution. The most energetic impact is 12.2 eV, i.e. 0.6 eV higher than the pure MSP fragments. The temperature rises rapidly to 186 K and is steady until the ice layer is evaporated at $5 \cdot 10^{-5}$s. The evaporation, which can be observed in the right panel, is so rapid that about half of the impacting fragments have no ice layer at all.

The bottom row shows the solutions for an 1.7 nm MSP core with a 3Å ice layer. An additional braking of the particle in comparison with the previous solutions is observed. The hit percentage is decreased to 72%, while the most energetic impact has increased to 16.4 eV. The radius solution shows that all impacting particles have ice layers of varying width.
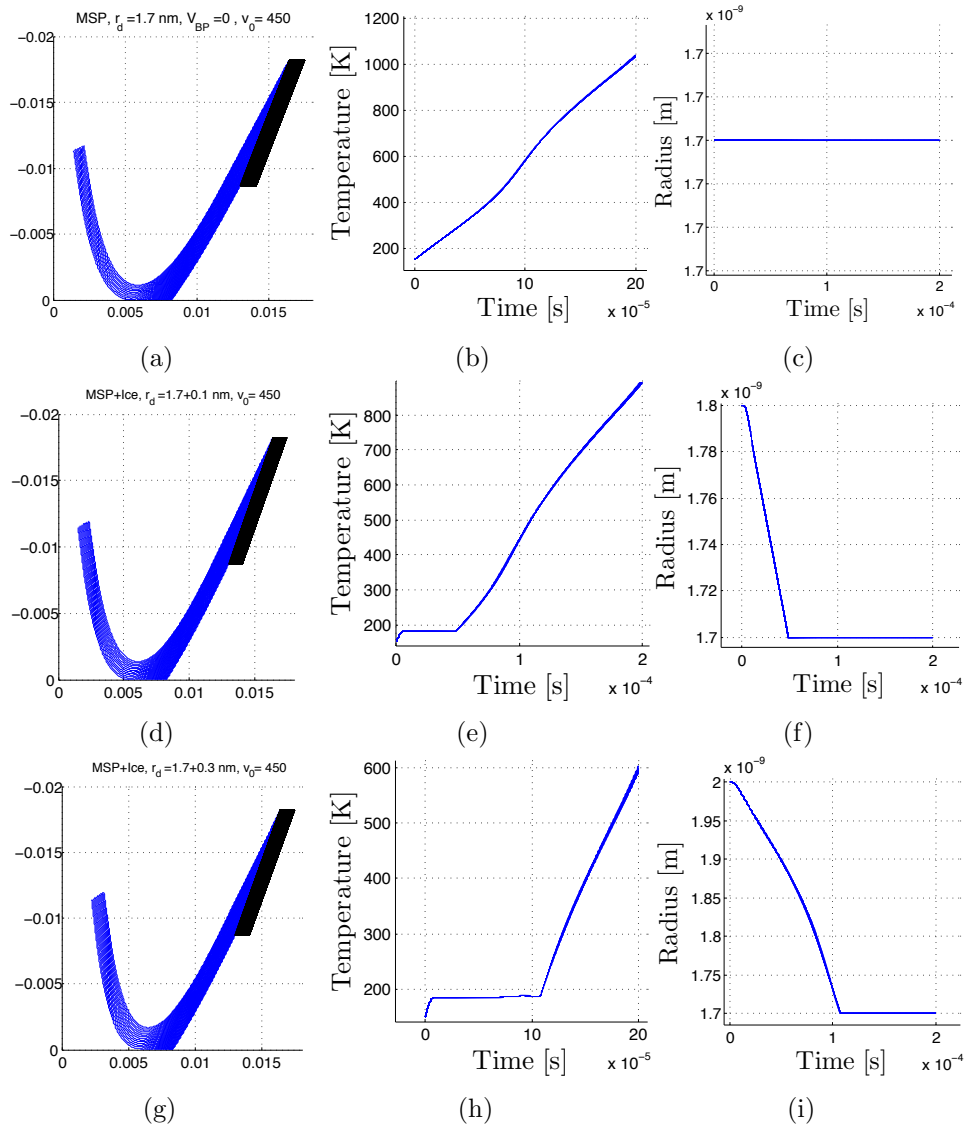
Figure 5.17: Comparison of MSPs with a small or no ice layer. Panels (a)–(c) shows movement, temperature and radius solutions of pure MSPs of radius 1.7 nm. Panels (d)–(f) shows the 1.7 nm radius MSPs with a 1Å ice layer, and (g)–(i) shows the same MSP fragments with a 3Å initial ice layer.

The example of the 1.7 nm-fragment illustrates a trend for MSP fragments with an ice layer; small ice layers have no significant effect on the impact size distribution, but ice layers of 3Å will shift the corresponding size distribution of pure MSP fragments up about 0.1 nm. The obtained results are summarized in table 5.3.

In figure 5.18 we illustrate the general effect of different ice layers on MSP fragments. It is observed that the impacting fragments of pure MSP and MSP with a 1Å layer of ice, represented by blue and purple bars respectively, have virtually the same range of relative impact energies. This observation is consistent for fragments of radii from 1.5 nm to 2.2 nm. Fragments with 3Å ice layers cover a larger range of impact energies, and the most energetic impacts are significantly more energetic than the two latter species.

Figure 5.19 summarizes the solutions for the same three species, however for their median energy impacts. We may draw from the figure that MSP fragments with a 1Å layer of ice will lose the ice completely for $r_0 \leq 1.8$ nm for $v_0 = 450 \text{ms}^{-1}$. Moreover will all particles with radii larger than 2 nm lose their ice layer before impact, if $v_0 = 350 \text{ms}^{-1}$.
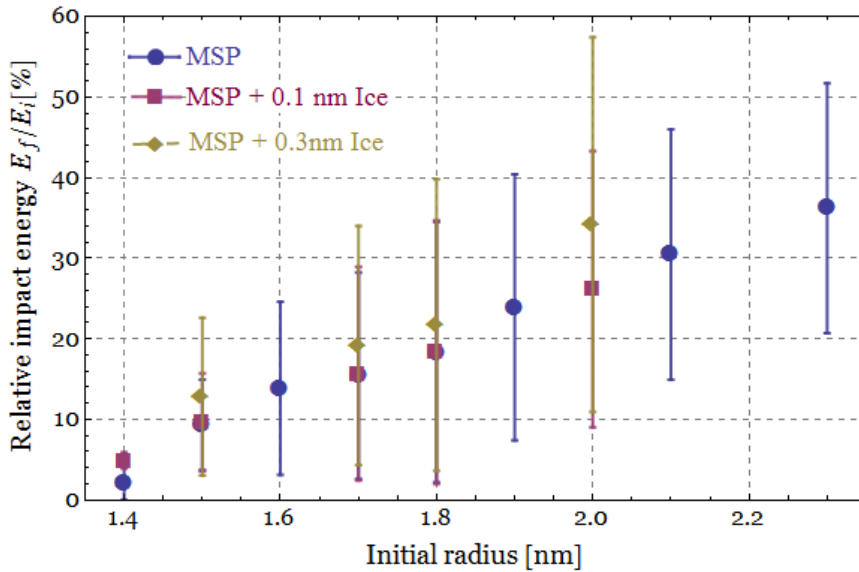
Figure 5.18: Range of preserved energy at impact for pure MSP, and MSP with ice layers of widths respectively 1 and 3 Å. E_f is the 'final' or energy (or impact energy). E_i denotes the initial energy. The initial velocity is $450 ms^{-1}$, and $V_{BP} = 0V$.
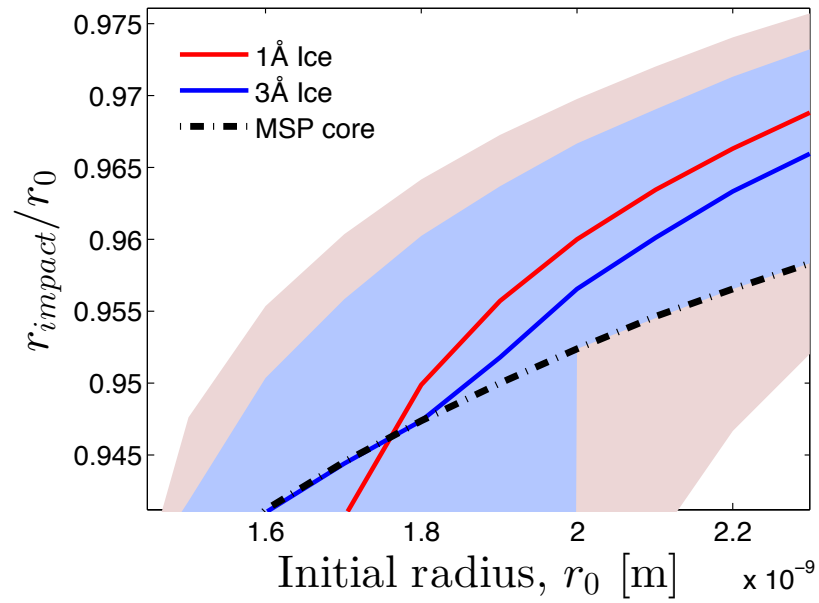
Figure 5.19: Impact radius relative to initial radius of MSPs with an ice layer of width 1 and 3 Å respectively. This is valid for dust grains of impact energy corresponding to the median of the energy range for a particle of a certain initial radius. The error band corresponds to the uncertainty in initial velocity of $v_0 = 450 \pm 100 ms^{-1}$. The dashed line corresponds to a dust grain with 1 Å ice where all the ice have melted with $v_0 = 450 ms^{-1}$.

Table 5.3: The table presents the hit count and energies of impacting fragments at BP from the entire range of G2, here given for MSP with a thin layer of ice on the outermost 1-3 Å of the grain, at different initial velocities

$r_0[nm]$	$v_0 = 350m/s$		$v_0 = 450m/s$		$v_0 = 550m/s$	
	$E_f[eV]$	Hits [%]	$E_f[eV]$	Hits [%]	$E_f[eV]$	Hits [%]
1.2+0.1	—	0.0	—	0.0	$0.0 - 1.0$	2.0
1.2+0.2	—	0.0	—	0.0	$0.0 - 1.6$	4.0
1.2+0.3	—	0.0	—	0.0	$0.0 - 2.4$	8.0
1.3+0.1	—	0.0	—	0.0	$0.0 - 4.4$	28.0
1.3+0.2	—	0.0	—	0.0	$0.0 - 5.5$	28.0
1.3+0.3	—	0.0	—	0.0	$0.0 - 6.9$	32.0
1.4+0.1	—	0.0	$0.0 - 1.5$	6.0	$0.0 - 8.5$	54.0
1.4+0.2	—	0.0	$0.0 - 2.0$	8.0	$0.0 - 10.3$	54.0
1.4+0.3	—	0.0	$0.0 - 2.7$	10.0	$0.0 - 12.3$	54.0
1.5+0.1	—	0.0	$0.0 - 4.4$	28.0	$0.0 - 13.5$	82.0
1.5+0.2	—	0.0	$0.0 - 5.4$	30.0	$0.0 - 15.9$	78.0
1.5+0.3	—	0.0	$0.0 - 6.5$	30.0	$0.0 - 18.8$	78.0
1.6+0.1	—	0.0	$0.0 - 8.0$	52.0	$2.0 - 19.4$	100.0
1.6+0.2	—	0.0	$0.0 - 9.4$	50.0	$1.6 - 22.6$	100.0
1.6+0.3	—	0.0	$0.0 - 11.1$	50.0	$1.4 - 26.3$	100.0
1.7+0.1	$0.0 - 2.0$	10.0	$0.0 - 12.2$	76.0	$5.4 - 26.3$	100.0
1.7+0.2	$0.0 - 2.4$	12.0	$0.0 - 14.1$	72.0	$5.3 - 30.4$	100.0
1.7+0.3	$0.0 - 2.9$	14.0	$0.0 - 16.4$	72.0	$5.5 - 35.0$	100.0
1.8+0.1	$0.0 - 4.5$	30.0	$0.0 - 17.1$	98.0	$9.7 - 34.2$	100.0
1.8+0.2	$0.0 - 5.2$	30.0	$0.0 - 19.6$	94.0	$9.9 - 39.2$	100.0
1.8+0.3	$0.0 - 6.1$	30.0	$0.0 - 22.4$	92.0	$10.5 - 45.0$	100.0
1.9+0.1	$0.0 - 7.4$	48.0	$3.6 - 22.7$	100.0	$14.8 - 43.4$	100.0
1.9+0.2	$0.0 - 8.4$	46.0	$3.1 - 25.8$	100.0	$15.4 - 49.5$	100.0
1.9+0.3	$0.0 - 9.7$	46.0	$3.0 - 29.3$	100.0	$16.6 - 56.1$	100.0
2.0+0.1	$0.0 - 10.8$	68.0	$6.9 - 29.2$	100.0	$20.7 - 53.7$	100.0
2.0+0.2	$0.0 - 12.2$	64.0	$6.5 - 33.0$	100.0	$22.1 - 60.8$	100.0
2.0+0.3	$0.0 - 13.8$	64.0	$6.7 - 37.2$	100.0	$23.8 - 68.5$	100.0
2.1+0.1	$0.0 - 14.7$	86.0	$10.9 - 36.4$	100.0	$27.7 - 65.3$	100.0
2.1+0.2	$0.0 - 16.5$	82.0	$10.7 - 41.0$	100.0	$29.7 - 73.6$	100.0
2.1+0.3	$0.0 - 18.5$	80.0	$11.2 - 46.0$	100.0	$32.2 - 82.5$	100.0
2.2+0.1	$1.5 - 19.1$	100.0	$15.5 - 44.6$	100.0	$35.7 - 78.2$	100.0
2.2+0.2	$1.0 - 21.3$	100.0	$15.6 - 49.9$	100.0	$38.6 - 87.7$	100.0
2.2+0.3	$0.0 - 23.8$	100.0	$16.5 - 55.7$	100.0	$41.8 - 98.2$	100.0

Pure ice particles

In chapter 3.5 it was argued that ice fragments, especially with radii smaller than 3 nm, are unlikely candidates for detection in the current MUDD; they tend to stick to surfaces easily and are in addition poor charge carriers. It is however a possibility that larger ice particles provide some influx to the higher end of the measured energy spectrum, so studying them is advantageous for further research.

Figure 5.20 shows the obtained solutions from the model for 3.5 nm pure ice fragments with a 450 ms^{-1} initial velocity. The hit percentage is 74% and the impact energies ranges up to 85.7 eV. The temperature is found to rise rapidly to a temperature of 186 K. For particles which are reflected away, the temperature rises further to above 200 K as the velocity vector is reversed; the heating is more efficient at lower fragment velocities. The evaporation is observed to be rather rapid, and the reflected fragments have their radii reduced to just above 2.6 nm in $2 \cdot 10^{-4}$s.
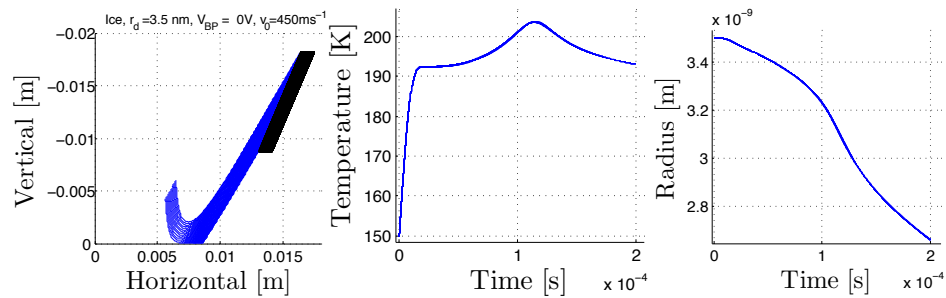
Figure 5.20: Movement (left), temperature (middle) and radius (right) of 3.5 nm pure spherical ice fragment.

In figure 5.21 we show the impact energy signature of the 3.5 nm ice fragments. The radii at impact range from 3.19 to 3.46 nm, resulting in large impact energies. The range of radii at impact indicates the rapid evaporation, even of the larger ice fragments.

Table 5.4 gives a consistent image for pure ice fragments of other sizes and initial velocities. In addition to the low charging probability, the drag force from the neutral gas is observed to be quite strong for ice particles. Because of this, even if smaller ice particles did *not* tend to stick to surfaces, the contribution to the measured current would arguably be small, as few fragments would reach BP. From similar arguments as for the pure MSP fragments, we may draw from the table a detection limit of a minimum radius of 3.0 nm for initial velocities of 450 ms^{-1} and 550 ms^{-1}, stretching up to 3.5 nm for the 350 ms^{-1}-fragments.
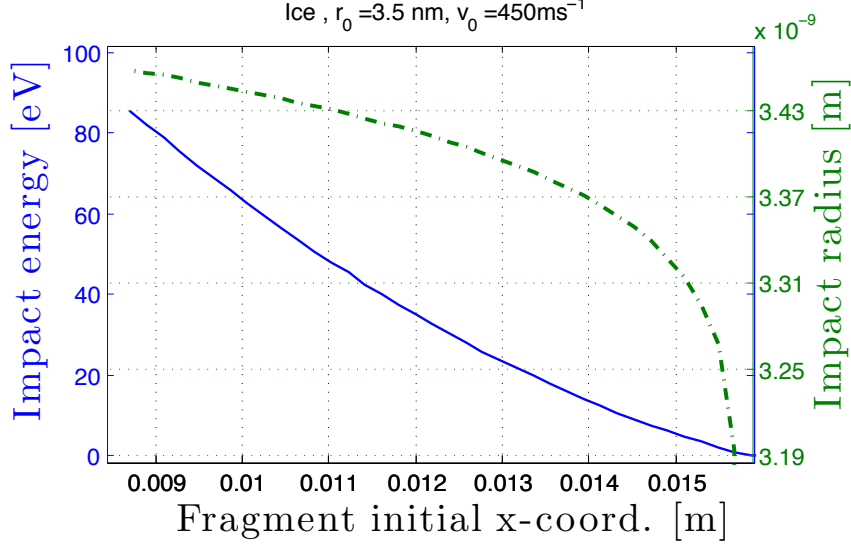
Figure 5.21: Impact radii and corresponding impact energy of 3.5 nm pure ice fragments as a function of the initial height above BP. The initial velocity is $450ms^{-1}$.

Table 5.4: Impact energies of pure ice particles for a 10 V retarding potential. Note that ice particles smaller than 3 nm are assumed to stick to the impact surface in G2, and will thus in practice not be measured in MUDD.

$r_0[nm]$	$v_0 = 350m/s$		$v_0 = 450m/s$		$v_0 = 550m/s$	
	$E_f[eV]$	Hits [%]	$E_f[eV]$	Hits [%]	$E_f[eV]$	Hits [%]
2.5	—	0	$0.0 - 1.4$	2.0	$0.0 - 22.9$	30.0
2.6	—	0	$0.0 - 5.8$	8.0	$0.0 - 31.4$	40.0
2.7	—	0	$0.0 - 10.9$	16.0	$0.0 - 41.6$	48.0
2.8	—	0	$0.0 - 16.9$	24.0	$0.0 - 52.8$	56.0
2.9	—	0	$0.0 - 23.8$	30.0	$0.0 - 65.5$	64.0
3.0	—	0	$0.0 - 31.5$	38.0	$0.0 - 79.5$	74.0
3.1	$0.0 - 4.2$	6.0	$0.0 - 40.3$	44.0	$0.0 - 95.4$	82.0
3.2	$0.0 - 8.2$	12.0	$0.0 - 50.0$	52.0	$0.0 - 112.2$	90.0
3.3	$0.0 - 12.7$	18.0	$0.0 - 60.8$	60.0	$0.0 - 131.4$	98.0
3.4	$0.0 - 18.1$	24.0	$0.0 - 72.7$	66.0	$5.4 - 152.0$	100.0
3.5	$0.0 - 23.9$	30.0	$0.0 - 85.7$	74.0	$11.7 - 173.9$	100.0

5.3.2   Dust fragments in a 20V retarding potential

The 20V retarding potential mode, i.e. $V_{BP} = -10V$, is another detection mode which in theory opens to detect more energetic particles than the 10 V retarding potential.

The left panel of figure 5.22 shows the obtained solutions for the most energetic impacts of pure MSPs with an error band for the uncertainty in initial velocity. It is observed that fragments with radii below 1.5 nm are virtually undetectable in this mode. The right panel yields the same information relative to the initial energy. The figures presents similar tendencies as seen in fig. 5.15 for the first detection mode, although shifted towards higher radii.

Table 5.5 gives a summary of the simulation results for pure MSP fragments in the 20 V retarding potential mode. It is found that the uncertainty in initial velocity produces a larger spread in the energy than the first detection mode. The minimum detectable fragment size for MSPs is found to be 1.8 nm with a lower bound of 1.6 nm and an upper bound of 2.2 nm for higher and lower initial velocities ($\pm100 \mathrm{ms}^{-1}$) respectively. This limit is approximately 0.3 nm larger than for the 10 V detecting mode. The energy of the minimum detectable fragments for the 20V-mode is found to be larger than the energies of the 10V-mode with a factor of approximately 2 (most energetic impacts). The maxim detectable radius of pure MSPs is 2.1 nm bounded by 1.8 nm below and 2.5 nm above due to the intrinsic error in initial velocity.

Table 5.6 gives the results for the pure ice simulations.
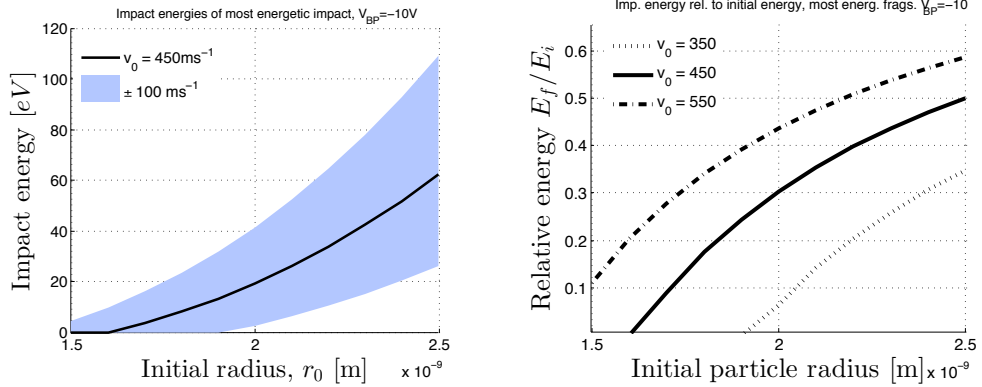

Figure 5.22: Numeric value (left panel) and relative value (right panel) of impact energies as a function of radius for pure MSP fragments. The ribbon (left) and dashed lines (right) represents an uncertainty in initial velocity of 100 ms^{-1}.

Table 5.5: Solutions for pure MSP fragments for the case of $V_{BP} = -10V$ yielding a 20V retarding potential for singly negatively charged fragments; corresponding to an E-field of approximately $2200V/m$.

$r_0[nm]$	$v_0 = 350\ ms^{-1}$		$v_0 = 450\ ms^{-1}$		$v_0 = 550\ ms^{-1}$	
	$E_f[eV]$	Hits [%]	$E_f[eV]$	Hits [%]	$E_f[eV]$	Hits [%]
1.4	—	0.0	—	0.0	—	0.0
1.5	—	0.0	—	0.0	$0.0 - 4.4$	12.0
1.6	—	0.0	—	0.0	$0.0 - 9.9$	42.0
1.7	—	0.0	$0.0 - 3.5$	8.0	$0.0 - 16.2$	70.0
1.8	—	0.0	$0.0 - 8.1$	32.0	$2.2 - 23.6$	100.0
1.9	—	0.0	$0.0 - 13.3$	56.0	$7.6 - 32.0$	100.0
2.0	$0.0 - 2.4$	2.0	$0.0 - 19.3$	82.0	$13.6 - 41.5$	100.0
2.1	$0.0 - 6.3$	22.0	$3.4 - 26.1$	100.0	$20.6 - 52.3$	100.0
2.2	$0.0 - 10.4$	42.0	$8.1 - 33.8$	100.0	$28.7 - 64.5$	100.0
2.3	$0.0 - 15.1$	62.0	$13.5 - 42.3$	100.0	$37.9 - 77.9$	100.0
2.4	$0.0 - 20.4$	82.0	$19.6 - 51.8$	100.0	$48.4 - 92.6$	100.0
2.5	$2.5 - 26.2$	100.0	$26.5 - 62.3$	100.0	$60.1 - 109.2$	100.0

Table 5.6: Solutions for pure ice fragments for the case of $V_{BP} = -10V$.

$r_0[nm]$	$v_0 = 350\ ms^{-1}$		$v_0 = 450\ ms^{-1}$		$v_0 = 550\ ms^{-1}$	
	$E_f[eV]$	Hits [%]	$E_f[eV]$	Hits [%]	$E_f[eV]$	Hits [%]
2.5	—	0.0	—	0.0	—	0.0
2.6	—	0.0	—	0.0	$0.0 - 11.6$	10.0
2.7	—	0.0	—	0.0	$0.0 - 21.2$	18.0
2.8	—	0.0	—	0.0	$0.0 - 32.0$	26.0
2.9	—	0.0	$0.0 - 3.8$	2.0	$0.0 - 44.4$	36.0
3.0	—	0.0	$0.0 - 11.5$	10.0	$0.0 - 58.3$	44.0
3.1	—	0.0	$0.0 - 19.9$	16.0	$0.0 - 73.3$	52.0
3.2	—	0.0	$0.0 - 29.3$	24.0	$0.0 - 90.6$	62.0
3.3	—	0.0	$0.0 - 39.8$	32.0	$0.0 - 109.1$	70.0
3.4	—	0.0	$0.0 - 51.3$	38.0	$0.0 - 129.1$	78.0
3.5	$0.0 - 4.4$	2.0	$0.0 - 64.3$	46.0	$0.0 - 151.3$	88.0

5.3.3   Simulations with alternative potential modes

An intriguing question about the MUDD probe and faraday cup probes in general is: Can such probes yield information on fragment mass spectra, and if so, how sensitive would they be? In the following, we present the summary of solutions for retarding field modes with smaller retarding fields; which will detect smaller particles. The possible utilization of this, with focus on MUDD, is discussed in chapter 6.2.

Table 5.7 presents the obtained results for $V_{BP} = 5V$, that is a retarding potential of 5V; or a retarding field of approximately 550 Vm^{-1}. The results for $V_{BP} = 8V$ is presented in table 5.8, and the corresponding results for the case of $V_{BP} = 9V$ is summarized in table 5.9. The results are limited to radii larger than or equal to 1.0 nm because of the limitations of the model code when handling very small radii (unrealistic constraints on step lengths in the 4th order Runge-Kutta used in the calculations). We observe that the (mean) minimum detectable fragment radius ranges from around 1.3 nm ($V_{BP} = 5V$) to below 1.0 nm ($V_{BP} = 9V$).

In figure 5.23 we show, for a few fragments of small initial radii, how the energy at impact can be influenced by a small retarding field compared to the zero-field situation. It also shows how the impact energies are influenced by accelerating fields, i.e. $V_{BP} > 10V$. This might help to detect very small particles ($\mathcal{O}(1\text{Å})$) which otherwise would be stopped by drag from the neutral air molecules; which will be brought up for discussion below.
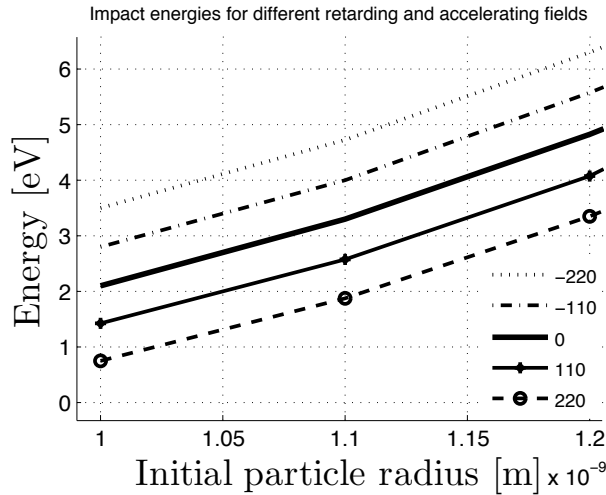

Figure 5.23: Energy for most energetic impacts for retarding and accelerating fields of different values as a function of initial radius. The legend units are [Vm^{-1}], where negative values correspond to accelerating potentials while positive values are retarding. Ex.: ± 220 Vm^{-1} corresponds to $V_{BP} = 8/12$ V.

Table 5.7: Summary of simulations of pure MSPs for bottom plate potential $V_{BP} = 5V$ corresponding to a retarding electric field of approximately $550V/m$.

$r_0[nm]$	$v_0 = 350\ ms^{-1}$		$v_0 = 450\ ms^{-1}$		$v_0 = 550\ ms^{-1}$	
	$E_f[eV]$	Hits [%]	$E_f[eV]$	Hits [%]	$E_f[eV]$	Hits [%]
1.0	—	0.0	—	0.0	—	0.0
1.1	—	0.0	—	0.0	$0.0 - 2.3$	28.0
1.2	—	0.0	$0.0 - 1.2$	12.0	$0.0 - 4.8$	58.0
1.3	—	0.0	$0.0 - 3.0$	36.0	$0.0 - 7.9$	86.0
1.4	$0.0 - 0.7$	6.0	$0.0 - 5.3$	60.0	$1.3 - 11.8$	100.0
1.5	$0.0 - 2.1$	24.0	$0.0 - 8.2$	84.0	$3.6 - 16.4$	100.0
1.6	$0.0 - 3.8$	44.0	$1.0 - 11.6$	100.0	$6.5 - 21.9$	100.0
1.7	$0.0 - 5.9$	64.0	$2.8 - 15.5$	100.0	$10.1 - 28.4$	100.0
1.8	$0.0 - 8.4$	84.0	$5.2 - 20.2$	100.0	$14.5 - 35.9$	100.0
1.9	$0.4 - 11.3$	100.0	$8.1 - 25.6$	100.0	$19.7 - 44.3$	100.0

Table 5.8: Summary of simulations of pure MSPs for bottom plate potential $V_{BP} = 8V$ corresponding to a retarding electric field of approximately $220V/m$.

$r_0[nm]$	$v_0 = 350\ ms^{-1}$		$v_0 = 450\ ms^{-1}$		$v_0 = 550\ ms^{-1}$	
	$E_f[eV]$	Hits [%]	$E_f[eV]$	Hits [%]	$E_f[eV]$	Hits [%]
1.0	—	0.0	$0.0 - 0.8$	20.0	$0.0 - 2.6$	56.0
1.1	—	0.0	$0.0 - 1.9$	42.0	$0.0 - 4.5$	84.0
1.2	$0.0 - 0.7$	18.0	$0.0 - 3.4$	66.0	$0.5 - 7.1$	100.0
1.3	$0.0 - 1.7$	38.0	$0.0 - 5.2$	88.0	$1.7 - 10.2$	100.0
1.4	$0.0 - 2.8$	56.0	$0.5 - 7.6$	100.0	$3.5 - 14.2$	100.0
1.5	$0.0 - 4.3$	82.0	$1.6 - 10.5$	100.0	$5.8 - 18.8$	100.0
1.6	$0.0 - 6.1$	100.0	$3.1 - 13.9$	100.0	$8.8 - 24.3$	100.0

Table 5.9: Summary of simulations of pure MSPs for bottom plate potential $V_{BP} = 9V$ corresponding to a retarding electric field of approximately $110V/m$.

$r_0[nm]$	$v_0 = 350\ ms^{-1}$		$v_0 = 450\ ms^{-1}$		$v_0 = 550\ ms^{-1}$	
	$E_f[eV]$	Hits [%]	$E_f[eV]$	Hits [%]	$E_f[eV]$	Hits [%]
1.0	$0.0 - 0.2$	8.0	$0.0 - 1.4$	48.0	$0.0 - 3.3$	86.0
1.1	$0.0 - 0.7$	28.0	$0.0 - 2.6$	70.0	$0.3 - 5.3$	100.0
1.2	$0.0 - 1.4$	48.0	$0.0 - 4.1$	100.0	$1.2 - 7.8$	100.0
1.3	$0.0 - 2.4$	72.0	$0.4 - 6.0$	100.0	$2.5 - 11.0$	100.0
1.4	$0.0 - 3.6$	92.0	$1.2 - 8.4$	100.0	$4.2 - 14.9$	100.0
1.5	$0.0 - 5.1$	100.0	$2.3 - 11.3$	100.0	$6.6 - 19.6$	100.0

5.3.4   The case of no retarding potential

In the case that $V_{BP} = 10V$, there are in theory no retarding fields, i.e if
we approximate G2 and BP with large conducting planes. In reality there
are probably large edge fields, as shown in the E-field simulations. In this
potential mode, the so called *reference* mode, the fragments are braked only
by the drag from the neutral air molecules. The measured current in this
mode therefore yields a total current with which we may compare the other
currents and deduce the fragment sizes from.

Figure 5.24 shows a the typical dynamics for sub-nanometer fragments
where the majority of 0.7 nm- (7Å-) fragments are stopped entirely by the
neutral gas drag within the integration time. How to handle these free
fragments will be discussed later.
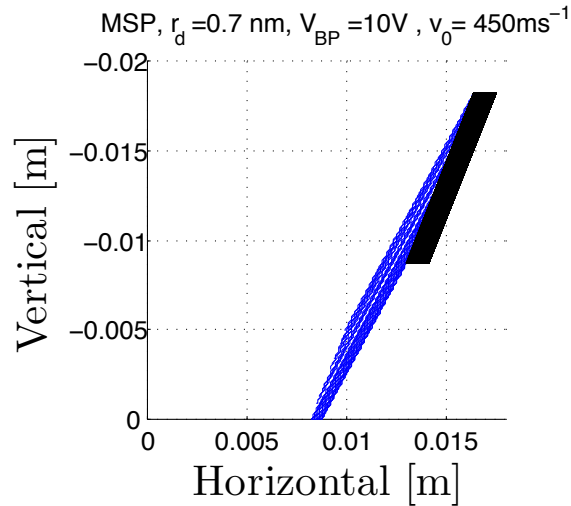
Figure 5.24: Traced paths of MSP fragments of initial radii 0.7 nm for
$V_{BP} = 10V$.

Figure 5.25 shows the typical energy of impacting fragments and their
energy at impact relative to the initial energy at G2. The energies, as seen
in the left panel, are lower than the impact energies in the detecting modes,
but have a smaller spread and represent smaller radii. The spread in relative
impact energy is also smaller, and the fragments keep more of their energy.

Table 5.10 gives a summary of the obtained results for pure MSPs for
the reference mode, i.e. $V_{BP} = 10V$. The obtained values of sub-nanometer
fragments were obtained by a simpler model which used an Euler-procedure
without the temperature and radius solutions to calculate the drag. Very
small MSP fragments may evaporate more severely than larger fragments,
and we can argue that the work done by the neutral drag force on the
fragments will at best be a little bit to large when one does not account for
the decreasing radius.
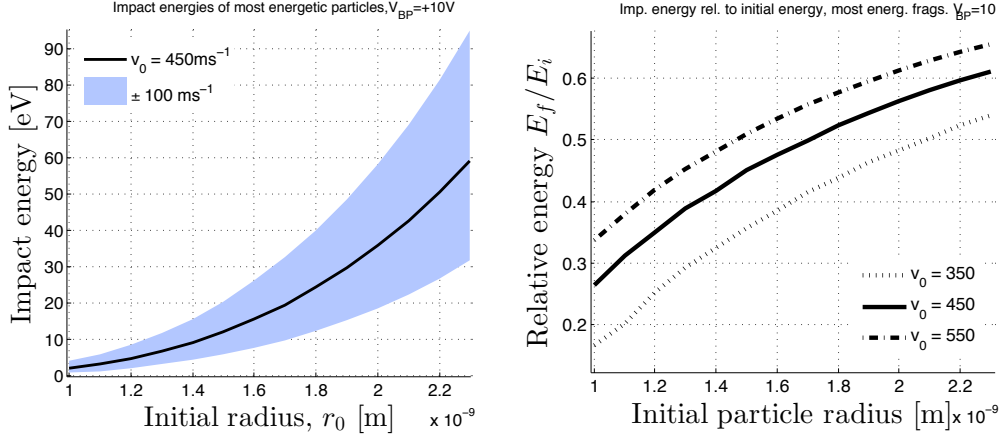
Figure 5.25: Numeric value (left panel) and relative value (right panel) of impact energies as a function of radius for pure MSP fragments in zero E-field.

Table 5.10: Summary of simulations of pure MSPs for bottom plate potential $V_{BP} = 10V$ corresponding to the case of no retarding field, thus independent of charge. Smaller radii are simulated with a simpler program because of numerical constraints.

$r_0[nm]$	$v_0 = 350\ ms^{-1}$		$v_0 = 450\ ms^{-1}$		$v_0 = 550\ ms^{-1}$	
	$E_f[eV]$	Hits [%]	$E_f[eV]$	Hits [%]	$E_f[eV]$	Hits [%]
0.5^1	—	0	—	0	—	0
0.6^1	—	0	—	0	N/A	26
0.7^1	—	0	N/A	18	N/A	82
0.8^1	—	0	N/A	66	N/A	100.0
0.9^1	N/A	26	N/A	100.0	N/A	100.0
1.0	$0.0 - 0.8$	70.0	$0.0 - 2.1$	100.0	$0.4 - 4.0$	100.0
1.1	$0.0 - 1.3$	84.0	$0.1 - 3.3$	100.0	$0.9 - 6.0$	100.0
1.2	$0.0 - 2.1$	96.0	$0.5 - 4.8$	100.0	$1.8 - 8.6$	100.0
1.3	$0.0 - 3.1$	100.0	$1.0 - 6.8$	100.0	$3.2 - 11.8$	100.0
1.4	$0.2 - 4.3$	100.0	$1.9 - 9.1$	100.0	$5.0 - 15.7$	100.0
1.5	$0.5 - 5.8$	100.0	$3.0 - 12.1$	100.0	$7.4 - 20.4$	100.0
1.6	$1.0 - 7.6$	100.0	$4.6 - 15.5$	100.0	$10.3 - 26.0$	100.0
1.7	$1.8 - 9.8$	100.0	$6.6 - 19.5$	100.0	$14.0 - 32.5$	100.0
1.8	$2.7 - 12.3$	100.0	$9.0 - 24.3$	100.0	$18.5 - 40.0$	100.0
1.9	$4.0 - 15.3$	100.0	$12.0 - 29.6$	100.0	$23.8 - 48.5$	100.0
2.0	$5.5 - 18.6$	100.0	$15.5 - 35.8$	100.0	$30.0 - 58.2$	100.0
2.1	$7.4 - 22.4$	100.0	$19.6 - 42.7$	100.0	$37.2 - 69.1$	100.0
2.2	$9.6 - 26.8$	100.0	$24.5 - 50.5$	100.0	$45.4 - 81.3$	100.0
2.3	$12.2 - 31.6$	100.0	$29.9 - 59.1$	100.0	$54.7 - 94.8$	100.0

[1] Euler procedure with Smirnov's force term.

5.3.5   Non-spherical fragments

It has been assumed throughout this paper that the fragments, consisting primarily of pure MSPs, are spherical in shape. Such a constraint on the MSP fragments is not necessarily oversimplifying; laboratory studies show that silicate-based compounds tend to grow spherically, while iron-compounds may grow in chains [Saunders and Plane, 2006]. We introduced in chapter 4.3.3 a factor to compensate for an oblate or elongated morphology; the dynamic shape factor. The model was applied to pure MSP fragments in the first detection mode, $V_{BP} = 0$V with a dynamic shape factor of $\chi = 1.5$ corresponding to chondritic agglomerates or a long chain of small spheres.

The obtained results are summarized in table 5.11. In figure 5.26 the solutions in terms of hit percentage are plotted as a function of initial radius for an initial velocity of 450 ± 100 ms^{-1}. It is observed, as for spherical fragments, that the 450 ms^{-1}-results are shifted slightly towards the upper uncertainty bound. This finding may suggest that the initial velocity of measured fragments in reality is probable to be at least 450 ms^{-1} as fragments of lower initial velocities are relatively harder to measure than fragments of higher velocities, i.e. for realistic MSP radii at least (see [Hunten et al., 1980; Megner et al., 2008; Bardeen et al., 2008]).
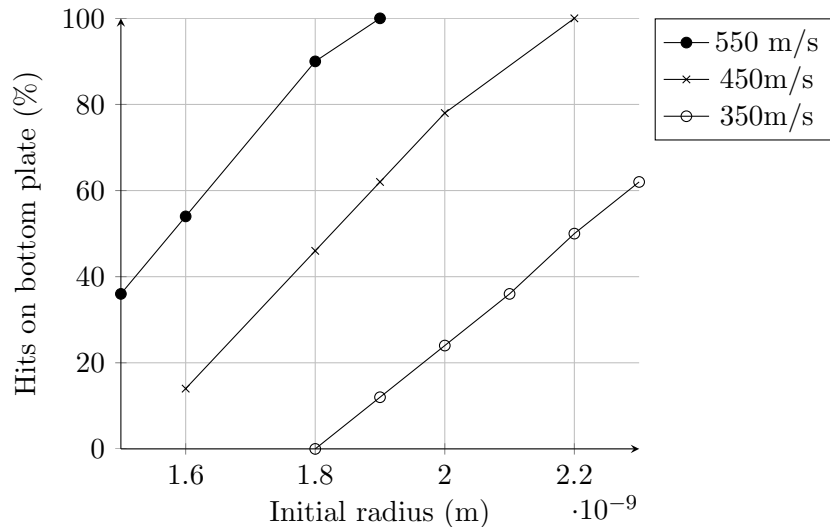

Figure 5.26: Comparison of the proportion of fragments reaching BP for different initial velocities. Characteristic parameters are $\chi = 1.5$, $Z = -1$ and $V_{BP} = 0$V.

Table 5.11: Summary of simulations of non-spherical pure MSP fragments with a dynamic shape factor $\chi = 1.5$ for a bottom plate potential of $V_{BP} = 0\text{V}$.

$r_0[nm]$	$v_0 = 350\ ms^{-1}$		$v_0 = 450\ ms^{-1}$		$v_0 = 550\ ms^{-1}$	
	$E_f[\text{eV}]$	Hits [%]	$E_f[\text{eV}]$	Hits [%]	$E_f[\text{eV}]$	Hits [%]
1.4	—	0.0	—	0.0	$0.0 - 3.0$	16.0
1.5	—	0.0	—	0.0	$0.0 - 6.4$	36.0
1.6	—	0.0	$0.0 - 2.7$	14.0	$0.0 - 10.5$	54.0
1.7	—	0.0	$0.0 - 5.5$	30.0	$0.0 - 15.5$	72.0
1.8	—	0.0	$0.0 - 8.9$	46.0	$0.0 - 21.3$	90.0
1.9	$0.0 - 2.2$	12.0	$0.0 - 13.0$	62.0	$2.1 - 28.2$	100.0
2.0	$0.0 - 4.5$	24.0	$0.0 - 17.8$	78.0	$5.4 - 36.1$	100.0
2.1	$0.0 - 7.2$	36.0	$0.0 - 23.2$	92.0	$9.4 - 45.1$	100.0
2.2	$0.0 - 10.4$	50.0	$1.9 - 29.5$	100.0	$14.4 - 55.4$	100.0
2.3	$0.0 - 14.0$	62.0	$4.7 - 36.5$	100.0	$20.3 - 66.9$	100.0

Chapter 6

Discussion

The simulation results for the two detecting modes, $V_{BP} = 0V$ and $V_{BP} = -10V$, and the reference mode $V_{BP} = +10V$, are representable for the present setup of MUDD. Underlying the data from the first launch of MUDD, and also for future launches, is the question of what the capabilities of the current MUDD design are. From the obtained results we shall discuss the theoretical limits of detection, and compare the sensitivities for different fragment types. Key features such as the most energetic impacts of a certain fragment type in a certain potential, as well as hit percentage, will be used to characterize one specific fragment type. The energy of the most energetic impact is a useful tool for visualizing the obtained results as it is directly proportional to the current. However, for situations where 100% of fragments reach BP, the impact energy yields no new information, so it must be used cautiously. Nevertheless, it may still provide experimental justification for our discussions; and for future development of dust probes.

6.1 Assessment of the current MUDD

Detection limits

It was found for pure MSP fragments, that particles with radii larger than 1 nm experience no significant evaporation for the time scales they encounter in MUDD. This result is also probably applicable to the sub-nanometer particles that have been investigated to a smaller extent. This implies that the energy at impact is related linearly to the position (height) in G2 due to a nearly constant drag force, as observed in figure 5.14. However, if the fragments consists of pure ice, it is found that the relationship between impact energy and initial position is non-linear, as shown in fig. 5.21. This is due to the non-linear neutral drag induced by a strong evaporation of ice fragments with initial radii over 3 nm. As a consequence, the pure ice fragments would yield a much larger range of impact energies, which are furthermore non-linearly distributed as a function of radius. From the

71

literature it is found that ice particles lose considerably more charge than metal or MSP-like fragments [Tomsic, 2001; Adams and Smith, 1971; Havnes and Næsheim, 2007]. This is because the large observed evaporation of pure ice particles will increase the chance of a discharge significantly [Thomson and Iribarne, 1978; Tomsic, 2001]. Thus, even if the ice fragments have a high hit percentage, the measured current from these particles may be small compared to even the most modest MSP currents.

For the second detection mode, $V_{BP} = -10V$, we observe from table 5.6 that pure ice fragments are unlikely to hit BP at all for radii under 3 nm; independently of their initial velocity. The initial assumption that ice particles smaller than 3 nm in radius tend to stick to G2, might therefore be redundant, at least for velocities lower than 450 ms^{-1}. The relatively low hit percentage combined with a low charging probability makes it unlikely for pure ice particles to dominate or have a significant impact on the currents measured in MUDD. However, because of the large range of impact energies, large and energetic ice fragments which have higher chance of becoming charged, may generate a similar current and thus be indistinguishable from an MSPs of smaller sizes.

For spherical particles of pure MSP and pure ice content, we present in table 6.1 the theoretical detection limits of the current MUDD probe on the basis of the results and discussion above. We require that at least 30% of fragments must reach BP for a significant detection.

Table 6.1: Summary of theoretical detection limits of the current MUDD probe. EB^- denotes the error bound for the minimum detectable radius where [L,U] are the lower and upper limits for an uncertainty of ±100 ms^{-1}. EB^+ is correspondingly valid for the maximum detectable radius. The N/A entries for ice denotes too large radii to have been included in the simulations.

	V_{BP}	Mean [nm]	EB^- [L,U]	EB^+ [L,U]
MSP	0 V	1.5–1.8	[1.4, 1.8]	[1.6, 2.2]
MSP	-10 V	1.8–2.1	[1.6, 2.2]	[1.8, 2.5]
ICE	0 V	2.9–N/A	[3, 2.5]	[3.4, N/A]
ICE	-10 V	3.3–N/A	[3.0, > 3.5]	N/A

It must be discussed that this theoretical size distribution may be heavily shifted by a number of factors, of which many have been introduced in this paper. Uncertainties in initial velocity, MSP density and particle shape have been shown to shift the size distribution significantly. Ice layers on MSP fragments were found to introduce non-linear shifts in the size distribution, however not strong shifts. Another important consideration

is the uncertainty in the solutions for fragments with radii smaller than 1 nm. Because of the stiffness of the ordinary system at these sizes, we employed an Euler procedure on a simplified set of equations. This set did not include evaporation, and the primary uncertainty therefore lies within the possible evaporation of sub-nanometer MSP fragments. If they would show to evaporate severely, the conclusions we draw from extrapolating the obtained results have to be altered. The uncertainty in deflection angle at G2 was not investigated, however small changes in deflection angle can also give considerable shifts in size distribution (see e.g. [Tomsic, 2001]).

Preliminary estimate of braking length due to neutral collisions

To precisely estimate the MUDD-currents, the dynamics of the very small fragments must be known. As mentioned in the previous chapter, the equation of motion becomes stiff at very small fragment sizes ($\mathcal{O}(1)$ Å). To validate the less conclusive results from the simpler Euler simulations, we can make a rough estimate analytically. There is almost certainly errors also in these analytical estimates, but it allows us to handle as small fragments as we wish, thus granting useful insight. If the weight of a dust fragment is set equal to the weight of a neutral air column of the same radius as the fragment, we get an estimate of its braking length:

$$\pi r_d^2 m_g n_g L = \frac{4\pi}{3}\rho_d r_d^3 \tag{6.1}$$

where all parameters are characteristic of MUDD, as in the other calculations. Figure 6.1 shows in the right panel a schematic of the problem, and in the left panel the solution for pure MSP fragments, where it has been solved for L. If we assume that the particles move in a straight line with an angle of 6° with the G2-surface, we find that the absolute minimum fragment radius which an impacting fragment may have is around 0.3 nm or 3Å. It may also be observed that fragments with a radius larger than approximately 0.6 nm will have a 100% hit count. This is between 0.2 and 0.3 nm lower than the results from table 5.10, which is probably a consequence of the higher drag introduced by the thermal movement of the neutrals which is included in this latter model.

Diffusive transport between G2 and BP

It has been shown that fragments with $r_d \lesssim 0.6$ nm are partially or completely stopped by the neutral air drag between G2 and BP in the reference mode. The subsequent movement of these fragments have not been included in the model, it may however be an oversimplification to postulate that all of these fragments evaporate and lose their charge. On the other hand, this
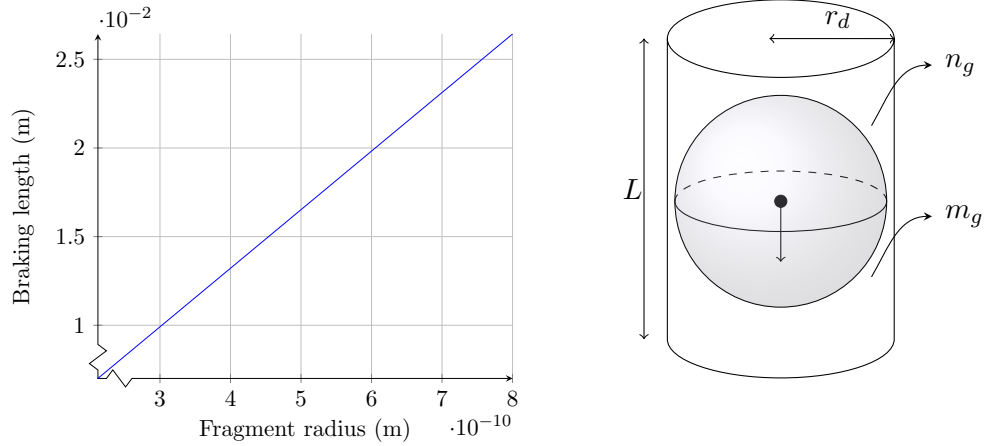
Figure 6.1: Result and schematic for back-of-envelope estimate of the braking length of pure MSP fragments in neutral air.

postulate is arguably true for pure ice fragments, based on the obtained results; further focus is therefore directed towards pure MSP fragments.

The proportion of the MSP size distribution inhabited by particles smaller than 1 nm is thought to be considerable (see e.g. [Hunten et al., 1980; Megner et al., 2006]). Thus the concentration of small fragments which are completely stopped by neutral molecules, may be thought to build up between G2 and BP. We base this assumption on the fact that MSPs have a rather strong resistance towards evaporation. If the concentration of free fragments becomes high enough, it will give rise to a collective stochastic transport in the direction of the density gradient. It is reasonable to assume that the concentration has its maximum around the middle of the region between G2 and BP, thus 50% of the fragments will diffuse towards G2 and 50% towards BP. The smaller fragments have been shown to be likely to carry away negative charge from the fragmentation [Adams and Smith, 1971; Friichtenicht, 1964], and are thus furthermore likely to produce measurable currents at BP. At most, this diffusive transport will give rise to a considerable current to BP of smaller particles, which the model used in this paper does not account for.

We have on the other hand shown that MSPs accumulate heat easily. At a certain point, the evaporation may become large, especially for very small fragments. The question remains whether the diffusion velocity will be large enough to compete with the evaporation, and whether the fragments will evaporate before the BP potential changes. One possibility to solve this problem is to add a small accelerating potential between G2 and BP, which is discussed further below.

Strong E-fields at edges

In the study of fragmentation and transport of charged dust, we used an idealized E-field configuration, i.e. zero field within G2 and a homogeneous field between G2 and BP. From the obtained results it was observed that the electric fields inside MUDD were strongly dependent on position, and the assumption of a homogeneous field is far too optimistic in the vicinity of edges or corners. In the detecting modes, the edge effects between G2 and BP may *not* introduce unwanted effects, because the edge-fields are mainly radial (in the $+\hat{r}$-direction) and would probably give the negative fragments a larger velocity component towards the center of the probe, if any. In the reference mode, as shown in fig. 5.5, the edge effects can become far more important. Below the two outermost rings, the vertical field strength reaches values < -1000 Vm^{-1} which is large enough to brake or even reflect smaller dust particles. This picture is very different from the intended zero field. In addition, we observe very strong fields of strengths on the order of 10^4 Vm^{-1} in the entrance and bottom edge of G2. These large fields also have a direction which acts to attract negative fragments towards the G2 surface, as shown in fig. 5.3a. This anomaly is observed in all the modes, and may act to weaken the flux of fragments to BP through the outermost ring of G2, which constitute about 20% of the flux surface area. Although the field direction between G1 and G2 will act to accelerate negative particles inwards, the NLC particles are probably too energetic to be significantly affected, thus fragmentation should also happen at the outermost ring regardless. Also, if the edge anomalies are strong enough to significantly weaken the effective area of MUDD, the secondary charging effect becomes important, and secondary currents tend to be underestimated.

To reduce the possible effect of these edge fields, it may be a necessary to round off the sharp edges in MUDD, which might yield a higher sensitivity in the low end of the energy (mass) spectrum.

We must stress that the FEM procedure used to solve for the E-fields is finite, as any other numerical method. The numerical values obtained for the fields may therefore not necessarily be absolutely correct. However, the solutions points out the very real effect of field enhancement and there is little doubt that these fields can effect the outermost fragments if they become large enough. The emittance of small charged particles from sharp edges due to the strong edge fields is another possible effect (analogue to field electron emission), but the potential gradient is probably to weak for this mechanism.

Improvement of detection resolution

The detection modes that currently exist in MUDD were found to detect fragments within intervals of an approximate length of 0.3 nm, and slightly

larger intervals were observed for the weaker potential modes. Since the dispersity of the fragments is not known, except for theoretical distributions, it is difficult to decisively determine the true sizes of the measured fragments. By overlaying the theoretical size distribution, which gives higher MSP concentrations for lower sizes [Hunten et al., 1980], on the measured distribution, it is possible to somewhat enhance the measured size distribution.

Another method to enhance the measured distribution is by considering the mechanical geometry of the probe. The modeling performed in this work have not included the effect of different spatial configurations of the inside of the probe. However, it may be desired to explore the possibilities of alternative designs for future launches of MUDD. A rigorous discussion of such a modification does, of course, require new simulations of electric fields, neutrals and dust dynamics, but we may point out certain features from the existing data.

Reducing the width or shifting the position of the grid G2 may be the easiest way to improve the detection interval in MUDD. By reducing the width of MUDD, the detection range can be shortened. If the height over BP is altered, the detection limit may in addition be lowered or increased. Changes in the positioning of the grids G0 and G1 will presumably not induce large changes in the electric field structure, and thus will not improve resolution. From the E-field solutions we may extract that there may be a stronger coupling of edge field lines if G1 is moved closer to G2. This effect can reduce the effective cross-section of G2, leading to more secondary charges. To conclude any further, the mechanical structure must be further investigated, as it requires new simulations. On a practical note, it must also be considered that a higher size resolution requires more detection modes to obtain a good distribution, and therefore will reduce the height resolution.

6.2 Effect of alternative potential gaps in sampling cycle

The obtained results for other retarding potentials than the two modes currently found in MUDD were summarized in chapter 5.3.3. An exposition of other detecting modes is motivated by the possibility of improving the capabilities of MUDD as a mass spectrometer; currently MUDD is capable of directly detecting fragments in two size ranges. From the results it was found that pure ice fragments of smaller radii would evaporate rather quickly in MUDD, thus lowering the limit for the minimum detectable fragment size implies a higher probability for the measured current of coming from *pure* MSPs.

Figure 6.2 gives a comparison of the relative currents in the existing detecting modes to three proposed modes of retarding potentials 1V, 2V and 5V respectively. Because of the limitations in the numerical model, the simulations stop at 1.0 nm. If we again require that around 30% of the fragments have to reach BP to be detected, we must extrapolate the obtained solutions to yield a detection limit for the mode in which $V_{BP} = 9V$. We draw from the results that fragments of sizes down to radii of around 0.8 nm may be detected in this latter mode. This is around 0.7 nm smaller than the smallest radius which can be detected in MUDD today. The number densities of sub-nanometer MSPs are estimated in the literature to be considerable [Hunten et al., 1980; Megner et al., 2006; Bardeen et al., 2008], so the employment of a new detecting mode in MUDD may become fruitful. It is important to note that the addition of other detecting modes yields a better mass resolution at the expense of height resolution. Adding many modes will restrict the resolution to larger scale changes in the NLC structure; which is an advantageous feature of the current MUDD design. Table 6.2 summarizes the detection limits of the alternative detecting modes. We observe that the detection range for the different modes overlap quite a bit, thus making it possible to get a continuous mass spectrum. In a prospective modification of MUDD, the voltage cycle can be optimized to barely overlap to yield the best possible height resolution.

In figure 6.3 we give an alternative presentation of the obtained solutions for alternative potential modes. The data is presented in terms of energy loss of the most energetic fragments, between G2 and BP. This presentation is not directly comparable to MUDD as specific fragment energies cannot be directly measured. However, if it *were* possible to measure the fragment energies directly, the data shows that even the weakest detecting mode would presumably be able to give significant measurements (6-11% larger loss than the reference mode here). Thus it have been pointed out that further development of dust probes may utilize single fragment energy measurements in small retarding potentials.
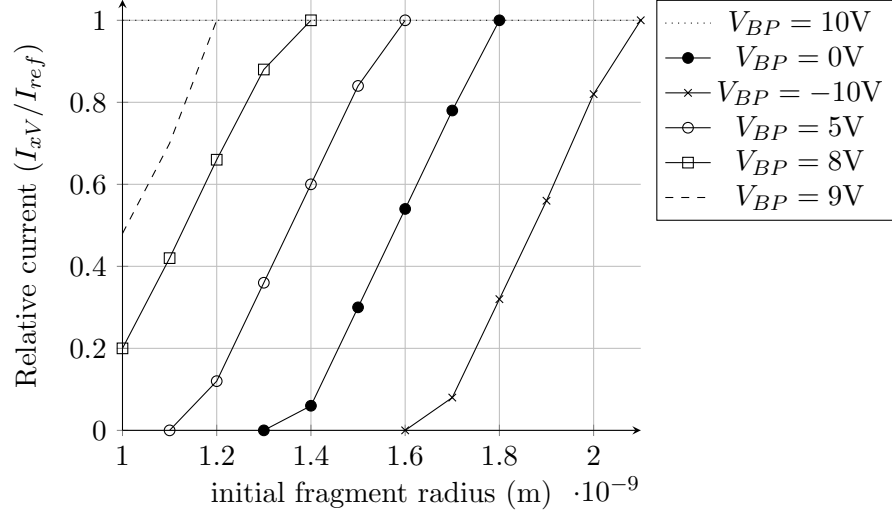
Figure 6.2: Ratio of the current from the reference mode to the current from a detecting mode ($V_{BP} \neq 10V$). The initial velocity is 450 ms^{-1}.

Table 6.2: Theoretical detection limits for alternative potential modes for pure MSP fragments. $EB^{\pm}$ denotes the error bounds for the maximum/minimum detectable radius where [L,U] are the lower and upper limits for an uncertainty of ± 100 ms^{-1}.

V_{BP}	Mean [nm]	EB^- [L,U]	EB^+ [L,U]
5 V	$1.3 - 1.6$	$[\sim 1.1, \sim 1.55]$	$[1.4, 1.9]$
2 V	$\sim 1.05 - 1.4$	$[< 1.0, \sim 1.25]$	$[1.2, 1.6]$
1 V	$\sim 0.8 - 1.2$	$[N/A, \sim 1.1]$	$[1.1, 1.5]$

Reversal of field direction – Accelerating fields

The measurement techniques in MUDD is currently based on decelerating the presupposed negative fragments and measure the reduced current. It has already been shown that particles of radii smaller than ~ 0.6 nm will be stopped partly or completely by the neutral air drag alone. This study therefore includes simulations with small accelerating fields between G2 and BP to see if the detection of very small charged fragments may be assured.

Figure 6.4 compares three retarding E-fields; 330, 220, and 110 Vm^{-1}; corresponding to $V_{BP} = 7V$, $V_{BP} = 8V$ and $V_{BP} = 9V$ respectively, with the reference mode and two accelerating E-fields corresponding to $V_{BP} = 11V$ and $V_{BP} = 12V$. It shows the impact energy of fragments relative to their initial energy. As discussed earlier, it is not possible to draw direct information about what currents these modes would produce in MUDD. We may however use the curves to predict how the currents might develop in the accelerating modes with respect to the retarding modes. We observe that
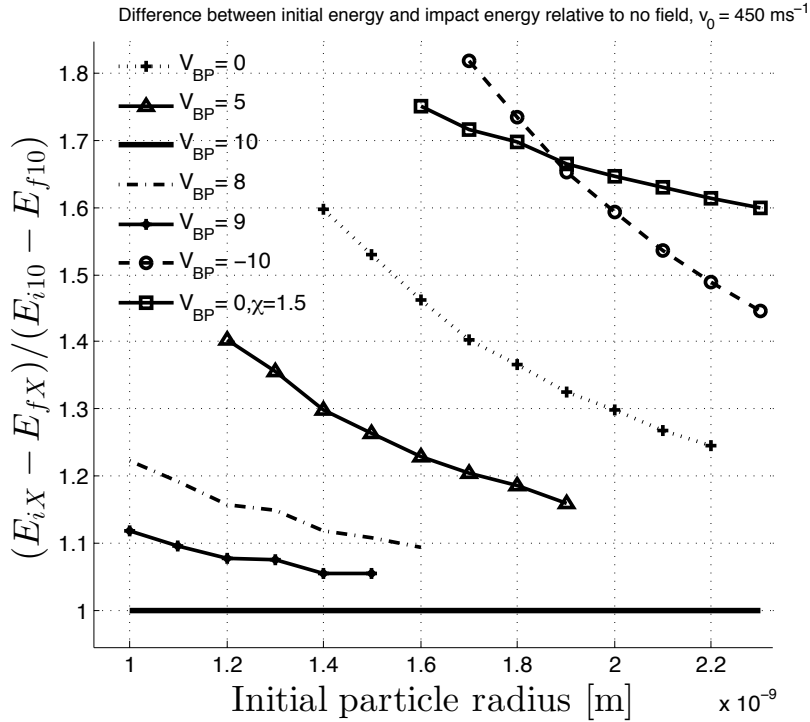
Figure 6.3: Energy loss of most energetic fragments between G2 and BP relative to the reference mode for different detection modes.

the fragments in the first accelerating mode, -110 Vm^{-1}, obtain roughly the same amount of energy relative to the reference mode as the fragments in the first retarding mode, $+110$ Vm^{-1}, lose. Since we are interested in fragment radii below 0.6 nm, we must extrapolate the results to predict the behavior and detectability of the smaller fragments. It is therefore plausible that the detecting limit in the the accelerating mode where $V_{BP} = 11V$ may be approximately 0.4 nm, based on previous discussions.

However, this estimate is rough, and models must be developed to handle smaller fragment radii to get conclusive results. Another aspect is that at these sizes, the fragment evaporation is considerably larger relative to the nanometer-scale particles we have studied, and the possibility of total evaporation may have to be addressed. Also, an accelerating potential will probably also lead to an enhanced free electron current which have to be corrected for.

Relative impact energy for different retarding and accelerating fields
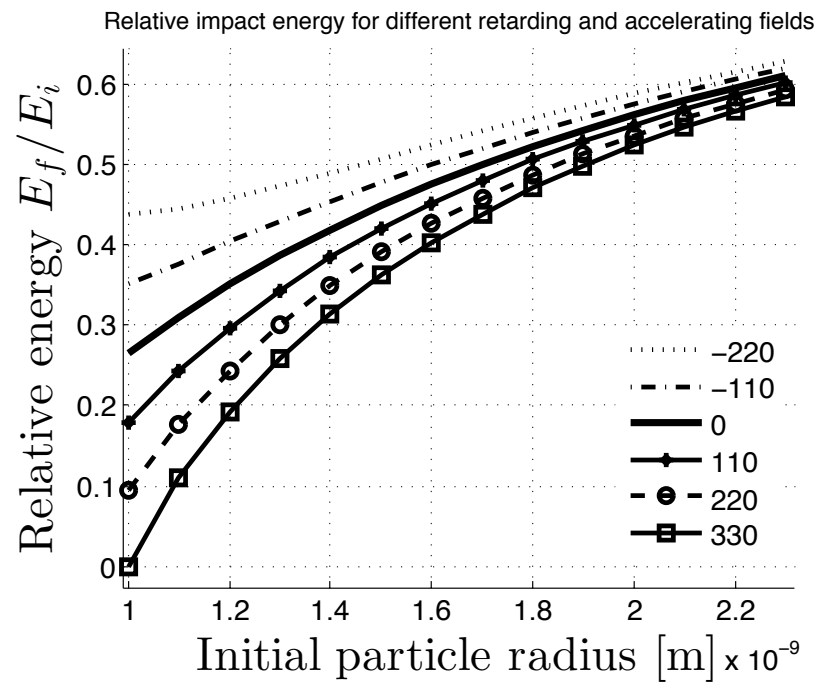
Figure 6.4: Ratio between final energy and initial energy for different initial fragment radii in different electric fields. A positive electric field value corresponds to a retarding field for negative fragments, while negative field values will accelerate the same fragments.

6.3 Heating of dust on impact with G2

This study has operated with zero heat conduction during fragmentation of the incoming NLC particles. However, we must assume that the MSPs and ice particles which constitute the fragments, are not completely rigid, and will therefore be in contact with the G2 surface for a certain amount of time as they are compressed and subsequently bounce of. Consistently, it has been assumed that the NLC particles and fragments have initial temperatures equal to the ambient; 150 K. We address here the possibility of a higher fragment temperature as the fragments leave G2; implying a possibly faster evaporation.

Figure 6.5 shows the geometry of a single fragment (e.g. a single MSP off the surface of an NLC) hitting G2 and being compressed a certain length. We have assumed that a fragment is compressed a distance of maximum half of its radius, and that about 25% of its surface is in direct contact with G2. We assume no loss of mass during compression. The heat conduction problem is solved analytically in appendix C, and the theoretical justification is given there. The time interval Δt in which a fragment is in contact with G2 is estimated by altering the compression length of a fragment while assuming that the mean compression velocity is slightly lower than the rocket (or NLC) velocity of 750 ms^{-1}; assuming some loss of kinetic energy to the inner degrees of freedom.
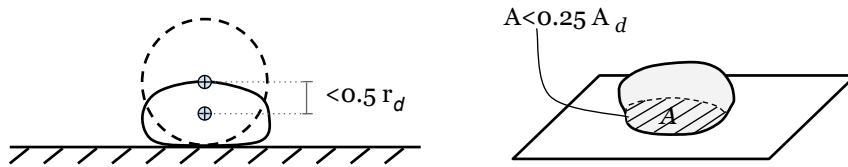

Figure 6.5: Geometry of impact heating of dust grains.

In figure 6.6 we give the solutions for heating of pure MSP fragments of different radii with different heating intervals. For the MSPs, a thermal conductivity of $k = 4.49$Wm^{-1}K^{-1} have been used, based on an Olivine material [Xu et al., 2004]. The heat capacity is taken to be 82 Jmol^{-1}K^{-1}= 707 Jkg^{-1}K^{-1} [Akaogi et al., 1989; Hofmeister, 2001]. Already at $1 \cdot 10^{-12}$s = 1 ps, a significant heating up to a temperature of approximately 240 K is observed for the smallest fragments. This corresponds to a compression of about 3Å in length. Even the largest fragments with radii up to 2 nm will experience a heating of at least 10 K, according to these calculations. If we assume that the larger particles spend relatively larger time intervals at G2 due to the larger compression length, we observe that the heating would be approximately equal; all fragments can be heated up to roughly 240 K.

Figure 6.7 presents the heating of ice particles. Both the thermal con-
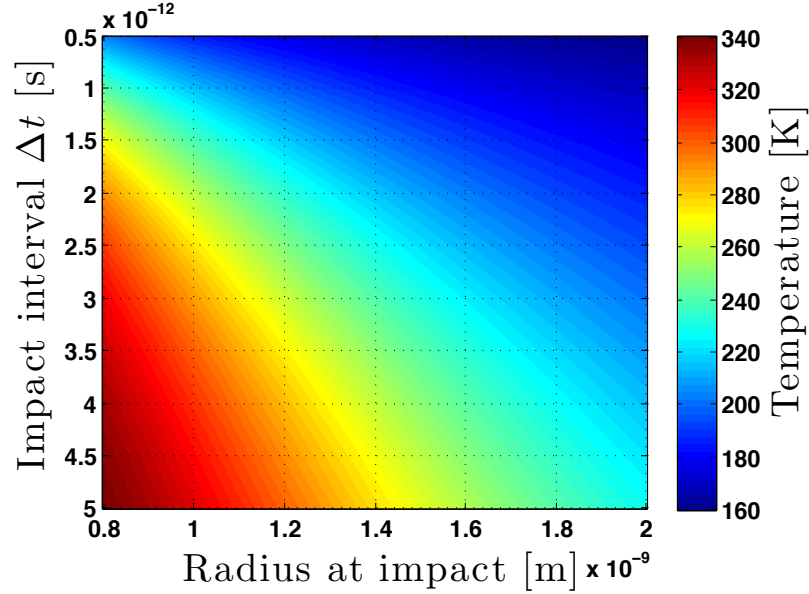
Figure 6.6: Heating of pure MSP fragments for initial radii and compression compression intervals. $T_B = 350$ K.

ductivity and heat capacity of hexagonal ice changes rather rapidly for low temperatures [Slack, 1980], and we have used $k = 1.6$W/mK, and $H_C = 2108$ J/kgK which is valid at mesospheric ambient temperatures [Shulman, 2004]. The heating interval is based on the simulations of Tomsic [2001], and is relatively longer than for the smaller MSPs. The heating is observed to be vigorous among the smallest observable ice fragments with a heating of at least 100 K for a 3 nm fragment. For longer heating intervals, the temperature is observed to increase less violently than in MSPs, as would be expected because of the larger heat capacity. The largest radii presented in the figure are almost at the order of the NLC particles, and are therefore not directly representative for the fragments. However the results from these larger particles will give an estimate to the minimum temperature an ice fragment must acquire in the fragmentation process.

Even though the limitations and simplifications of these one-dimensional calculations are evident, there is little doubt that heating of particles during fragmentation has a significant effect on the initial fragment temperature. We have previously shown that the MSP fragments are difficult to evaporate, and it is uncertain if this additional heating will affect their dynamics. The ice fragments, on the other hand, have been shown to evaporate significantly, and the effect of heating during fragmentation might be considerable. It may be that this heating is sufficient to help with evaporating larger ice fragments to the extent that these also lose charge, cf. previous discussions
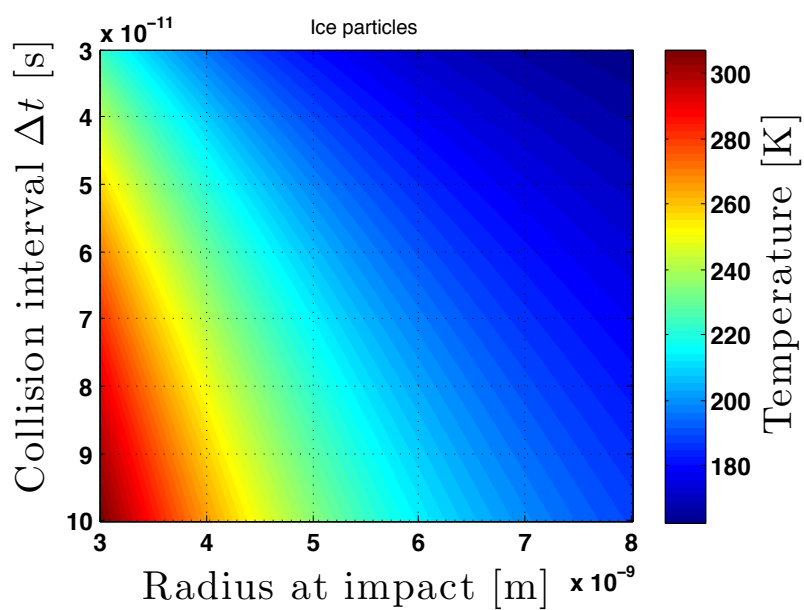
Figure 6.7: Heating of pure ice fragments for initial radii given a certain compression time. The G2 temperature is $T_B = 350$ K.

on electrical discharge from ice particles.

Chapter 7

Conclusions

We have modeled the interior conditions of the rocket-borne impact dust probe MUDD [Havnes et al., 2014] to find the neutral gas conditions and electric field structure within it. This has been the basis for our calculations of the trajectories of the dust fragments which are produced as large NLC ice particles impact on the main grid, G2, in MUDD. The theoretical model for fragment dynamics includes the effect of neutral drag, electric force, and heating of and evaporation from the fragments. The orbit calculations are the basis for determining the best possible size distribution of the collision fragments, which presumably reflect the size distribution of meteoric smoke particles (MSP) in the mesosphere. The considerations given in this thesis, have been aimed towards fully understanding the properties and performance of the MUDD probes.

It was found from the background simulation of the ambient gas, that the neutrals does not introduce significant turbulence in the bottom of the probe, and that a mean background velocity field of zero is probably a good approximation. The neutral molecules were observed to obtain the characteristic temperature of the probe surface at very short timescales, thus implying a certain need of a priori knowledge on the in-flight temperature of the probe. The E-field solutions are found to deviate from the conducting plane solutions with $\sim 5\%$ for the detection modes. However, near the probe walls and at certain edges, we observed field strengths of several thousand Vm^{-1}; which is at least one order of magnitude larger than the intended fields. These anomalies were present also in the reference mode, and may introduce measurement errors.

For singly charged dust fragments, dynamics are found to vary much between the studied fragment species. From an assessment of the detection limits of MUDD, it was found that pure MSP fragments within the range $[1.5, 1.8]$ nm for $V_{BP} = 0$ V, and $[1.8, 2.1]$ nm for $V_{BP} = -10$ V could be detected unambiguously. These ranges were found to be shifted down by 0.1 to 0.2 nm ($\sim 10\%$) and up by 0.3 to 0.4 nm ($\sim 20\%$) due to an uncertainty in

initial velocity of $\pm 100\,\mathrm{ms}^{-1}$. In the reference mode, MSPs with radii smaller than ~ 0.8 nm were stopped completely by air drag. Pure ice fragments will contribute relatively little to the measured currents. This is partly due to the previous results of Tomsic [2001] who found that fragments below 3 nm were unlikely to leave the impact surface (G2 here), but also backed up by the obtained result in this paper from which we can conclude that ice particles smaller than ~ 3.5 nm evaporate significantly. This suggests that ice particles contribute much less to the measured currents than MSPs, which can be justified from the literature [Adams and Smith, 1971; Havnes and Næsheim, 2007; Tomsic, 2001]. The two detecting modes in the present MUDD are on this basis found unlikely to detect ice particles below and above the range $[3, \sim 3.5]$ nm.

From the study of alternative detection modes, it was found that bottom plate potentials from 5 V to 9 V could extend the detection range down to a radius of 0.8 nm (MSPs). To detect fragments smaller than this, it is necessary to employ accelerating potentials. At $V_{BP} = 11$ V, the detection range is found to be 0.4 to 0.7 nm, however such a mode would also be exposed to a larger free electron current which must be corrected for. However, there already exists a method to correct for such enhanced electron currents (see e.g. Havnes and Næsheim [2007]). Figure 7.1 gives a summary of the obtained detection ranges for all the studied potential modes. Also shown is the theoretical concentrations of MSPs at 90 km (a few km higher than our region of interest, but still applicable). The smaller fragments are observed to be abundant, and expanding the current MUDD with smaller potential modes may give decisive evidence for the size distribution of MSPs.

The effect on the size distribution of thin ice layers on MSPs is almost negligible, and an ice layer of 0.3 nm was found to shift the size distribution upwards with approximately 0.1 nm, however the currents from such hybrids are smaller than pure MSP currents by up to 8%. In addition to the uncertainty in velocity, factors such as shape and chemical composition of the MSPs are found to introduce considerable shifts in the measured size distribution; an upward shift of around 0.2 nm may be expected.

The effect of heating during fragmentation was not included in the theoretical model, but in later considerations we showed that this mechanism might be important for the fragment dynamics. For MSP fragments, an increase in the initial temperature will probably not influence the evaporation rate, which was found to be insignificantly affected by the increase in temperature. For pure ice fragments the significant increase in temperature from the one used in this paper, may however introduce a substantial increase in evaporation. As a consequence, the ice fragment size distribution may be shifted to the point that only very few fragments contribute to the total detected currents; implying that MUDD measures primarily particles of meteoric origin.
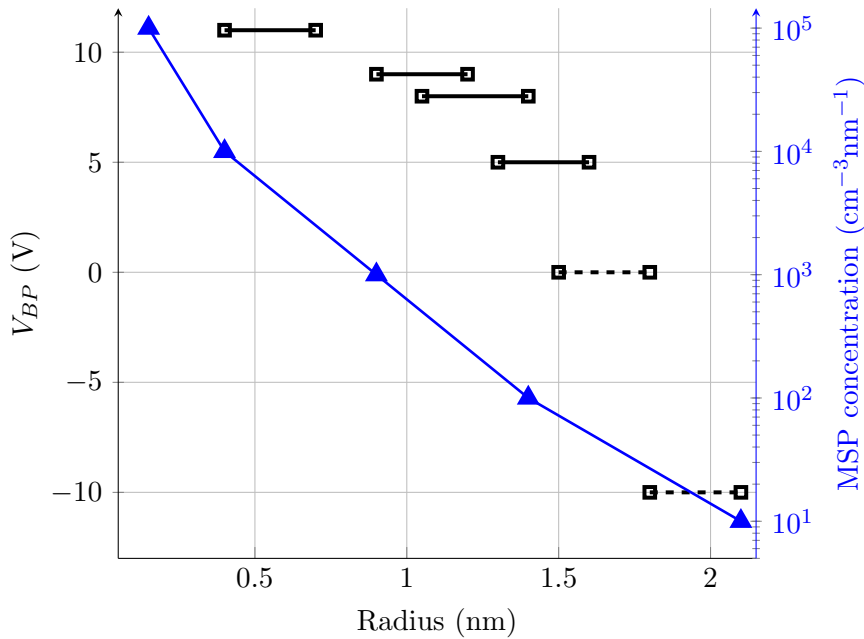
Figure 7.1: Summary of obtained detection ranges in MUDD for an initial fragment velocity of 450 ms^{-1} (black), and theoretical size distribution of pure MSP particles at 90 km (blue) adopted from [Hunten et al., 1980; Megner et al., 2006]. The dashed lines represent existing modes.

Outlook

One of the intensions of this work was, in addition to contribute to the basic research on dust particles, to yield some immediate results to help improve the ongoing research with MUDD. One important result is the theoretical framework we have given for the implementation of MUDD on the MAXIDUSTY-I rocket, due to be launched in july 2014. In addition, our results give some corrections to the obtained size distribution of fragments of Havnes et al. [2014] from the PHOCUS campaign in 2011.

The versatility of the model implemented in this study allows for the obtained solutions to be transferred to other similar dust probes which experience some kind of fragmentation, with simple adjustments. The obtained results have been investigated to the degree that they can – and should – be included in both the analysis of MUDD data and the further development of the probe. Including the findings of this thesis in further research may be beneficial, not only for research with MUDD, but also for other Faraday cup type probes, as we have quantified the possible resolution of such probes and provided a scheme to make them more efficient.

The prime advantage of using Faraday probes, is that the relatively simple designs, with few parts and few extraordinary requirements of the

payload, makes them reliable in-flight. If launched in a triplet (or other multiple configuration), it is possible to configure the detecting potential modes of each probe in such a way that they partly overlap (for reference), but covers different regions of the mass spectrum. In this way, it is possible to obtain a high mass *and* height resolution of the dust fragment ($\propto$ MSP-) sizes. Such a configuration may allow us to investigate the entire theoretical size spectrum of MSPs (cf. figure 7.1), with only a few probes yielding a respectable resolution.

Appendix A

The Boltzmann transport equation

In six-dimensional phase space, we define a probability density function f such that:

$$\mathrm{d}N = f(\vec{r}, m\vec{v}, t)\mathrm{d}^3\vec{r} \cdot m\mathrm{d}^3\vec{v} \qquad (\text{A.1})$$

where $\mathrm{d}N$ is the number of molecules in a volume element $\mathrm{d}^3\vec{r}$ having velocities within a velocity space element $\mathrm{d}^3\vec{v}$ at a time t. The general Boltzmann equation can then be expressed as:

$$\frac{\partial f}{\partial t} = \left(\frac{\partial f}{\partial t}\right)_{Force} + \left(\frac{\partial f}{\partial t}\right)_{Diffusion} + \left(\frac{\partial f}{\partial t}\right)_{Collisions} \qquad (\text{A.2})$$

where the force term only accounts for external forces. From this equation other properties than momentum and position characteristic to a fluid can be derived. For instance is the Navier-Stokes equation fundamentally derived from the Boltzmann equation.

Appendix B

Relationship between Re, Kn, and Ma

The Reynolds number is commonly defined in terms of gas properties as [Colbeck, 1998]:

$$Re = \frac{\rho_g \bar{v}_{th} L}{\eta} \tag{B.1}$$

where ρ_g is the mass density, $\bar{v}_{th} = (8k_B T_g / \pi m_g)^{\frac{1}{2}}$ is the mean gas thermal velocity as given by the Maxwell-Boltzmann distribution, L is a characteristic dimension, and η is the dynamic viscosity.

We can furthermore define the viscosity in terms of the mean free path, λ_{mfp} as:

$$\eta = \frac{1}{2} \rho_g \bar{v}_{th} \lambda_{mfp} \tag{B.2}$$

which allows us to express the mean free path as:

$$\lambda_{mfp} = \frac{2\eta}{\rho_g \bar{v}_{th}}. \tag{B.3}$$

The Knudsen number, which is nothing more than the ratio between the mean free path and characteristic dimension of a system, can thus be written as:

$$Kn = \frac{\lambda_{mfp}}{L} = \frac{\eta}{\rho_g L} \left(\frac{\pi m_g}{2k_B T_g} \right)^{\frac{1}{2}} \tag{B.4}$$

where we have inserted for the mean velocity, $\bar{v}_{th}$ in the term for m.f.p.

We now define the Mach number in terms of the mean molecule velocity as:

$$Ma = \frac{\bar{v}_{th}}{c_s} \tag{B.5}$$

where $c_s = (\gamma k_B T_g / m_g)^{\frac{1}{2}}$ is the speed of sound in the gas. If we now divide the Mach number by the Reynolds number we obtain:

$$\frac{Ma}{Re} = \frac{\eta}{\rho_g L c_s} = \frac{\eta}{\rho_g L} \left(\frac{m_g}{\gamma k_B T_g} \right)^{\frac{1}{2}} \tag{B.6}$$

We observe from equation (B.6), that if we multiply both sides by a factor of $(\gamma \pi / 2)^{\frac{1}{2}}$, we obtain the expression for the Knudsen number as given in eq. (B.4). We may therefore subsequently express the Reynolds number as:

$$Re = \frac{Ma}{Kn} \left(\frac{\gamma \pi}{2} \right) \blacksquare \tag{B.7}$$

Appendix C

Heat conduction during impact

This appendix gives the solution for the possible effect of heating on impact, discussed in section 6.3. Fourier's law of thermal conduction gives the theoretical tools to solve the problem, and the solution is given as a function of material specific constants.

Fourier's law is given on differential form as:

$$\vec{q} = k\nabla T \tag{C.1}$$

where $\vec{q}$ is the local heat flux vector in Wm^{-2}, k is the thermal conductivity in $Wm^{-1}K^{-1}$ and ∇T is the temperature gradient. We integrate over the entire surface S to obtain the integral form of the law:

$$\frac{\partial Q}{\partial t} = k \oint_S \nabla T \cdot d\vec{A} \tag{C.2}$$

where $\partial Q/\partial t$ is the heat flow rate in Ws^{-1} and $d\vec{A}$ is a surface element of the conducting area. When assuming the material is homogeneous and that the boundary temperatures are stationary, the one-dimensional equation becomes:

$$\frac{\Delta Q}{\Delta t} = kA\frac{\Delta T}{\Delta x} \tag{C.3}$$

where A is the conducting area. This discretization is equivalent to the Newtonian heat transfer formulation. If we insert for characteristic parameters of the system the equation becomes:

$$\frac{dQ}{dt} = kA\frac{T_H - T_L}{L} \tag{C.4}$$

where T_H is the temperature of the warmest reservoir, typically the temperature of G2 in MUDD; T_L is the cold particle temperature, typically the

dust grain temperature, and ; the characteristic dimension $L \sim r_d$ in our system.

We assume that the warm surface has a large span and a very high thermal conductance (which is a fair assumption in MUDD, where the probe wall is stainless steel). The amount of heat transferred from a the warm surface to a colder object divided by the temperature difference in the object yields the objects heat capacity C, which in terms of the specific heat capacity, c_p can be stated as:

$$\frac{\Delta Q}{\Delta T} = C = m_d c_p \tag{C.5}$$

where m_d is the object (dust) mass. We divide by a time interval Δt on both sides and take the infinitesimal limit to obtain the differential formulation:

$$\frac{\mathrm{d}T_L}{dt} = kA\frac{T_H - T_L}{L} \bigg/ m_d c_p \tag{C.6}$$

This equation is nothing but a separable differential equation, which we solve to obtain the temperature evolution in the colliding dust grain. We rearrange the equation;

$$\frac{\mathrm{d}T_L}{T_H - T_L} = \frac{dT_L}{1 - \frac{T_L}{T_H}} = \frac{kAT_H/r_d}{m_d c_p}\mathrm{d}t = \kappa \mathrm{d}t \tag{C.7}$$

from which the solution easily follows;

$$T_L(t) = T_H - (T_H - T_L(0))\exp\left(-\frac{\kappa t}{T_H}\right) \blacksquare \tag{C.8}$$

Bibliography

Adams, N.G. and Smith, D. Studies of microparticle impact phenomena leading to the development of a highly sensitive micrometeoroid detector. *Planetary and Space Science*, 19(2):195 – 204, 1971. ISSN 0032-0633. doi: 10.1016/0032-0633(71)90199-1.

Akaogi, Masaki, Ito, Eiji, and Navrotsky, Alexandra. Olivine-modified spinel-spinel transitions in the system mg2sio4-fe2sio4: Calorimetric measurements, thermochemical calculation, and geophysical application. *Journal of Geophysical Research: Solid Earth*, 94(B11):15671–15685, 1989. ISSN 2156-2202. doi: 10.1029/JB094iB11p15671.

Andreae, M.O. and Rosenfeld, D. Aerosol-cloud-precipitation interactions. Part 1. the nature and sources of cloud-active aerosols. *Earth-Science Reviews*, 89(1-2):13 – 41, 2008. ISSN 0012-8252.

Auer, A. and Sitte, K. Detection technique for micrometeoroids using impact ionization. *Earth and Planetary Science Letters*, 4(2):178 – 183, 1968. ISSN 0012-821X. doi: 10.1016/0012-821X(68)90013-7.

Baines, M. J., Williams, I. P., and Asebiomo, A. S. Resistance to the motion of a small sphere moving through a gas. *Mon. Not. of the Royal Ast. Soc.*, 130:63, 1965.

Bardeen, C. G., Toon, O. B., Jensen, E. J., Marsh, D. R., and Harvey, V. L. Numerical simulations of the three-dimensional distribution of meteoric dust in the mesosphere and upper stratosphere. *Journal of Geophysical Research*, 113, 2008.

Bekkeng, T. A., Barjatya, A., Hoppe, U.-P., Pedersen, A., Moen, J. I., Friedrich, M., and Rapp, M. Payload charging events in the mesosphere and their impact on langmuir type electric probes. *Annales Geophysicae*, 31(2):187–196, 2013. doi: 10.5194/angeo-31-187-2013.

Beskok, A. and Karniadakis, G. E. Simulation of heat and momentum transfer in complex microgeometries. *Journal of Thermophysics and Heat Transfer*, 8:647–655, oct 1994.

Bigg, E. Keith. Sources of insoluble inclusions in stratospheric sulfate particles. *Meteoritics & Planetary Science*, 47(5):799–805, 2012. ISSN 1945-5100. doi: 10.1111/j.1945-5100.2012.01346.x.

Bird, G.A. *Molecular Gas Dynamics and the Direct Simulation of Gas Flows.* Oxford science publications. Oxford University Press, Incorporated, 1994. ISBN 9780198561958.

Bohren, Craig F. and Olivero, John J. Evidence for haematite particles at 60 km altitude. *Nature*, 310(5974):216–218, 1984. doi: 10.1038/310216a0.

Brekke, A. *Physics of the Upper Polar Atmosphere.* Springer Berlin Heidelberg, 2 edition, 2013. ISBN 978-3-642-27400-8. doi: 10.1007/978-3-642-27401-5.

Colbeck, I. *Physical and chemical properties of aerosols.* Blackie Academic & Professional, 1998. ISBN 9780751404029.

Cziczo, D. J., Thomson, D. S., and Murphy, D. M. Ablation, flux, and atmospheric implications of meteors inferred from stratospheric aerosol. *Science*, 291(5509):1772–1775, 2001. doi: 10.1126/science.1057737.

DeCarlo, Peter F., Slowik, Jay G., Worsnop, Douglas R., Davidovits, Paul, and Jimenez, Jose L. Particle morphology and density characterization by combined mobility and aerodynamic diameter measurements. part 1: Theory. *Aerosol Science and Technology*, 38(12):1185–1205, 2004. doi: 10.1080/027868290903907.

Evans, Aneurin. *The Dusty Universe.* Series in astronomy. John Wiley & Sons, 1994.

Friedrich, M. and Rapp, M. News from the lower ionosphere: A review of recent developments. *Surveys in Geophysics*, 30:525–559, November 2009. doi: 10.1007/s10712-009-9074-2.

Friichtenicht, J.F. Micrometeroid simulation using nuclear accelerator techniques. *Nuclear Instruments and Methods*, 28(1):70 – 78, 1964. ISSN 0029-554X. doi: http://dx.doi.org/10.1016/0029-554X(64)90351-9.

Fuchs, N. A. The mechanics of aerosols. *Quarterly Journal of the Royal Meteorological Society*, 91(388):249–249, 1965. ISSN 1477-870X. doi: 10.1002/qj.49709138822.

Gabrielli, Paolo, Barbante, Carlo, Plane, John M.C., Varga, Anita, Hong, Sungmin, Cozzi, Giulio, Gaspari, Vania, Planchon, Frédéric AM, Cairns, Warren, and Ferrari, Christophe. Meteoric smoke fallout over the holocene epoch revealed by iridium and platinum in greenland ice. *Nature*, 432 (7020):1011–1014, 2004.

Gadsden, M. The secular changes in noctilucent cloud occurrence: Study of a 31-year sequence to clarify the causes. *Advances in Space Research*, 20 (11):2097 – 2100, 1997. ISSN 0273-1177.

Gombosi, T. I., Nagy, A. F., and Cravens, T. E. Dust and neutral gas modeling of the inner atmospheres of comets. *Reviews of Geophysics*, 24: 667–700, aug 1986. doi: 10.1029/RG024i003p00667.

Gundlach, B., Kilias, S., Beitz, E., and Blum, J. Micrometer-sized ice particles for planetary-science experiments - i. preparation, critical rolling friction force, and specific surface energy. *Icarus*, 214(2):717 – 723, 2011.

Havnes, O. Polar mesospheric summer echoes (pmse) overshoot effect due to cycling of artificial electron heating. *Journal of Geophysical Research: Space Physics*, 109(A2), 2004. ISSN 2156-2202. doi: 10.1029/ 2003JA010159.

Havnes, O. and Kassa, M. On the sizes and observable effects of dust particles in polar mesospheric winter echoes. *Journal of Geophysical Research: Atmospheres*, 114(D9), 2009a.

Havnes, O. and Kassa, M. On the sizes and observable effects of dust particles in polar mesospheric winter echoes. *Journal of Geophysical Research: Atmospheres*, 114(D9), 2009b. ISSN 2156-2202. doi: 10.1029/2008JD011276.

Havnes, O. and Næsheim, L. I. On the secondary charging effects and structure of mesospheric dust particles impacting on rocket probes. *Annales Geophysicae*, 25(3):623–637, 2007. doi: 10.5194/angeo-25-623-2007.

Havnes, O., Morfill, G. E., and Goertz, C. K. Plasma potential and grain charges in a dust cloud embedded in a plasma. *Journal of Geophysical Research: Space Physics*, 89(A12):10999–11003, 1984. ISSN 2156-2202. doi: 10.1029/JA089iA12p10999.

Havnes, O., Trøim, J., Blix, T., Mortensen, W., Næsheim, L. I., Thrane, E., and Tønnesen, T. First detection of charged dust particles in the Earth's mesosphere. *Journal of Geophysical Research: Space Physics*, 101(A5): 10839–10847, 1996. ISSN 2156-2202. doi: 10.1029/96JA00003.

Havnes, O., Gumbel, J., La Hoz, C., and Hedin, J. On the size distribution of collision fragments of nlc dust particles and their relevance to meteoric smoke particles. Accepted by J. of, 2014.

Hedin, J., Gumbel, J., and Rapp, M. On the efficiency of rocket-borne particle detection in the mesosphere. *Atmospheric Chemistry and Physics*, 7(14):3701–3711, 2007. doi: 10.5194/acp-7-3701-2007.

Heim, Lars-Oliver, Blum, Jürgen, Preuss, Markus, and Butt, Hans-Jürgen. Adhesion and friction forces between spherical micrometer-sized particles. *Phys. Rev. Lett.*, 83:3328–3331, Oct 1999. doi: 10.1103/PhysRevLett.83.3328.

Hervig, M. E., Gordley, L. L., Deaver, L. E., Siskind, D. E., Stevens, M. H., III, J. M. Russell, Bailey, S. M., Megner, L., and Bardeen, C. G. First satellite observations of meteoric smoke in the middle atmosphere. *Geophysical Research Letters*, 36, 2009. doi: 10.1029/2009GL039737.

Hervig, Mark E., Deaver, Lance E., Bardeen, Charles G., III, James M. Russell, Bailey, Scott M., and Gordley, Larry L. The content and composition of meteoric smoke in mesospheric ice particles from SOFIE observations. *Journal of Atmospheric and Solar-Terrestrial Physics*, 84-85:1 – 6, 2012. ISSN 1364-6826. doi: http://dx.doi.org/10.1016/j.jastp.2012.04.005.

Hofmeister, A.M. Thermal conductivity of spinels and olivines from vibrational spectroscopy: Ambient conditions. *American Mineralogist*, 86(10): 1188–1208, 2001.

Horanyi, M., Gumbel, J., Witt, G., and Robertson, S. Simulation of rocketborne particle measurements in the mesosphere. *Geophysical Research Letters*, 26(11):1537 – 1540, 1999.

Hunten, Donald M., Turco, Richard P., and Toon, Owen B. Smoke and dust particles of meteoric origin in the mesosphere and stratosphere. *Journal of the Atmospheric Sciences*, 37(6):1342–1357, 1980. doi: 10.1175/1520-0469(1980)037⟨1342:SADPOM⟩2.0.CO;2.

Hutchins, D. K., Harper, M. H., and Felder, R. L. Slip correction measurements for solid spherical particles by modulated dynamic light scattering. *Aerosol Science and Technology*, 22(2):202–218, 1995. doi: 10.1080/02786829408959741.

Ihme, F., Schmidt-Traub, H., and H., Brauer. Theoretical studies on mass transfer at and flow past spheres. *Chemie-Ing-Tech.*, 44:306–313, 1972.

Inhester, B., Klostermeyer, J., Lübken, F. J., and Zahn, U.von . Evidence for ice clouds causing polar mesospheric summer echoes. *Journal of Geophysical Research: Atmospheres*, 99(D10):20937–20954, 1994. ISSN 2156-2202. doi: 10.1029/94JD01619.

Kassa, M., Rapp, M., Hartquist, T. W., and Havnes, O. Secondary charging effects due to icy dust particle impacts on rocket payloads. *Annales Geophysicae*, 30(3):433–439, 2012. doi: 10.5194/angeo-30-433-2012.

Keckhut, P. Temperature trends in the stratosphere and mesosphere. *Advances in Space Research*, 28(7):955 – 959, 2001. ISSN 0273-1177. doi: 10.1016/S0273-1177(01)80023-5.

Keckhut, P., Hauchecorne, A., and Chanin, M. L. Midlatitude long-term variability of the middle atmosphere: Trends and cyclic and episodic changes. *Journal of Geophysical Research: Atmospheres*, 100(D9):18887–18897, 1995. ISSN 2156-2202. doi: 10.1029/95JD01387.

Kelley, K.K. Contribution to data on theoretical metallurgy. *US bureau of mines bulletin*, (383), 1935.

Kendall, K., McN. Alford, N., and Birchall, J. D. A new method for measuring the surface energy of solids. *Nature*, 325:794–796, February 1987. doi: 10.1038/325794a0.

Klekociuk, Andrew R, Brown, Peter G, Pack, Dee W, ReVelle, Douglas O, Edwards, W N, Spalding, Richard E, Tagliaferri, Edward, Yoo, Bernard B, and Zagari, Joseph. Meteoritic dust from the atmospheric disintegration of a large meteoroid. *Nature*, 436(7054):1132–1135, 2005. doi: http://dx.doi.org/10.1038/nature03881.

Klinger, J. Some consequences of a phase transition of water ice on the heat balance of comet nuclei. *Icarus*, 47(3):320 – 324, 1981. ISSN 0019-1035.

Kulmala, M., Laakso, L., Lehtinen, K. E. J., Riipinen, I., Dal Maso, M., Anttila, T., Kerminen, V.-M., Hõrrak, U., Vana, M., and Tammet, H. Initial steps of aerosol growth. *Atmospheric Chemistry and Physics*, 4 (11/12):2553–2560, 2004. doi: 10.5194/acp-4-2553-2004.

Lamy, P.L. Interaction of interplanetary dust grains with the solar radiation field. *Astron. Astrophys.*, 35(2):197–207, Oct 1974.

Langmuir, I., Blodgett, K.B., and Forces, United States. Army Air. *A Mathematical Investigation of Water Droplet Trajectories*. Army Air Forces technical report. Army Air Forces Headquarters, Air Technical Service Command, 1946.

Lichtenegger, H.I.M. and Kömle, N.I. Heating and evaporation of icy particles in the vicinity of comets. *Icarus*, 90(2):319 – 325, 1991. ISSN 0019-1035.

Love, S. G. and Brownlee, D. E. A direct measurement of the terrestrial mass accretion rate of cosmic dust. *Science*, 262(5133):550–553, 1993. doi: 10.1126/science.262.5133.550.

Lübken, F.-J., Lautenbach, J., Höffner, J., Rapp, M., and Zecha, M. First continuous temperature measurements within polar mesosphere summer

echoes. *Journal of Atmospheric and Solar-Terrestrial Physics*, 71(3-4): 453 – 463, 2009. ISSN 1364-6826.

Lübken, Franz-Josef and Höffner, Josef. Experimental evidence for ice particle interaction with metal atoms at the high latitude summer mesopause region. *Geophysical Research Letters*, 31(8), 2004. doi: 10.1029/2004GL019586.

Lübken, Franz-Josef, Rapp, Markus, and Hoffmann, Peter. Neutral air turbulence and temperatures in the vicinity of polar mesosphere summer echoes. *Journal of Geophysical Research: Atmospheres*, 107(D15):ACL 9–1–ACL 9–10, 2002. ISSN 2156-2202. doi: 10.1029/2001JD000915.

Megner, L., Rapp, M., and Gumbel, J. Distribution of meteoric smoke – sensitivity to microphysical properties and atmospheric conditions. *Atmospheric Chemistry and Physics*, 6(12):4415–4426, 2006. doi: 10.5194/acp-6-4415-2006.

Megner, L., Siskind, D. E., Rapp, M., and Gumbel, J. Global and temporal distribution of meteoric smoke: A two-dimensional simulation study. *Journal of Geophysical Research: Atmospheres*, 113(D3), 2008. ISSN 2156-2202. doi: 10.1029/2007JD009054.

Megner, L., Khaplanov, M., Baumgarten, G., Gumbel, J., Stegman, J., Strelnikov, B., and Robertson, S. Large mesospheric ice particles at exceptionally high altitudes. *Annales Geophysicae*, 27(3):943–951, 2009. doi: 10.5194/angeo-27-943-2009.

Murray, Benjamin J. and Jensen, Eric J. Homogeneous nucleation of amorphous solid water particles in the upper mesosphere. *Journal of Atmospheric and Solar-Terrestrial Physics*, 72(1):51 – 61, 2010. ISSN 1364-6826. doi: 10.1016/j.jastp.2009.10.007.

Ostwald, W. Studien über die bildung und umwandlung fester körper. *Zeitschrift für Physikalische Chemie*, 22(289), 1897.

Pedersen, A., Troim, J., and Kane, J. Rocket measurement showing removal of electrons above the mesopause in summer at high latitudes. *Planet. Space Sci.*, 18:945–947, 1969.

Plane, John M.C. On the role of metal silicate molecules as ice nuclei. *Journal of Atmospheric and Solar-Terrestrial Physics*, 73(14-15):2192 – 2200, 2011. ISSN 1364-6826. doi: 10.1016/j.jastp.2010.07.008.

Podolak, Morris, Pollack, James B., and Reynolds, Ray T. Interactions of planetesimals with protoplanetary atmospheres. *Icarus*, 73(1):163 – 179, 1988.

Prather, M. J. and Rodriguez, J. Antarctic ozone: Meteoric control of hno3. *Geophysical Research Letters*, 15(1):1–4, 1988. doi: 10.1029/GL015i001p00001.

Rapp, M. and Lübken, F.-J. Polar mesosphere summer echoes (pmse): Review of observations and current understanding. *Atmospheric Chemistry and Physics*, 4(11/12):2601–2633, 2004. doi: 10.5194/acp-4-2601-2004.

Rapp, M., Gumbel, J., and Lübken, F.-J. Absolute density measurements in the middle atmosphere. *Annales Geophysicae*, 19(5):571–580, 2001. doi: 10.5194/angeo-19-571-2001.

Rapp, M., Lübken, F.-J., Möllemann, A., Thomas, G. E., and Jensen, E. J. Small-scale temperature variations in the vicinity of NLC: Experimental and model results. *Journal of Geophysical Research: Atmospheres*, 107(D19):AAC 11–1–AAC 11–20, 2002. ISSN 2156-2202. doi: 10.1029/2001JD001241.

Rapp, Markus and Thomas, Gary E. Modeling the microphysics of mesospheric ice particles: Assessment of current capabilities and basic sensitivities. *Journal of Atmospheric and Solar-Terrestrial Physics*, 68(7):715 – 744, 2006.

Rapp, Markus, Strelnikova, Irina, and Gumbel, Jörg. Meteoric smoke particles: Evidence from rocket and radar techniques. *Advances in Space Research*, 40(6):809 – 817, 2007. doi: 10.1016/j.asr.2006.11.021.

Robertson, S., Horanyi, M., Knappmiller, S., Sternovsky, Z., Holzworth, R., Shimogawa, M., Friedrich, M., Torkar, K., Gumbel, J., Megner, L., Baumgarten, G., Latteck, R., Rapp, M., Hoppe, U.-P., and Hervig, M. E. Mass analysis of charged aerosol particles in nlc and pmse during the ecoma/mass campaign. *Annales Geophysicae*, 27(3):1213–1232, 2009. doi: 10.5194/angeo-27-1213-2009.

Rosinski, J. and Snow, R. H. Secondary particulate matter from meteor vapors. *Journal of Meteorology*, 18(6):736–745, 1961. doi: 10.1175/1520-0469(1961)018⟨0736:SPMFMV⟩2.0.CO;2.

Saunders, R. W., Möhler, O., Schnaiter, M., Benz, S., Wagner, R., Saathoff, H., Connolly, P. J., Burgess, R., Murray, B. J., Gallagher, M., Wills, R., and Plane, J. M. C. An aerosol chamber investigation of the heterogeneous ice nucleating potential of refractory nanoparticles. *Atmospheric Chemistry and Physics*, 10(3):1227–1247, 2010. doi: 10.5194/acp-10-1227-2010.

Saunders, Russell W. and Plane, John M.C. A laboratory study of meteor smoke analogues: Composition, optical properties and growth kinetics. *Journal of Atmospheric and Solar-Terrestrial Physics*, 68(18):2182 – 2202, 2006. ISSN 1364-6826. doi: 10.1016/j.jastp.2006.09.006.

Schiller, L. and Naumann, A. Mechanics of liquids and gases . Part i. *Die Physik*, 1:101–122, 1933.

She, C.Y., Williams, B.P., Hoffmann, P., Latteck, R., Baumgarten, G., Vance, J.D., Fiedler, J., Acott, P., Fritts, D.C., and Lubken, F.-J. Simultaneous observation of sodium atoms, NLC and PMSE in the summer mesopause region above ALOMAR, Norway $(69°N, 12°E)$. *Journal of Atmospheric and Solar-Terrestrial Physics*, 68(1):93 – 101, 2006. doi: 10.1016/j.jastp.2005.08.014.

Shulman, L. M. The heat capacity of water ice in interstellar or interplanetary conditions. *A&A*, 416(1):187–190, 2004. doi: 10.1051/0004-6361: 20031746.

Slack, Glen A. Thermal conductivity of ice. *Phys. Rev. B*, 22:3065–3071, Sep 1980. doi: 10.1103/PhysRevB.22.3065.

Smirnov, R D, Pigarov, A Yu, Rosenberg, M, Krasheninnikov, S I, and Mendis, D A. Modelling of dynamics and transport of carbon dust particles in tokamaks. *Plasma Physics and Controlled Fusion*, 49(4):347, 2007.

Stokes, G. G. On the Effect of the Internal Friction of Fluids on the Motion of Pendulums. *Transactions of the Cambridge Philosophical Society*, 9:8, 1851.

Theon, J. S., Nordberg, W., Katchen, L. B., and Horvath, J. J. Some observations on the thermal behavior of the mesosphere. *J. Atmos. Sci.*, 24(4):428–438, 1967. doi: 10.1175/1520-0469(1967)024⟨0428:SOOTTB⟩2. 0.CO;2.

Thomas, Gary E. Mesospheric clouds and the physics of the mesopause region. *Reviews of Geophysics*, 29(4):553–575, 1991. doi: 10.1029/ 91RG01604.

Thomas, G.E. and Olivero, J. Noctilucent clouds as possible indicators of global change in the mesosphere. *Advances in Space Research*, 28 (7):937 – 946, 2001. ISSN 0273-1177. doi: http://dx.doi.org/10.1016/ S0273-1177(01)80021-1.

Thomson, B. A. and Iribarne, J. V. The fate of electrical charges in evaporating cloud droplets. *Reviews of Geophysics*, 16(3):431–434, 1978. ISSN 1944-9208. doi: 10.1029/RG016i003p00431.

Tomsic, Anna. *Collisions between water clusters and surfaces*. PhD thesis, Göteborg University, 2001.

Tomsic, Anna, Andersson, Patrik U., Markovic, Nikola, Piskorz, Witold, Svanberg, Marcus, and Pettersson, Jan B. C. Molecular dynamics simulations of cluster-surface collisions: Emission of large fragments. *The Journal of Chemical Physics*, 115(22):10509–10517, 2001. doi: http://dx.doi.org/10.1063/1.1413740.

Voigt, C., Schlager, H., Luo, B. P., Dornbrack, A., Roiger, A., Stock, P., Curtius, J., Vossing, H., Borrmann, S., Davies, S., Konopka, P., Schiller, C., Shur, G., and Peter, T. Nitric acid trihydrate (NAT) formation at low NAT supersaturation in polar stratospheric clouds (PSCs). *Atmospheric Chemistry and Physics*, 5(5):1371–1380, 2005. doi: 10.5194/acp-5-1371-2005.

Cossart, G.von , Fiedler, J., and Zahn, U.von . Size distributions of NLC particles as determined from 3-color observations of NLC by ground-based lidar. *Geophysical Research Letters*, 26(11):1513–1516, 1999. ISSN 1944-8007. doi: 10.1029/1999GL900226.

Wolfram, . Drag coefficient vs. reynolds number. *www.wolframalpha.com*, 2013.

Wu, Zhangfa, and Colbeck, I., . Studies of the dynamic shape factor of aerosol agglomerates. *Europhys. Lett.*, 33(9):719–724, 1996. doi: 10.1209/epl/i1996-00405-1.

Xu, Yousheng, Shankland, Thomas J, Linhardt, Sven, Rubie, David C, Langenhorst, Falko, and Klasinski, Kurt. Thermal diffusivity and conductivity of olivine, wadsleyite and ringwoodite to 20 {GPa} and 1373 k. *Physics of the Earth and Planetary Interiors*, 143–144(0):321 – 336, 2004. ISSN 0031-9201. doi: http://dx.doi.org/10.1016/j.pepi.2004.03.005.

Zasetsky, A. Y., Petelina, S. V., and Svishchev, I. M. Thermodynamics of homogeneous nucleation of ice particles in the polar summer mesosphere. *Atmospheric Chemistry and Physics*, 9(3):965–971, 2009. doi: 10.5194/acp-9-965-2009.